dissertation

Study on low-temperature atmospheric pressure plasma towards elucidation of gas decomposition process

Yosuke SATO

2020

Department of Electrical Engineering

Graduate school of Engineering

Nagoya University

Contents

Chapter 1 Introduction

Plasma is known as the fourth state of matter, after solid, liquid, and gas. In a plasma, electrons separate from the atoms, forming a state where positively and negatively charged particles coexist with unstable neutral radicals. These particles behave as a group while also being exposed to self-generated electric fields in the plasma. Therefore, plasmas are also called ionized gases. Plasmas are quasi-neutral, meaning that the positive and negative charge densities are almost equivalent except over a small characteristic length scale (the Debye length). Applied plasma technologies are used in various industrial fields, such as surface treatments [1, 2], gas decomposition [3, 4], ozone generation [5], and medicine [6]. Plasma and its application technologies are now indispensable in our life.

Plasmas can be classified according to whether they are in thermal equilibrium or non-equilibrium. In a thermal plasma (high-temperature plasma), the electrons and ions are almost the same temperature, while in a non-equilibrium plasma (low-temperature plasma, weakly ionized plasma), the electrons are typically much hotter than the ion and neutral particles. Naturally occurring plasmas are found in the Sun, lightning, and auroras, and among these, the Sun and lightning are thermal plasmas, while auroras are a non-equilibrium plasma.

Plasmas occur naturally or can be produced artificially in a laboratory by applying electromagnetic fields of sufficiently high strength to a gas such that the neutral gas decomposes into charged components in a process called gas breakdown or discharge. The focus of this research is on the non-equilibrium plasma generated by discharge at atmospheric pressure. This section provides an introduction to the history of discharge plasma physics and its applications along with the aims of this thesis.

1.1 History of discharge plasma

The term “plasma” comes from Greek, meaning “something molded or created” [7, 8]. In the 1920s, Irving Langmuir proposed referring to ionized gases as plasmas. He also discussed the sheath, which is an essential concept when discussing plasma even now. The sheath is a region between a plasma and a wall (solid surface) which is non-neutral and electrically positive.

In the 19th century, many discharge types were discovered and great progress was made in the study of discharge plasma. At the start of the 1800s, arc discharge, a type of thermal plasma, was produced by using large battery equipment. This was followed by glow discharge, discovered by Faraday in 1835. In 1878, corona discharge was studied under pin-to-plane and wire-to-cylinder electrode geometries. The relations between current and applied voltage were experimentally found about 20 years later. Along with corona discharge, silent discharge and surface discharge are also studied at atmospheric pressure. These discharges are also called dielectric barrier discharge because a dielectric is placed on the electrode.

Paschen and Townsend greatly contributed to progress in discharge theory. In 1884, the Paschen effect was discovered, which is expressed as Paschen curves. This states that the discharge starting voltage (breakdown voltage) between two plate electrodes depends on the product of the gas pressure P and the gap distance d (Pd), and Pd has a minimum value (Paschen minimum) depending on the type of gas or electrode. Later, Townsend explained these experimental results theoretically, and this theory is often referred to as the Townsend theory of gas breakdown. The essence of the theory is the concept of exponential multiplication of electrons due to collisions of a few seed

electrons with neutral gas particles in an electric field. This creates a so-called electron avalanche.

By the end of the 1930s, it became clear that a new theory was required to explain the formation of gas discharges at high pressures and high voltages. A new theory of spark breakdown was developed independently by Loeb and Meek [9, 10] in 1940, known as streamer theory. While streamer theory still uses the electron avalanche concept to explain the breakdown process, it differs in that it considers a single large electron avalanche rather than a series of avalanches as the mechanism of breakdown. A single large avalanche forms an active zone (the streamer head), which propagates into the gap inducing additional electron avalanches, which are drawn toward the primary avalanche. As the primary avalanche propagates into the gap, it leaves behind a long and thin trail of quasi neutral plasma from which comes the term “streamer”.

1.2 Low-temperature atmospheric pressure plasma

With the development of discharge technologies, low-temperature (cold) atmospheric pressure plasma (LTAPP) has attracted much interest because of its ease of generation and potential for various applications.

1.2.1 Basic properties

Conventional plasma is mainly generated under low-pressure and high-pressure conditions, which require expensive pressure control equipment and tend to be high cost. In contrast, LTAPP is mainly generated by discharge near atmospheric pressure and does not require pressure-control equipment. This feature of LTAPP enlarges the range of applications to include large objects that cannot be put inside equipment, heat-sensitive

substances, and living bodies. An LTAPP device can be constructed using only an electric power source and a set of electrodes in the simplest case, making it possible to create compact and portable devices.

LTAPP is mainly produced by discharges such as corona, glow, dielectric barrier, and streamer discharges. At atmospheric pressure, gas heating easily occurs and tends to transition to arc or spark (thermal plasma) due to high collision frequency. In order to prevent the transition to arc, it is important to secure off-time by using alternating nanosecond pulse voltage, by limiting the current by using a dielectric barrier, and by using a configuration that assists with heat dispersal. This kind of device creates a non-equilibrium plasma where the gas temperature is near room temperature while the electron temperature is higher than 10,000 K.

1.2.2 Applications

By utilizing LTAPP, strong chemical reactions that do not normally occur in our daily lives can be used. As more measures for improving safety and power efficiency are being implemented, more people are generating and utilizing LTAPP. There are various applications that utilize LTAPP, such as environmental applications [11, 12], material processing [1, 2], medicine [6, 13], energy [14-16], and light sources [17].

Applications of LTAPP are classified into four types: using the plasma itself, and using interactions between the plasma and a gas, liquid, or solid. This study focuses on the plasma itself and on the interaction between the plasma and a gas, such as gas decomposition by non-equilibrium plasma.

Examples of applications are presented for each type. Applications using plasma itself include light sources, plasma displays, ozone production, and generation of excimer

radiation.

Applications using interactions between LTAPP and a gas include degradation of pollutant molecules in gas, deodorization, flow control by plasma actuator, plasma jets, and combustion ignition.

Applications utilizing interactions between LTAPP and a liquid include plasma medicine, plasma agriculture, plasma-treated water, blood coagulation, and degradation of pollutant molecules in liquid.

Finally, applications using interactions between LTAPP and a solid include sterilization, etching, chemical vapor deposition, polymer deposition, surface modification, and plasma-catalyst combined systems. LTAPP has great potential for various industrial fields, including those mentioned above.

1.2.3 Generation by discharges

LTAPP is mainly produced by discharges such as corona, glow, dielectric barrier, and streamer discharge. This section describes streamer discharge and dielectric barrier discharge.

1.2.3.1 Streamer discharge

Streamer discharge is fundamental for the LTAPP phenomena and forms a propagation of filamentary ionization waves called a streamer head. Applying a high voltage of several kilovolts between pin and plane electrodes generates filamentary light emissions, as shown in Figure 1.1. These light emissions are due to streamer discharge. The streamer discharge usually propagates while changing direction and branching randomly. The propagation speed of the streamer discharge is on the order of magnitude

of 1×10^6 m/s (mm/ns) [18], and gas heating rarely occurs.

The physical process of the streamer discharge is as follows (Figure 1.2). When a high positive voltage is applied to the pin electrode, a remarkably non-uniform electric field is formed around the electrode. This electric field accelerates electrons that have detached from negative ions between the electrodes toward the pin electrode. The electrons induce electron avalanches as they move, thereby producing additional electrons, excited species, and negative and positive ions. Due to the large difference in mass between electrons and other particles, a deviation in the space charge arises. The streamer discharge starts to propagate toward the plane electrode when the space charge induces an electric field as strong as the outer electric field. Streamer propagation can deliver a rich variety of reactive species, including O atoms, N atoms, ·OH radicals, and ·NO radicals in air. The tip of the streamer is called the streamer head, and is a location that has excessive positive charge. Photoionization is also thought to be important as an electron source [19]. The region behind the streamer head is called the streamer channel and is in the plasma state. When the streamer head approaches the plane electrode, the electric field near the plane electrode becomes high. The streamer head disappears when it reaches the plane electrode and the electric field between the electrodes becomes redistributed. The phenomenon up until the streamer head disappears is called the primary streamer. After the primary streamer, a high-electric-field region propagates again from the pin electrode as the voltage continues to be applied, and this phenomenon is the secondary streamer. The discharge transitions to arc or spark if further voltage continues to be applied.

Streamer discharge is a fundamental phenomenon, but is not completely understood. To date, atmospheric pressure streamer discharges in air-related gases

involving N_2, O_2, N_2/O_2, and $N_2/O_2/H_2O$ mixtures have been studied experimentally [20, 21], analytically, and computationally [22–28]. Numerical simulation studies have discussed the propagation of primary and secondary streamers mainly in air-related gases which causes generation of O, N, and OH radicals. There are few studies on streamer discharge in noble gases at atmospheric pressure, and while there are previous studies of positive streamers, which are generated by applying positive voltages, few studies have considered negative streamers. In addition to low-pressure discharges, an understanding of noble gas discharges remains an important issue for providing broad knowledge over a wide range of atmospheric pressure plasma applications.

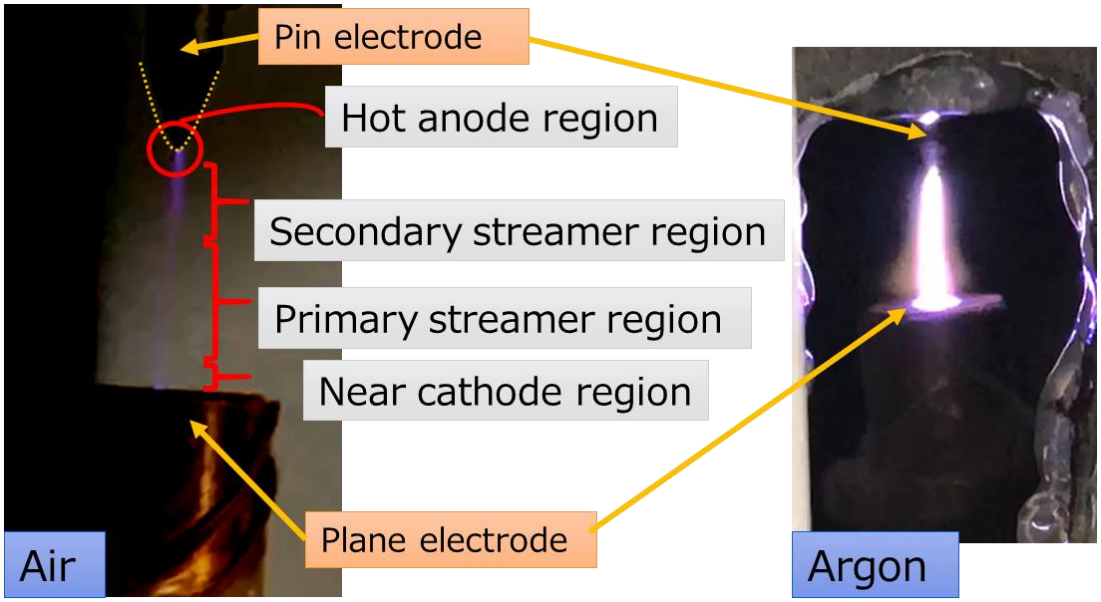

Figure 1.1: Streamer discharges in air and argon under a pin-to-plane geometry.

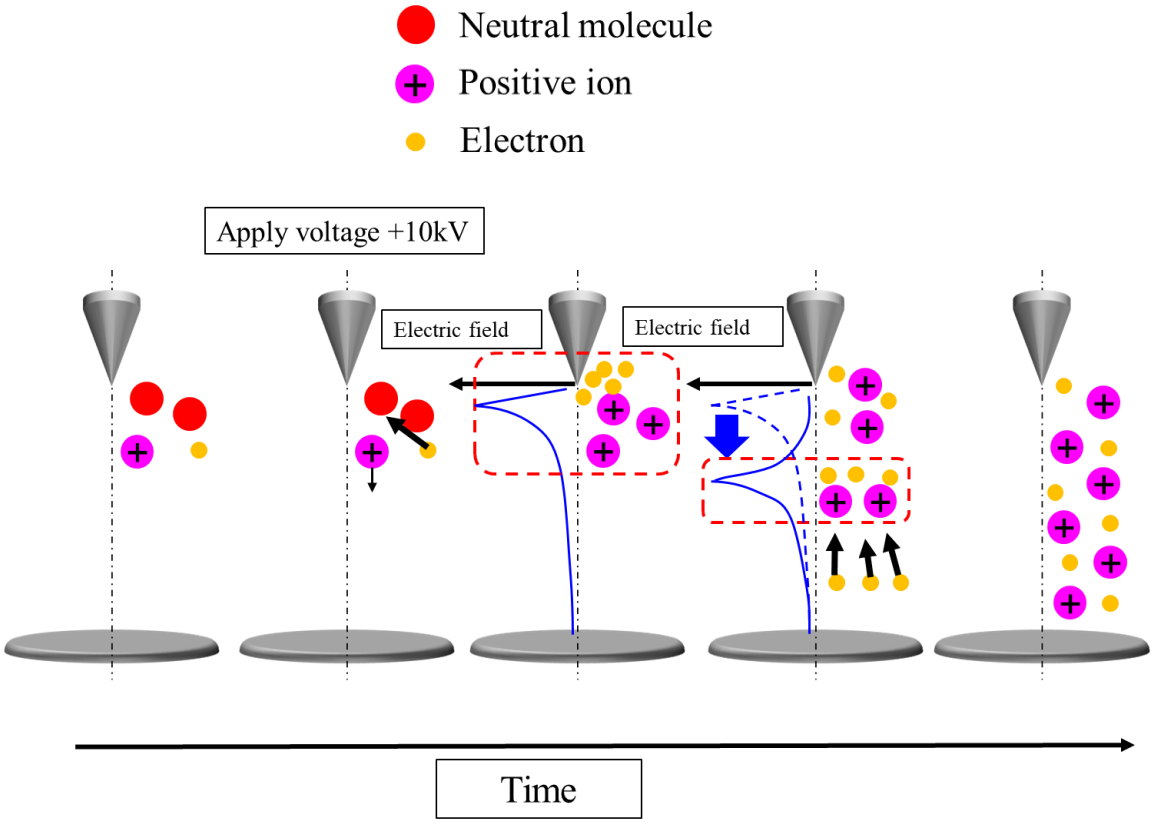

Figure 1.2: Streamer propagation mechanism.

1.2.3.2 Dielectric barrier discharge

LTAPP easily transitions to arc, which is not conducive to controllability and safety. Dielectric barrier discharge (DBD) is a typical method for generating stable LTAPP and has recently been applied in various fields, including surface treatments, medicine, air-pollution control, and material synthesis with assimilation of carbon dioxide [29-38]. DBD devices comprise one or more planar or cylindrical dielectrics and their corresponding shaped electrodes. The dielectrics act as current limiters that prevent transitions to spark or arc (thermal plasma). This is a beneficial feature for sustaining the low-temperature plasma and improving safety. DBD devices are mainly driven by alternative nanosecond (ns)-pulse voltage. Electron avalanches in the gas region,

secondary electron emissions from the dielectric wall, and surface charge accumulated on the dielectric surface are important for control of discharge properties.

DBD devices are classified into three types as shown in Figure 1.3: a planar type that generates plasma on and above a dielectric surface, a plasma-jet type that emits a discharge, and a reactor-type in which discharge remains within the device. Each device type can feed a chemically reactive species to a region downstream of the device.

Many studies of planar-type DBDs have focused on plasma actuator devices. Previous studies report that the discharge mode changes from streamer to glow, depending on the applied voltage polarity [38]. Control of the surface charge can align the movement direction of charged species in plasma colliding with background gas and enhancing ionic winds [29].

The plasma jet type is a representative coaxial-type DBD device. Experimental results have revealed that plasma jets are a series of rapidly propagating (around 100 km/s) luminous streamer discharges called plasma bullets [39], and that these bullets are ring-shaped [30]. Jet-type discharges involve two streamer structures depending on the jet width [40]. Propagating bullets are guided by a He-air mixing layer with background atmospheric air [41]. Photoionization determines the streamer propagation speed but is not itself the cause of propagation [42].

This research focuses on the reactor type DBD, in which consensus has been reached that discharges in reactor-type DBDs are glow-like in pure He and filament-like in pure Ar [43]. When mixing NH_3 and Ar, a transition of discharges from filament-like to glow-like was observed and this transition was explained by the Penning effect [44]. Helium discharge appears nearly uniform, whereas strong emissions are observed in regions near electrodes and dielectric surfaces [45]. There are comprehensive parametric

studies by one-dimensional numerical simulation of applied voltage and dielectric properties [46, 47]. Previous works have also reported equivalent circuit modeling [47], measurement of discharge current and electron number density in an argon DBD device [48], and development of a catalyst combination system to improve conversion efficiency [49].

However, ns-scale dynamics of reactor-type discharges have not yet been elucidated, so the reason for strong light emission near the electrodes remains unclear. One-dimensional analysis assuming a uniform axial distribution is substantially limited in terms of revealing any details of the formation process of plasma inside a reactor-type DBD; multidimensional analysis is instead required. In addition, the relations between plasma distributions in the device and device/process parameters remain unclear. To improve development efficiency and acquire design guidelines for device configurations and operational conditions, there is a need for parametric studies of more parameters than were studied previously [46]. In addition to DBD itself, this research investigates gas decomposition properties in a reactor-type DBD device as an application.

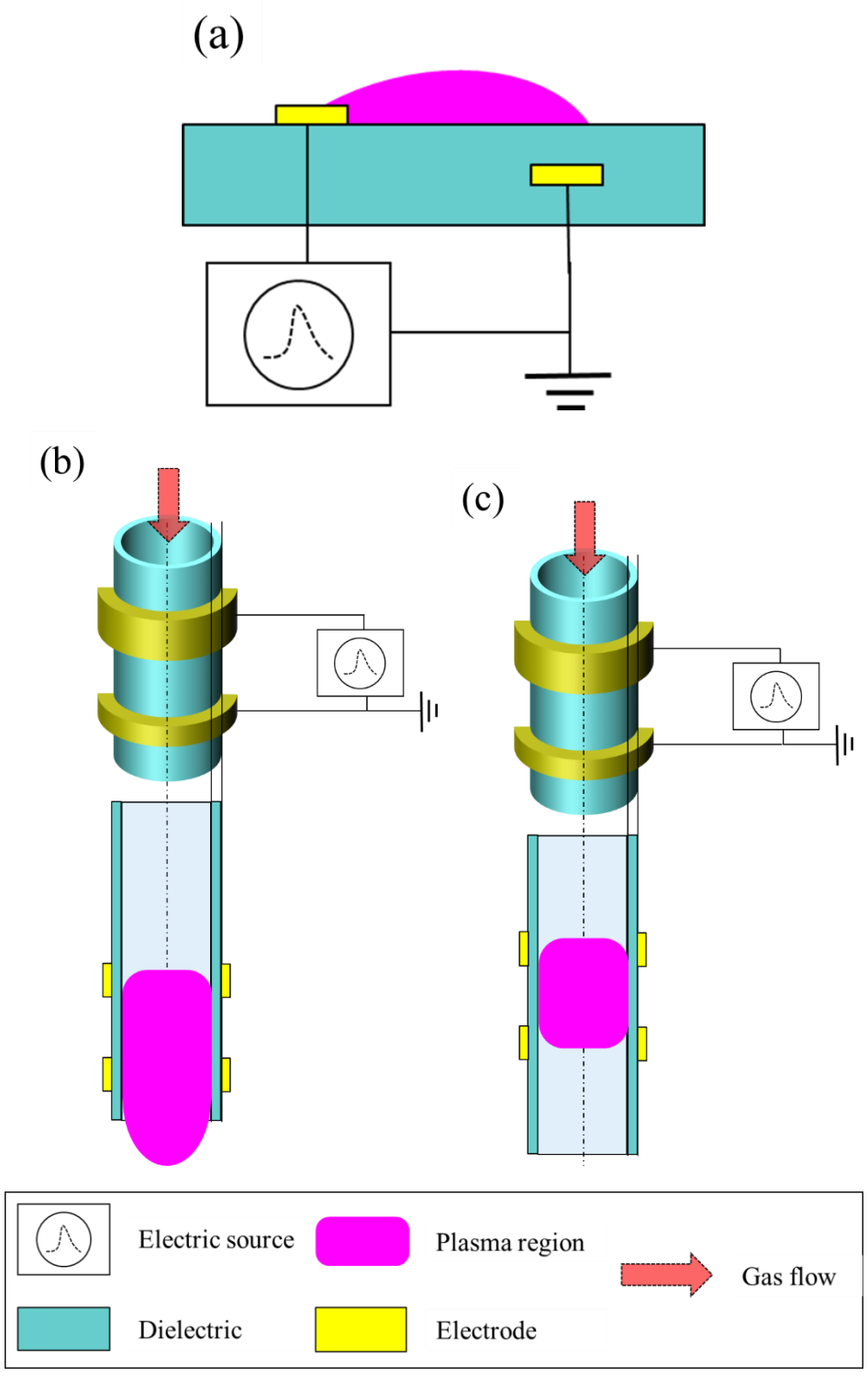

Figure 1.3: Three types of dielectric barrier discharge devices. (a) Planar-type, (b) plasma-jet-type, and (c) reactor-type dielectric barrier discharge devices.

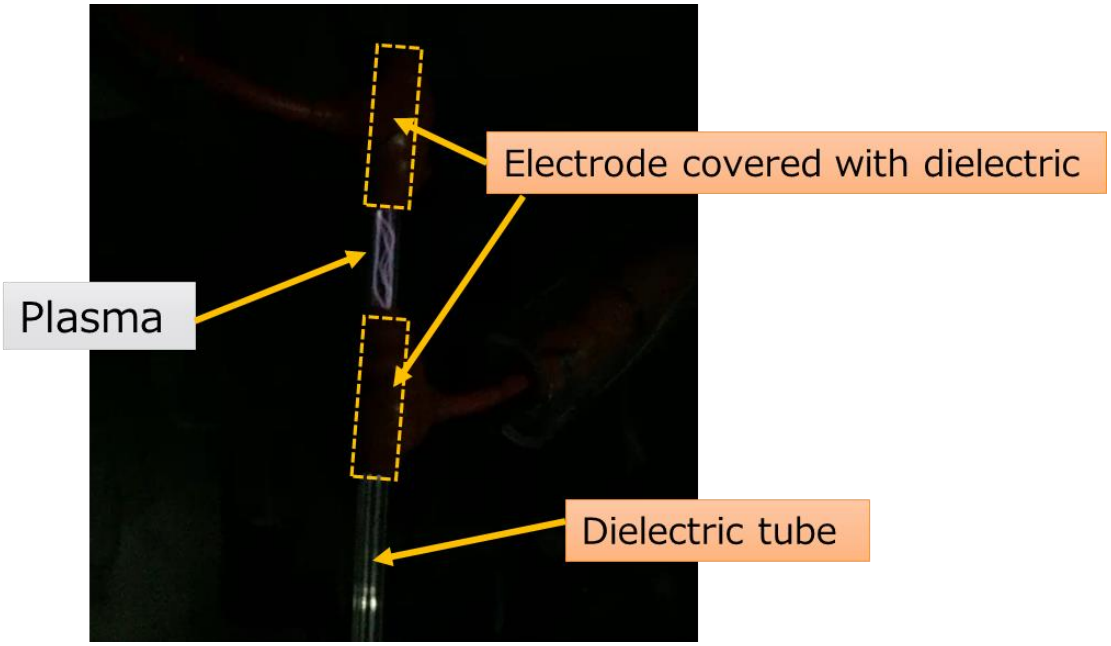

Figure 1.4: Dielectric barrier argon discharge in a coaxial DBD device.

1.2.4 Challenges for application

Although LTAPP has potential applications in various industrial fields, there remain challenges to be solved. It is assumed that many LTAPP applications will be used in scenarios close to human daily life. Therefore, safety is a critically important feature. In order to ensure safety, the following are thought to be important.

- Measures against electric shock incidents.
- Controlling (i.e., suppressing) the transition to arc.
- Understanding by-products and measures for these.
- Understanding the life of electrodes and the system.

Other challenges to be solved before LTAPP applications can be used more widely are thought to be lowering costs of devices and systems (e.g., electric sources), and reducing their power consumption (to improve efficiency).

Moreover, the effects need to be firmly demonstrated in the form of numerical values from experiments. Due to the lack of clarity in standards, it is difficult to realize the effects of LTAPP such as those in existing air purification products, which often result in consumer distrust of plasma applications.

In order to overcome the above challenges, it is once again important to have a deep understanding of physical phenomena. Therefore, both experimental and theoretical (numerical) analyses need to be conducted together.

Main target application of this research is decomposition of odorous gases and volatile organic compounds by LTAPP. These gases basically have a large molecular weight of four or more carbons. Therefore, decomposition processes of these gases are guessed to be complicated. Besides, although it is important to understand the decomposition processes in air when assuming applications in living spaces, understanding decomposition processes in air is challenging because of complicated chemical reactions in air plasma. This research focuses on decomposition processes of gases by noble gas plasmas which have relatively simple chemical reactions. Since the understanding of noble gas plasmas at atmospheric pressure is not sufficient, the author conducts research including understanding the basic phenomena of noble gas plasmas.

1.3 Aims and structure of this thesis

This research attempts to elucidate a deeper understanding of basic plasma phenomena by both experimental measurements and plasma numerical simulations, and to investigate gas decomposition performance by LTAPP as an application with the aim of applying LTAPP in a wide range of industrial fields. The aims of this research are following three contents:

1. To get a deeper understanding of streamer discharge, which is one of the basic phenomena related to LTAPP, by focusing on the propagation properties of primary and secondary streamers in a pin-to-plane geometry.
2. To understand DBD, a fundamental LTAPP phenomenon, focusing on the generation process of plasma inside a reactor-type DBD device.
3. To investigate gas decomposition properties in LTAPP, focusing on decomposition rate, by-products, and the decomposition mechanism.

In addition, the author also aims to construct basic numerical simulation technologies for LTAPP and to establish and assess relevant measurement technologies.

This thesis is structured as follows. Chapter 2 describes the experimental methods and principles utilized in this study, including streak imaging, optical emission spectroscopy, and mass spectrometry (electron ionization and ion attachment mass spectrometry). Chapter 3 provides a discussion of the plasma numerical simulation model. This research uses a self-consistent, multi-species, multi-temperature plasma fluid model. Chapter 4 shows and discusses the results for streamer discharge by experimental and numerical analyses. Chapter 5 presents analyses of coaxial DBD, using numerical simulation to discuss the plasma generation process in a coaxial DBD device. Chapter 6 shows experimental results for gas decomposition by coaxial DBD plasma, discussing the

gas decomposition rate, by-products, and the gas decomposition mechanism. Chapter 7 summarizes the conclusions of this research and describes future work.

References

1. Y. Masutani, N. Nagai, S. Fujita, M. Hayashi, M Kogoma, and K. Tanaka, Plasma Process. Polym. **4**, 41(2007).
2. R. R. Borude, H. Sugiura, K. Ishikawa, T. Tsutsumi, H. Kondo, J. G. Han and M. Hori, Jpn. J. Appl. Phys. **58**, SAAC07 (2009).
3. E.H. Lock, A.V. Saveliev, and L.A. Kennedy, Plasma Chem. Plasma Process **26** 527 (2006).
4. C. Klett, S. Touchard, A. Vega-Gonzalez, M. Redolfi, X. Bonnin, K. Hassouni, and X. Duten, Plasma Sources Sci. Technol. **21** 4 (2012).
5. M. Kogoma and S. Okazaki, J. Phys. D, Appl. Phys. **24** 1985–1987 (1994).
6. H. Tanaka, K. Ishikawa, M. Mizuno, S. Toyokuni, H. Kajiyama, F. Kikkawa, H. R. Metelmann, M. Hori, Rev. Mod. Plasma Phys. **1** 3 (2017).
7. P. M. Bellan, Fundamentals of plasma physics, Cambridge University Press, 2008.
8. K. Akashi, Surface technol. **61** 2 (in Japanese) (2010).
9. L. B. Loeb and J. M. Meek, J. Appl. Phys. **11** 6 438-447 (1940).
10. L.B. Loeb and J.M. Meek, J. Appl. Phys. **11** 7 459-474 (1940).
11. T. Hammer, Plasma Sources Sci. Technol., **11**, A196 (2002).
12. J. S. Chang, Plasma Sources Sci. Technol., **17**, 045004 (2008).
13. G. Friedman, A. Gutsol, A. B. Shekhter, V. N. Vasilets, and A. Fridman, Plasma Process. Polym. **5**, 503 (2008).
14. S. M. Starikovskaia, J. Phys. D: Appl. Phys. **39**, R265 (2006).

15. E. Moreau E, J. Phys. D: Appl. Phys., **40**, 605 (2007).

16. J. P. Boeuf, Y. Lagmich, T. Unfer, T. Callegari, and L. C. Pitchford, J. Phys. D: Appl. Phys., **40**, 652 (2007).

17. R. P. Mildren and R. J. Carman, J. Phys. D: Appl. Phys., **34**, L1 (2001).

18. G. V. Naidis, Phys. Rev. E. **79** 057401 (2009).

19. A. A. Kulikovsky, J. Phys. D: Appl. Phys. **33** 1514 (2000).

20. J. Winter, K. Wende, K. Masur, S. Iseni, M. Dunnbier, M. U. Hammer, H. Tresp, K. D. Weltmann, and S. Reuter, J. Phys. D: Appl. Phys. **46** 295401 (2013).

21. R. Ono, K. Takezawa and T. Oda, J. Appl. Phys. **106** 043302 (2009).

22. A. S. Bleker, J. Winter, S. Iseni, M. D€unnbier, K. D. Weltmann, and S. Reuter, J. Phys. D: Appl. Phys. **47**, 145201 (2014).

23. S. Reuter, J. Winter, S. Iseni, S. Peters, A. Schmidt-Bleker, M. D€unnbier, J. Sch€afer, R. Foest, and K. D. Weltmann, Plasma Sources Sci. Technol. **21** 034015 (2012).

24. O. Eichwald, O. Ducasse, D. Dubois, A. Abahazem, N. Merbahi, M. Benhenni and M. Yousfi, J. Phys. D: Appl. Phys. **41** 234002 (2008).

25. R. Ono J. Phys. D: Appl. Phys. **49** 083001 (2016).

26. X. P. Lu and K. K. Ostrikov, Appl. Phys. Rev. **5** 031102 (2018).

27. P. Bruggeman and R. Brandenburg 2013 J. Phys. D: Appl. Phys. 46 46 (2013).

28. U. Kogelschatz, Plasma Chem. Plasma process. **23** 1-46 (2003).

29. S. Sato, H. Furukawa, A. Komuro, M. Takahashi and N. Ohnishi, Sci Rep **9**, 5813 (2019).

30. R. Sosa, G. Artana, E. Moreau, and G. Touchard. Exp. Fluids. **42** 143 (2007).

31. H. H. Kim 2 Plasma Processes Polym. **1**, 2, 91–110 (2004).

32. G. Xiao, W. Xu, R. Wu, M. Ni, C. Du, X. Gao, Z. Luo, and K. Cen, Plasma Chem.

Plasma Process. **34**, 5, 1033–1065 (2014).

33. C. Xu and X. Tu, J. Energy Chem. **22**, 3, 420–425 (2013).
34. K. Urashima and J. S. Chang, IEEE Trans. Dielectr. Electr. Insul. **7**, 5, 602–614 (2000).
35. T. Wang, B. M. Sun, H. P. Xiao, J. Y. Zeng, E. P. Duan, J. Xin, and C. Li, Plasma Chem. Plasma Process. **32**, 6, 1189–1201 (2012).
36. R. Snoeckx, Y. X. Zeng, X. Tu, and A. Bogaerts, RSC Adv. **5**, 29799–29808 (2015).
37. J. Winter, K. Wende, K. Masur, S. Iseni, M. Dunnbier, M. U. Hammer, H. Tresp, K. D. Weltmann, and S. Reuter, J. Phys. D: Appl. Phys. **46** 295401 (2013).
38. A. R. Hoskinson, L. Oksuz, and N. Hershkowitz, Appl. Phys. Lett. **93**, 221501 (2008).
39. D. Breden, K. Miki, and L. L. Raja, Plasma Sources Sci. Technol. **21**, 034011 (2012).
40. D. Breden, K. Miki, and L. L. Raja, Appl. Phys. Lett. **99**, 111501 (2011).
41. X. J. Shao, N. Jiang, G. J. Zhang, and Z. X. Cao, Appl. Phys. Lett. **101**, 253509 (2012).
42. N. M. Bourdet, M. Laroussi, A. Begum, and E. Karakas, J. Phys. D: Appl. Phys. **42**, 055297 (2009).
43. G. V. Naidis, J. Phys. D: Appl. Phys. **43**, 402001 (2010).
44. Z. S. Chang, C. W. Yao, S. L. Chen, and G. J. Zhang, Phys. Plasmas **23**, 093503 (2016).
45. X. Lu, Z. Jiang, Q. Xiong, Z. Tang, X. Hu, and Y. Pan, Appl. Phys. Lett. **92**, 081502 (2008).
46. S. Gadkari and S. Gu, Phys. Plasmas **24**, 53517 (2017).
47. U. N. Pal, A. K. Sharma, J. S. Soni, S. Kr, H. Khatun, M. Kumar, B. L.Meena, M. S. Tyagi, B. J.. Lee, M. Iberler, J. Jacoby, and K. Frank, J. Phys. D: Appl. Phys. **42** 45213 (2009).
48. X. Li, N. Zhao, T. Fang, Z. Liu, L. Li, and L. Dong, Plasma Sources Sci. Technol. **17**, 015017 (2008).

49. J. Amouroux and S. Cavadias, J. Phys. D: Appl. Phys. **50** 465501 (2017).

Chapter 2 Experimental methods

2.1 Introduction

Determining appropriate applications requires understanding plasma phenomena in detail. It is therefore essential to measure physical quantities that are directly and indirectly related to plasma. This chapter describes the diagnostic methods used in this study.

2.2 Streak imaging

A streak camera is an ultrahigh-speed detector that captures light emission phenomena occurring over extremely short time periods [1, 2]. Streak cameras are widely used for visualizing discharge phenomena and are used for visualization of the streamer discharge in this study. The operating principles of the streak camera used in this study are as follows.

The streak camera consists of a photocathode, focus electrodes, streak tube, and image intensifier, as shown Figure 2.1. The light pulses to be measured (emissions from streamer discharge in this study) are focused onto the photocathode of the streak tube through the slit. The photons are converted into a number of electrons proportional to the intensity of the incident light. These electrons are accelerated and carried toward the phosphor screen, and a voltage is applied to the incident light to sweep the electrons. The electrons are swept at high speed from top to bottom and then bombard the phosphor screen of the streak tube, which is inversely converted to an optical image. When the light intensity of the streak image is very weak, an image intensifier amplifies the low-light-level streak image.

Figure 2.2 shows an example of streak imaging results. This is a visualization of a streamer discharge in air. The horizontal axis represents the position of the light emission from the streamer discharge (mainly the streamer head) and the vertical axis represents time. The discharge moves with time. Streak imaging enables analysis of streamer discharge properties such as propagation speed.

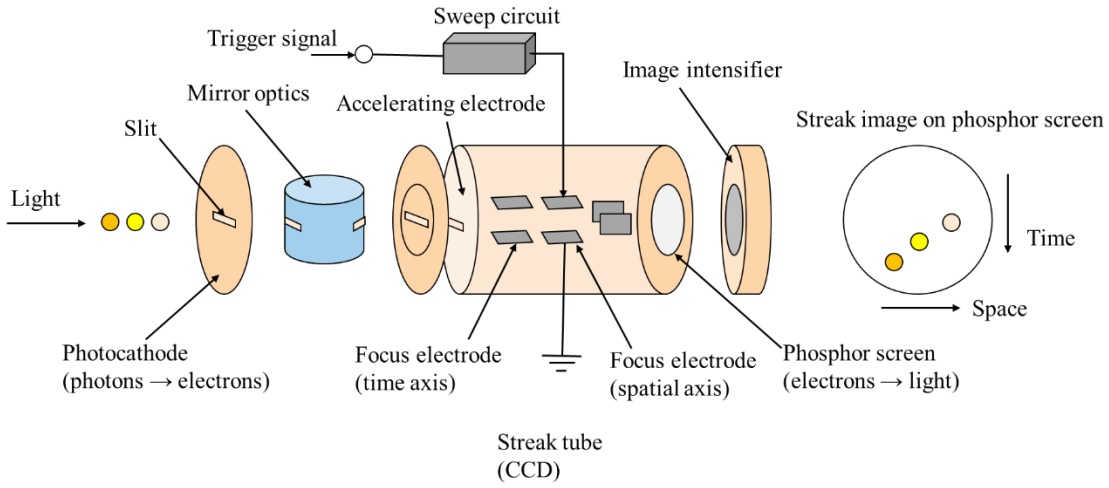

Figure 2.1: Operating principle of streak camera used in this research (created based on [1]).

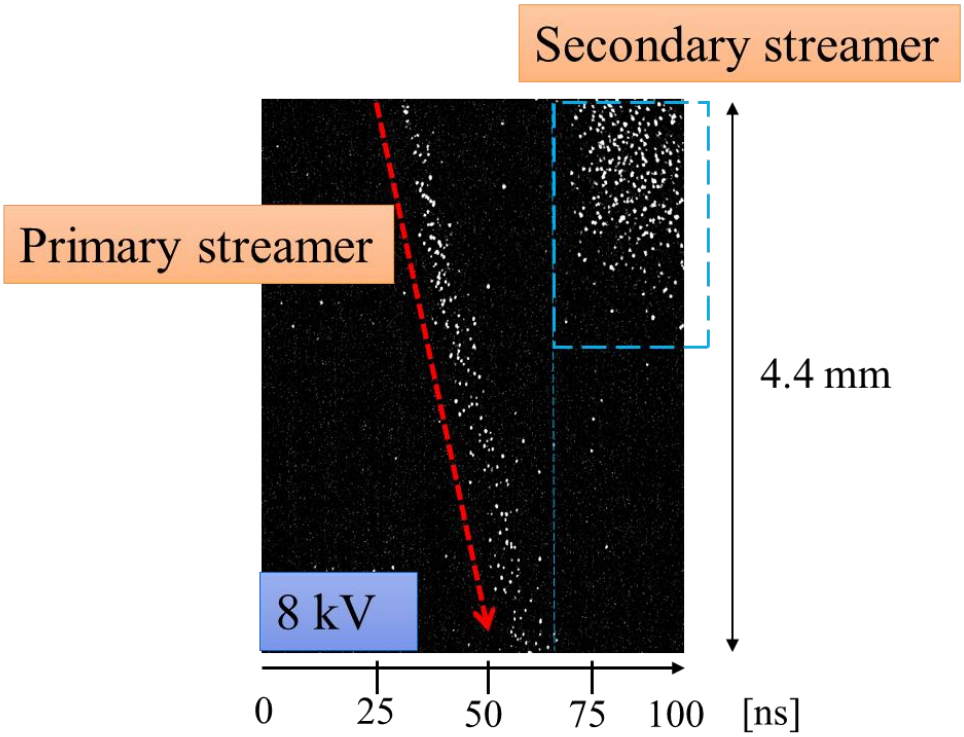

Figure 2.2: Example of streak photograph taken in air.

2.3 Optical emission spectroscopy

Optical emission spectroscopy (OES) is a plasma diagnostics method that analyzes the internal state of the plasma through light emissions from the plasma [2, 3]. OES is widely used because a measurement system can be quickly and easily constructed that facilitates acquisition of measurement data. OES is also a noninvasive method, allowing easy observation of plasma processes without disturbing them.

Generally speaking, the light emission in plasma processes measured by OES is due to bound-bound transition radiation (accompanying transition from an excited level to a low energy level) in the corona state [3]. The corona state is an equilibrium state in which electron impact excitation and radiative de-excitation of active species are balanced, and usual plasma processes are thought to be in this state. In this case, the

emission wavelength λ is related to the difference in energy between the levels involved in the transition:

$$\lambda = \frac{hc}{E_i - E_j}, \tag{2.1}$$

where h is Planck's constant, c is the speed of light, and E_i and E_j are the energies of the upper and lower levels in the transition, respectively. OES provides the number density of excited species in the upper level. Generation number *R* of luminescent excited species generated by electron impact excitation from the ground state per unit time and unit volume is given by

$$R = k_{\mathrm{ex}} n_e n_g, \tag{2.2}$$

where n_e is the electron number density, n_g is the number density of the ground state species before excitation, and k_{ex} is the rate coefficient of excitation, calculated as

$$k_{\mathrm{ex}} = \int_0^{\infty} \sigma(E) f(E) \sqrt{\frac{2E}{m_e}}\, dE, \tag{2.3}$$

where $\sigma(E)$ is the electron-impact excitation cross-section from the ground state to the upper level, E is the electron energy, m_e is the electron mass, and $f(E)$ is the probability density function of the electron energy.

The intensity of each peak in the emission spectrum depends on the electron number density and the electron energy distribution. Therefore, quantitative analysis requires detailed measurement and theoretical calculation of these parameters. In this research, OES is used in qualitative analyses of differences in plasma properties before and after gas decomposition.

Figure 2.3 shows an OES emission spectrum for argon plasma as an example. The horizontal axis shows wavelength and the vertical axis shows emission intensity. For example, the peak at 750.4 nm corresponds to emissions from transition of $1s_2$-$2p_1$.

Emissions from $1s_5$-$2p_9$ (811.5 nm) are also observed. Qualitative changes in plasma properties are analyzed by differences in spectrum elements and intensities between conditions.

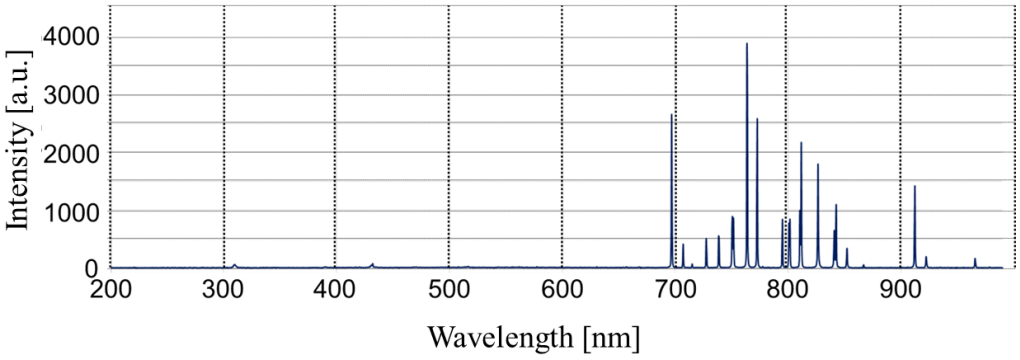

Figure 2.3: Example of OES spectrum (argon plasma).

2.4 Mass spectrometry

Mass spectrometry (MS) is a method for investigating active species present in gases, including plasma. MS analyzes sample molecules utilizing the mass-to-charge ratio *m*/*z* of ionized species. There are several ionization methods, selected according to purpose and target. This study applies two methods. Electron impact ionization is used for analysis of low-pressure plasma. This research also used Li^+ ion attachment to positively ionize the sample molecules. The MS apparatus in this study (L-240G-IA EVP-37024; Canon Anelva Corp.) can be used for both methods.

2.4.1 Electron ionization mass spectrometry

Electron ionization mass spectrometry (EIMS) has been widely applied to analyze low-temperature plasmas, such as those used in semiconductor processes. In

EIMS, sample molecules such as active species in gas are ionized by impact with thermal electrons emitted from a heated filament. The EIMS apparatus comprises an ion source, an ionization part, and an analysis part. The analysis part uses quadrupole mass spectrometry (QMS), which has four hyperbolic cross-sectional shapes. Parts other than the ionization part are the same as in ion attachment mass spectrometry, described in the next subsection, so further description of the apparatus configuration is presented there.

In the ionization process, electrons with energy of about 70 eV collide with sample molecules, and fragmentation of those molecules cannot be ignored. Therefore, identification of mixtures by EIMS alone is difficult, despite information about their molecular structures being obtained [4]. For identification of chemical species, GC/(EI)MS methods can be used in combination with gas chromatography (GC). This is a standard technique in many application fields, but it requires preprocessing, making real-time measurements difficult. This study used EIMS to judge whether sample molecules reach the analysis part and as a complementary method for ion attachment mass spectrometry.

2.4.2 Ion attachment mass spectrometry

In EIMS analyses, fragmentation tends to make analyses of sample molecules difficult. Nakamura et al. developed ion attachment mass spectrometry (IAMS) to realize fragment-free ionization [5, 6]. In IAMS, metal ions such as Li+ attach to and ionize sample molecules, instead of electrons. This prevents fragmentation under appropriate conditions, so only the peak associated with the original molecule is detected [5, 6]. Besides Li^+, other alkali metals such as Na^+ and K^+ are used to ionize the samples. One feature of IAMS is that each obtained peak allows sample molecule identification,

allowing quick and easy measurements in comparison with GC/MS because preprocessing and separation are unnecessary.

Figure 2.4 shows a schematic diagram of an IAMS apparatus. Sample gas molecules at up to about 0.1 Pa are introduced to an ionization chamber, which is filled through an orifice with N_2 to 100 Pa. A turbo molecular pump evacuates the ionization chamber. N_2 at 100 Pa acts as a third-body molecule and has two roles: deceleration of Li^+ ions and removal of surplus energy at attachment. Ions produced by attaching Li^+ to sample molecules are called adduct ions. These are introduced through another orifice into the QMS chamber, where mass spectra are measured. Pressure in the QMS chamber is 1.0×10^{-2} Pa under typical plasma conditions.

Figure 2.5 illustrates ion attachment in IAMS. Ionization progresses through three steps: collision between sample molecules and metal ions, attachment of metal ions to sample molecules, and stabilization of the adduct ions. The reaction by which Li^+ ions and sample molecules attach to form positive adduct ions is represented as follows:

$$\mathrm{Li^+ + M + N \rightarrow MLi^+ + N}, \Delta H = -D(\mathrm{M - Li^+}), \quad (2.4)$$

Here, M is the target sample molecule, MLi^+ is the adduct ion, N is a third-body molecule, ΔH is the enthalpy change, and $D(\mathrm{M - Li^+})$ is the attachment energy of M and Li^+, which corresponds to Li^+ affinity. The above reaction proceeds spontaneously for all molecules because Li^+ affinity for all molecules is positive and the reaction is exothermic and because there is no activation energy in the ion clustering reaction.

Li^+ attaches to negatively charged sites due to charge bias in the sample molecule M by the Coulomb force. For example, Li^+ attaches to O atoms having negative polarization charge in H_2O. In addition, Li^+ can attach to nonpolar molecules such as N_2, because negatively charged sites may be formed by dielectric polarization induced by the

electric field of Li^+. The attachment energy is at most 2 eV and less than the usual interatomic bond of a molecule, and there is no electron transfer. Attachment of Li^+ resembles a hydrogen bond, so molecule fragmentation rarely occurs. In attachment of an isolated system, internal energy due to attachment becomes surplus energy and naturally dissociates in a finite time. This surplus energy must be removed to stabilize adduct ions. This is achieved by collisions with third-body N_2. Figure 2.6 shows the spectrum of butanol ($C_4H_{10}O$) as an example. A peak is observed at m/z = 81, which is the sum of the molecular weights of butanol (74) and Li^+ (7).

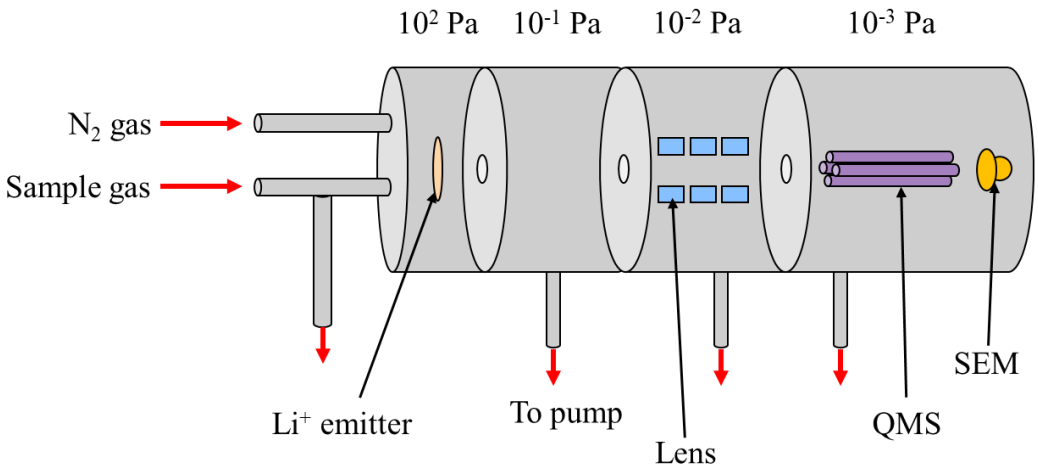

Figure 2.4: Schematic diagram of the ion attachment mass spectrometry apparatus.

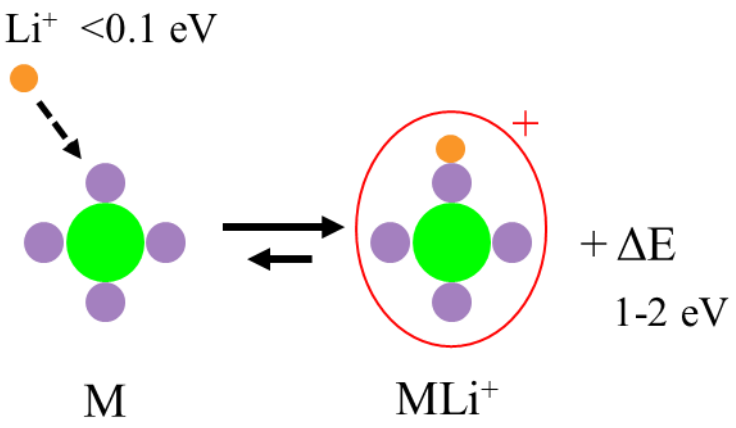

Figure 2.5: The ion attachment process.

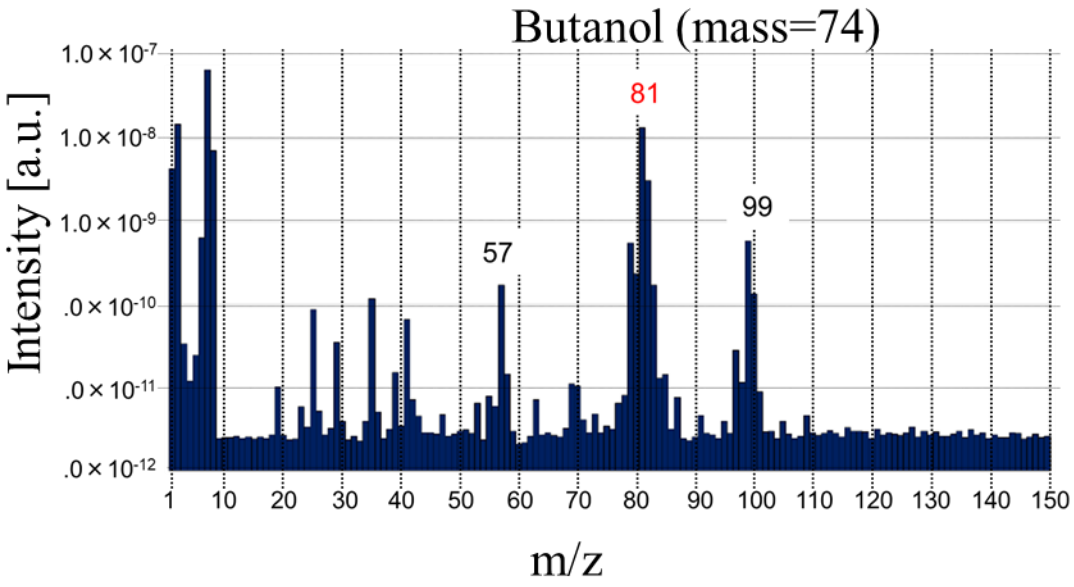

Fig 2.6: Example IAMS spectrum (butanol).

References

1. https://www.hamamatsu.com/jp/en/product/photometry-systems/streak-camera/index.html
2. R. Ono. J. Phys. D: Appl. Phys. **49** 083001 (2016).

3. T. Nakano, J. Plasma Fusion Res. **95** 3 132-138 (in Japanese) (2019).
4. K. Nagato, J. Plasma Fusion Res. **93** 5 236-239 (in Japanese) (2017).
5. N. Nakamura, Y. Hirano, Y. Shiokawa, M. Takayanagi, and M. Nakata, J. Vac. Sci. Technol. A **24** 385 (2006).
6. Y. Shiokawa, M. Nakamura, H. Maruyama, Y. Hirano, Y. Taneda and M. Inoue, J. Vac. Soc. Jpn. **50** 4 (2007).

Chapter 3 Numerical simulation of plasma

3.1 Introduction

This chapter discusses the methods used to model non-equilibrium plasma phenomena and physics. In order to understand the properties of the plasma, the amount and energy state of the particles, the electrostatic potential, and the relations of these to the plasma need to be specified. There are two main methods for analyzing plasma: the particle simulation method and the fluid modeling method. Although it would be ideal to analyze the behaviors of all of the particles in a plasma, this is too computationally expensive and is not realistic. In particle simulations, the concept of "super particles" is introduced to reduce the computational cost. The scope of particle simulations is limited to conditions of low pressure in narrow regions.

Plasma fluid modeling is widely used to analyze plasmas at relatively low computational cost compared with particle simulations. This method has been applied in many LTAPP studies, including this one. This research uses a self-consistent, multi-species, multi-temperature plasma fluid model [1-4]. A commercial plasma solver is used to solve a coupled set of nonlinear governing equations [5].

3.2 Governing equations for non-equilibrium plasma

The governing equations for plasma fluid modeling are the mass conservation equation for each species (continuity equation), electron energy conservation equation, and electrostatic Poisson's equation. There are two characteristic temperatures in non-equilibrium plasma: a heavy species temperature and a separate electron temperature. Each temperature is obtained separately by solving the energy conservation equation. In this study, the heavy species temperature is assumed to be constant and the conservation

equation is not solved.

3.2.1. Species continuity

The number densities of species are obtained by solving separate species continuity equations

$$\frac{\partial n_k}{\partial \mathrm{t}} + \vec{\nabla} \cdot \overrightarrow{\Gamma_k} = \dot{G_k}, \mathrm{k} = 1, \dots, \mathrm{K_{gas}}(\mathrm{k} \neq \mathrm{k_d}) \tag{3.1}$$

for all charged and neutral gas species given by index k, with the exception of a single dominant species given by index k_d (assumed to be ground-state neutral argon or helium). In the above equation, n_k is the number density, $\overrightarrow{\Gamma_k}$ is the number density flux of species k, and K_{gas} is the total number of gas species. The right side of the equation describes the volumetric source term of species $\dot{G_k}$ due to gas-phase chemical reactions. The number density of the dominant background is calculated using an ideal gas law constraint $p = \sum n_k k_B T_k$, where p is the specified gas pressure and T_k is the species temperature.

The species number flux term Γ_k is evaluated using the drift-diffusion approximation

$$\overrightarrow{\Gamma_k} = \mathrm{n_k}\overrightarrow{u_k} = \mu_k n_k \vec{E} - D_k \vec{\nabla} n_k, \tag{3.2}$$

where μ_k is the species mobility, D_k is the species diffusion coefficient, and $\vec{E}$ is the local electric field computed from the negative gradient of the electrostatic potential. This approximation is accurate at high pressures (atmospheric pressure or higher) and room temperature, where the mean free path of ions and neutral species (on the order of a micrometer) are much less than the characteristic scales of the geometry (on the order of a millimeter), and is widely used in studies of atmospheric pressure discharge.

3.2.2. Electron energy transport

Electron temperature T_{e} is determined by solving the electron energy conservation equation

$$\frac{\partial e_e}{\partial \mathrm{t}} + \vec{\nabla} \cdot [(e_{\mathrm{e}} + p_e)\overrightarrow{u_e} + \overrightarrow{q_e}] = \mathrm{e}\overrightarrow{\Gamma_e} \cdot \vec{E} - \mathrm{e}\sum_i \Delta E_i^e r_i - \frac{3}{2}\mathrm{k_B} n_{\mathrm{e}} \left(\frac{2m_e}{m_b}\right)(T_e - T_g)\overline{\nu_e}, \quad (3.3)$$

where the total electron energy $e_{\mathrm{e}} = \frac{3}{2}\mathrm{k_B} T_e n_{\mathrm{e}}$, electron pressure p_{e} follows the ideal gas law, and $\overrightarrow{q_e} = -\kappa_e \vec{\nabla} T_e$ is the electron thermal flux with electron thermal conductivity κ_e. The right side of the electron energy equation includes three source terms: Joule heating, inelastic collisional heating, and elastic collisional heating. The electron unit charge is e, ΔE_i^e is the inelastic collisional energy lost by an electron per collision event as described by the chemical reaction i (in units of eV), and r_i is the rate of progress of the chemical reaction. T_{g} is the heavy species (gas) temperature, m_{e} is the electron particle mass, m_{b} is the background species particle mass, and $\overline{\nu_e}$ is the electron momentum-transfer collision frequency with the background.

3.2.3. Heavy species temperature

The timescale associated with streamer propagation (~ns) is too short for use as a gas dynamic response timescale. Therefore, the background temperature T_{g} is kept at 300 K in all simulations presented below.

3.2.4. Electrostatic potential

The imbalance of net space charge due to the charged species densities generates self-consistent electric field. By assuming that the current densities are small (weakly ionized plasma), magnetic fields can be neglected and the Maxwell equations can be reduced to solving a single Poisson equation for the electric potential. The self-consistent

electrostatic potential ϕ is calculated by Poisson's equation

$$\nabla^2\phi = -\frac{e}{\varepsilon_0\varepsilon_r}\sum_k Z_k n_k, \tag{3.4}$$

where ε_0 is the permittivity of free space, ε_r is the relative permittivity of the material, and Z_k is the charge number of species *k*.

3.3 Plasma chemistry and species transport model

The gas chemistry source terms $\dot{G_k}$ in the species continuity equations are evaluated using a finite-rate chemistry mechanism with a mass-action kinetics formulation. In this research, argon and helium plasma, which are the most widely used gas for plasma applications, are considered.

A pure argon plasma models the following six species: electrons (E), argon ions (Ar^+), argon dimer ions (Ar_2^+), argon composite metastable species (Ar^m), argon dimer metastable species (Ar_2^m), and ground state argon atoms (Ar). Table 1 shows the plasma chemistry model. Reaction pathways for the pure argon reaction mechanism and reaction rate coefficients for non-electron impact reactions are obtained from a previous work [3]. Rate coefficients for electron impact reactions are calculated using an offline zero-dimensional Boltzmann solver BOLSIG+ [6] based on cross-sectional data from the literature [6], and are denoted as EEDF. For surface reaction mechanisms, all excited and charged species are assumed to be quenched with a unity-sticking coefficient.

Closure of the governing equations requires specification of transport properties, mobility μ_k and diffusion coefficient D_k for all ions and neutral species, and the thermal conductivity of electrons κ_e. Mobility and diffusion coefficients for electrons are calculated offline using the BOLSIG+ solver and tabulated as a function of the electron

temperature T_e. Thermal conductivity is computed as $\kappa_e = \frac{5}{2} k_B D_e n_e$. The mobility of argon ions is specified as a function of the local reduced electric field, as described in Ref. [3]. Diffusion coefficients are computed using Einstein's relation. For neutral species, the transport properties are calculated using cross-sections.

Photoionization plays an important role in streamer propagation [7,8]. In air, radiation from the de-excitation of N_2 molecules can photoionize surrounding O_2 molecules and enhance the streamer propagation speed [8]. Further, Breden et al. [9] showed that the photoionization mechanism significantly impacts the speed of streamer propagation, but is not necessary for propagation. This research does not consider the photoionization because we focus on qualitative understanding of streamer propagation and plasma generation, and do not consider O_2 molecules, which are considered as the main radiation receptors. When quantitatively comparing results with experimental data, the photoionization mechanism may be important.

Table 1. Argon plasma chemistry model.

Rxn	Reactions	Reaction rate coefficient [a]	Ref.
G_1	$E + Ar \rightarrow E + Ar^m$	$1.0\times10^{-8}\ T_e^{0.1}\ \exp(-1.38\times10^5/T_e)$	[6]
G_2	$E + Ar \rightarrow 2E + Ar^+$	EEDF	[6]
G_3	$E + Ar^m \rightarrow 2E + Ar^+$	EEDF	[6]
G_4	$E + Ar^m \rightarrow E + Ar$	EEDF	[6]
G_5	$E + Ar_2^m \rightarrow 2E + Ar_2^+$	$1.29\times10^{-7}\ T_e^{0.7}\ \exp(-0.42\times10^5/T_e)$	[6]
G_6	$E + Ar_2^m \rightarrow E + 2Ar$	10^{-7}	[6]
G_7	$E + Ar^+ \rightarrow Ar^m$	$4.0\times10^{-13}Te^{-0.5}$	[6]
G_8	$2E + Ar^+ \rightarrow E + Ar^m$	$5.0\times10^{-27}Te^{-4.7}\ cm^6/s$	[6]
G_9	$E + Ar_2^+ \rightarrow Ar + Ar^m$	$5.38\times10^{-8}Te^{-0.66}$	[6]
G_{10}	$2Ar^m \rightarrow E + Ar + Ar^+$	5.0×10^{-10}	[3]
G_{11}	$Ar_2^m \rightarrow 2Ar$	$6.0\times10^7\ /s$	[3]
G_{12}	$2Ar_2^m \rightarrow E + Ar_2^+ + 2Ar$	5.0×10^{-10}	[3]
G_{13}	$Ar^m + 2Ar \rightarrow Ar_2^m + Ar$	$1.14\times10^{-32}\ cm^6/s$	[3]
G_{14}	$Ar^+ + 2Ar \rightarrow Ar_2^+ + Ar$	$2.5\times10^{-31}\ cm^6/s$	[3]

[a] Units of cm^3/s for two-body reactions and cm^6/s for three-body reactions.

3.4 Boundary conditions

This section describes boundary conditions for each equation. Specific settings are described in each chapter.

3.4.1. Boundary conditions for species continuity equation

Solid surface flux

For the electron continuity equation, the electron flux at solid walls (electrodes and dielectric surfaces) is specified as follows

$$\overrightarrow{\Gamma_e}\cdot\widehat{n_s} = \frac{1}{4}\mathrm{n_e}\left(\frac{8k_bT_e}{\pi m_e}\right)^{\frac{1}{2}} - \gamma\overrightarrow{\Gamma_{\mathrm{Ar^+}}}\cdot\widehat{n_s}, \tag{3.5}$$

where $\widehat{n_s}$ is the unit normal vector pointed toward the wall and γ is the secondary

electron emission coefficient of Ar^+ ion for the given surface. The first term assumes that the electron energy distribution is nearly Maxwellian close to the surface and is characterized by an electron temperature.

For the ions the flux of positive ions is set to 0 for all solid boundaries for which the electric field points away from the wall ($\vec{E} \cdot \widehat{n_s} < 0$). If the electric field points toward the wall ($\vec{E} \cdot \widehat{n_s} > 0$), the ion flux is extrapolated from the interior by imposing a zero gradient of the ion flux at the boundary. The Maxwellian flux condition is imposed for the neutral species as $\gamma = 0$ in the Eq. (3.5).

Symmetry

A symmetry boundary condition can be imposed at boundaries by specifying that the flux of species normal to the boundary is zero

$$\overrightarrow{\Gamma_e} \cdot \widehat{n_s} = 0. \tag{3.6}$$

Axis

The axis boundary condition has the same meaning in the context of the species density equation as the symmetry boundary condition. The axis boundary condition imposes a zero number flux of species normal to the boundary

$$\overrightarrow{\Gamma_e} \cdot \widehat{n_s} = 0. \tag{3.7}$$

3.4.2. Boundary conditions for electron energy equation

Solid surface flux

For electron energy equation, the total electron energy flux at the solid walls is given as

$$\overrightarrow{Q_e} \cdot \widehat{n_s} = 2\mathrm{k_b} T_e \overrightarrow{\Gamma_e} - e\Delta E^{se} \gamma \overrightarrow{\Gamma_{\mathrm{Ar}^+}}, \tag{3.8}$$

where $\overrightarrow{Q_e} = (e_\mathrm{e} + p_e)\overrightarrow{u_e} + \overrightarrow{q_e}$ is the total electron energy flux and ΔE^{se} is an average electron energy.

Symmetry

A symmetry boundary condition can be imposed at boundaries by specifying the total flux of electron energy to the boundary

$$\overrightarrow{Q_e} \cdot \widehat{n_s} = 0. \tag{3.9}$$

Axis

The axis boundary condition has the same meaning in the context of the electron energy equation as the symmetry boundary condition

$$\overrightarrow{Q_e} \cdot \widehat{n_s} = 0. \tag{3.10}$$

3.4.3. Boundary conditions for Poisson's equation

Fixed potential

A fixed boundary potential is imposed at boundaries as follws.

$$\phi = \phi_b, \tag{3.11}$$

where, ϕ_b is the specified potential at the boundary.

Continuous (surface charge)

When a solid surface is a dielectric, a charge accumulation occurs at the dielectric surface. The surface charge density ρ_s that accumulates on the dielectric surface is given by

$$\frac{\partial \rho_s}{\partial \mathrm{t}} = \sum_{k=1}^{K_{gas}} eZ_k \overrightarrow{\Gamma_k} \cdot \widehat{n_s}. \tag{3.12}$$

Symmetry

A symmetry boundary condition can be imposed at boundaries by specifying that electric field normal to the boundary surface is zero as follows.

$$\nabla\phi \cdot \widehat{n_s} = 0. \tag{3.13}$$

Axis

The axis boundary condition has the same meaning in the context of the Poisson's equation as the symmetry boundary condition

$$\nabla\phi \cdot \widehat{n_s} = 0. \tag{3.14}$$

3.5 Computational methods

The set of governing equations is solved with a cell-centered finite volume discretization on an unstructured mesh framework, using a commercial plasma solver [5]. The special discretization of flux terms at cell faces is evaluated using the Scharfetter–Gummel exponential scheme [10] for transport Eqs. (3.1) and (3.3). A first-order backward Euler method is used for time-derivative terms. The electrostatic Poisson's equation is solved using a semi-implicit approach [11].

References

1. D. Breden, L. L. Raja, C. A. Idicheria, P. M. Najt, and S. Mahadevan, J. Appl. Phys. **114** 083302 (2013).

2. L. L. Raja, S. Mahadevan, L. Peter, G. Ventzek and J. Yoshikawa, J. Vac. Sci. Technol. A **31** 031304 (2013).
3. T. Deconinck and L. L. Raja, Plasma Process. Polym. **6** 5 335–346 (2009).
4. Y. Sato, K. Ishikawa, T. Tsutsumi, A. Ui, M. Akita, S. Oka, and M. Hori, J. Phys. D: Appl. Phys. **53**, 265204 (2020).
5. VizGlow: Plasma Modeling Software for Multi-Dimensional Simulations of Non-Equilibrium Glow Discharge Systems, User Manual, Version 2.2 (Esgee Technologies Inc.).
6. G. Hagelaar and L. Pitchford, Plasma Sources Sci. Technol. **14** 4 722 (2005).
7. G. V. Naidis, J. Phys. D: Appl. Phys. **30** 1214 (1997).
8. A. Bourdon, V. P. Pasko, N. Y. Liu, S. Celestin, P. Segue, and E. Maroude, Plasma Sources Sci. Technol. **16**, 656 (2007).
9. D. Breden, K. Miki, and L. L. Raja, Appl. Phys. Lett. **99**, 111501 (2011).
10. D. L. Scharfetter and H. K. Gummel, IEEE Trans. Elec. Dev. **16** 64-77 (1969).
11. L. L. Raja, S. Mahadevan, P. L. G. Ventzek and J. Yoshikawa, J. Vac. Sci. Technol. A **31** 031304 (2013).

Chapter 4 Study on atmospheric pressure streamer discharge

4.1 Introduction

Streamer discharge is a fundamental part of atmospheric pressure plasma phenomena. In order to properly apply LTAP technologies, understanding of the streamer discharge is important. Energetic studies in recent years have led to a better understanding of propagation characteristics of the streamer discharge and formation processes of chemical species in air.

However, it is difficult to measure streamer properties in detail owing to the small volume, high propagation speed, and randomness. Numerical simulations also have difficulties analyzing streamer phenomena because of they are non-stationary, have steep gradients of physical valuables, and rely on multiphysics features. As a result, streamer phenomena are not completely understood. In particular, there are few studies on streamer discharges in noble gases under the atmospheric pressure and the understanding of that is not sufficient. Understanding of noble gas plasmas is also important in order to analyze gas decomposition properties by noble gas plasmas.

This research conducts both experimental and numerical analyses of streamer propagation properties such as propagation speed and the secondary streamer on the nanosecond-to-microsecond timescale.

4.2 Experimental analysis

Experimental analysis of streamer discharge in air and argon are presented in this section. The results in this subsection are used for qualitative analysis of streamer discharges.

4.2.1. Experimental setup

Figure 4.1 shows a schematic of the streak imaging setup for measuring streamer discharges. The experimental system consists of discharge, streak imaging, and electrical measurement components. The discharge component of the target is a simple pin-to-plane electrode geometry, comprising copper pin and plane electrodes. The gap distance between the pin and plane electrodes is adjustable, and a high voltage is applied to the pin electrode while the plane electrode is earthed. Voltage from the electrical source (function generator) is boosted through an amplifier from several volts to several kilovolts. The streak imaging part consists of a trigger system, streak camera, and CCD camera (Hamamatsu photonics). In order to visualize streamer propagation, streak photographs are taken during the discharge using the function generator as a trigger. A lens is attached to the CCD camera to adjust the field of view and brightness, and the tip of the lens is placed 46.5 mm from the discharge part. The applied voltage waveform is a square pulse of several kilovolts with 20% duty. A high-voltage probe and current monitor are used to measure the voltage and current.

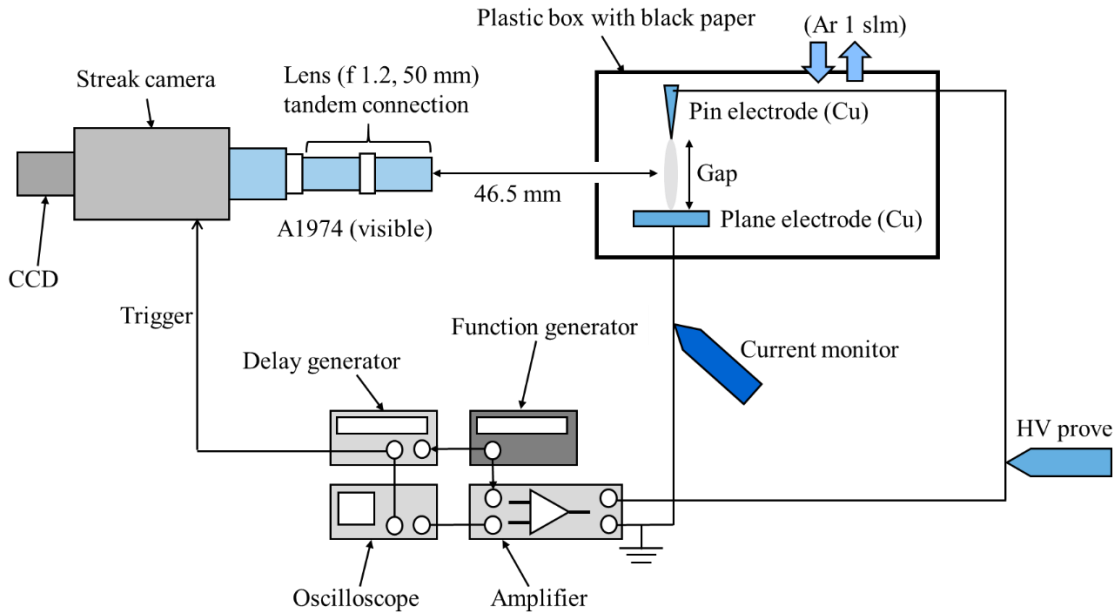

Figure 4.1: Experimental setup for measurement of streamer discharge.

4.2.2. Results and discussion

4.2.2.1. Visualization of streamer discharge

Figure 4.2 shows streamer discharge emissions captured by the digital camera. Streamer discharge was reproduced in air and argon. As shown in the Figure 4.2, strong emissions are observed near the pin electrode and near the plane electrode, and the streamer discharges were observed repeatedly in both cases.

It has been confirmed that streamer discharge has four spatially distinct regions that depend on the characteristics of the reactive species production [1]. The area within a 1 mm radius of the pin electrode tip is referred to as the “hot anode region” because of its very high temperature under some conditions, and the area near the plane electrode is referred to as the “near-cathode region”. Other areas include the secondary streamer region and primary streamer region, which are important for volumetric processes such as gas removal because of their large volume. In addition, the secondary streamer is

important for applications that require high processing rates.

On the other hand, in the streamer discharge in argon, four distinct regions were not clearly confirmed. As discussed later with voltage and current waveforms, the discharge condition for the argon was too strong to sustain the streamer discharge, resulting in a short circuit due to the overcurrent.

Figure 4.3 shows photographs of streamer discharge with different gap distances between the electrodes (2, 3, and 5 mm) and different repetition frequencies of the applied voltage (10, 100, 500, and 1000 Hz). The applied voltage was fixed 10 kV. At a gap of 2 mm, spark discharge occurred at 500 and 1000 Hz, so these conditions are not shown. In all conditions shown in Figure 4.3, light emission from the streamer discharge was observed between the left pin and right plane electrodes. One major trend was that the streamer discharges often reached different locations on the plane electrode and often split into multiple paths. These phenomena are called “deviations” and “branching”, respectively, and are known to be basic properties of streamer discharge. Snapshots at the moment when these phenomena occurred are also shown in Figure 4.3. For the small gap of 2 mm, the deviation was small and appeared to be within a 1 mm radius in the image and animation. As the gap was increased to 3 mm and 5 mm, the degree of deviation and branching increased, and in the case of 5 mm, it even reached the edge of the plate electrode.

Differences were also observed between frequencies. When the gap was 3 mm, the deviation was relatively small at 10 Hz and 1000 Hz, with light emission observed at almost the same position. However, at 100 Hz and 500 Hz, deviations were seen frequently, and it seemed that deviations were at most about 2 mm. In the case of the 5 mm gap, differences between frequencies were not very large, and deviation was observed

at all frequencies. At gaps of 3 mm and 5 mm, there were cases where multiple lines of light occurred at the same time, for example for 5 mm at 100 Hz and 3 mm at 500 Hz. Although it was not known whether they occurred simultaneously due to limitations on the time resolution, it was thought that the next discharge was generated along another path at least while the previous light emission (excited species) remained.

From the viewpoint of electric resistance, although it was expected that the space through which the streamer had passed would be easier for electricity to flow, owing to the presence of the remaining charged particles (electrons and ions), this was not always the case. The characteristics of the discharge also changed owing to fluctuations in the surrounding physical quantities and the microscopic shape of the tip of the pin, and possibly also owing to stochastic factors such as stray electrons that happen to be present. To analyze the deviation and branching in more detail, it is necessary to acquire more data and construct a more detailed measurement device that enables analysis from a statistical point of view. Results from the present visualizations suggest that the frequency and magnitude of deviation and branching increase as the gap increases.

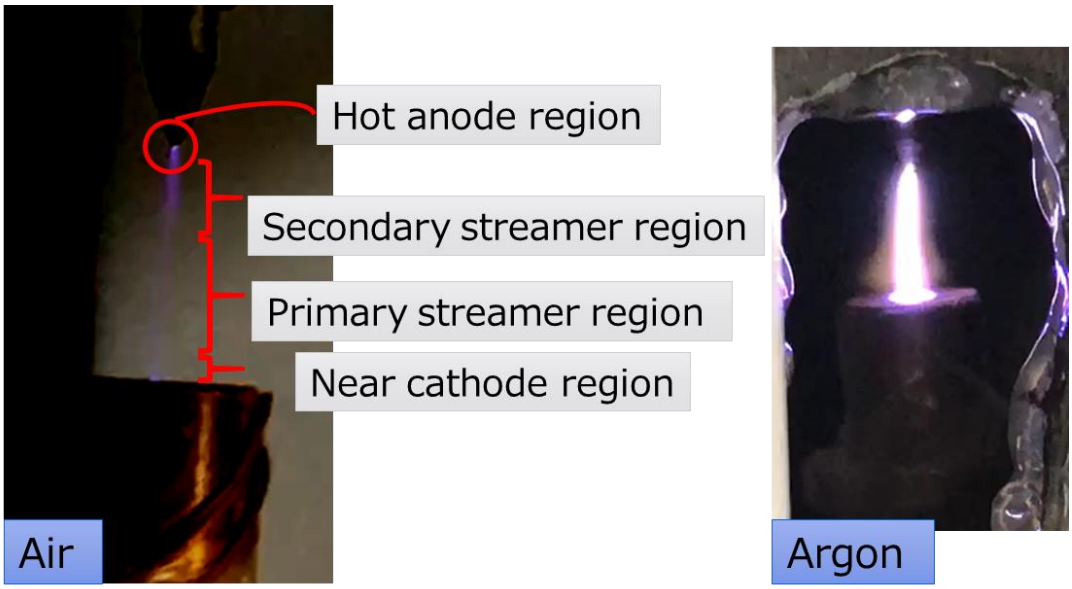

Figure 4.2: Pictures of streamer discharges in air and argon under the pin-to-plane electrode geometry. Left figure shows the discharge in air under the condition of 5 kHz repetitive frequency, 7 mm gap and 8 kV voltage. Right figure shows the discharge in argon under the condition of 1 kHz repetitive frequency, 5 mm gap and 10 kV voltage.

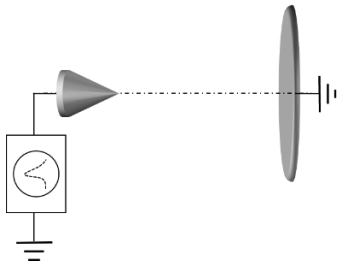

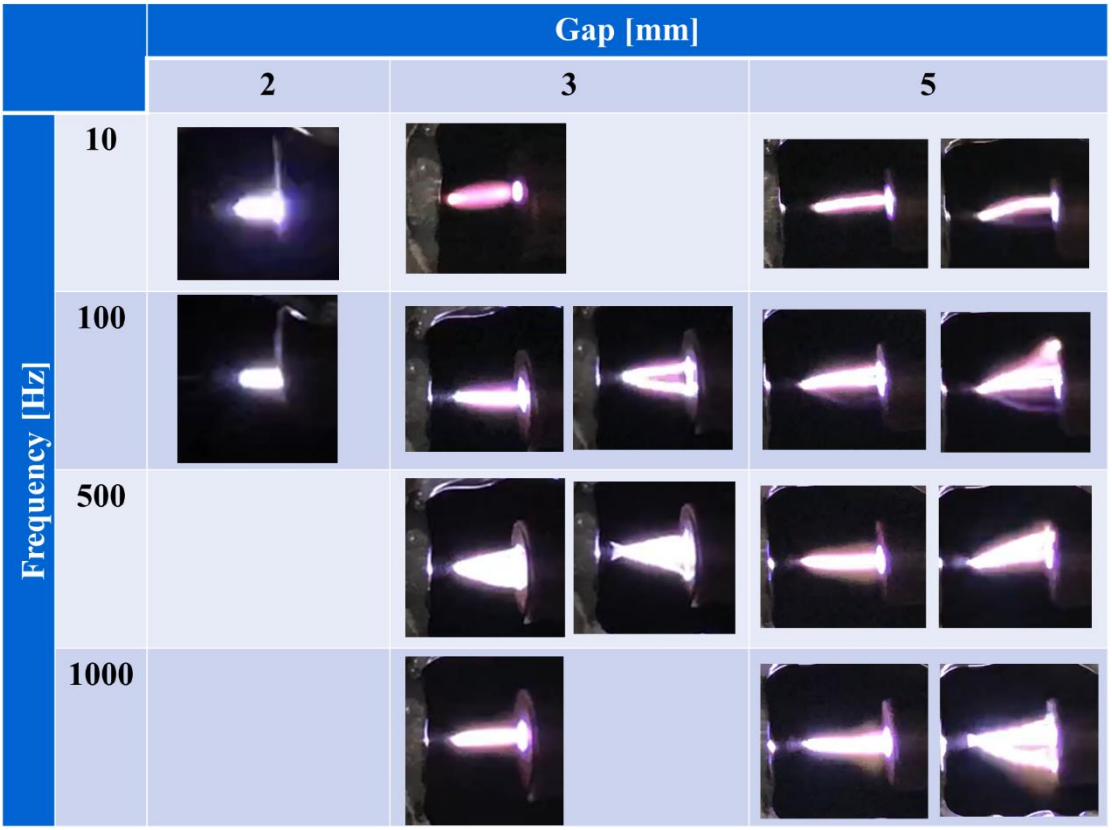

Figure 4.3: Photographs of streamer discharges in argon under different gaps and repetitive frequencies. The applied voltage is 10 kV. Light emissions from streamer discharges, deviation and branching are observed.

4.2.2.2. Voltage and current measurement

Figures 4.4(a) and (b) show the measured voltage and current waveforms for the cases of a 7 mm gap, 5 kHz repetitive frequency in air. The applied voltage is 8 kV and 9 kV, respectively. Figure 4.4(c) shows the measured voltage and current waveforms for the condition of 2 mm gap, 10 Hz and 10 kV in argon. Blue lines show voltages and orange lines show currents. Peaks in the orange lines are thought to correspond to the arrival of the primary streamer head at the plane electrode. The first peak in the currents is mainly composed of a displacement current produced by the temporal change in the electric field induced by the approach of the streamer head to the plane electrode. The oscillations after the first current peak continued for approximately 500 ns.

There were differences in voltage waveforms between air and argon cases. In air, the voltage drop was not observed at the time of the current peak. In argon case (Figure 4.4(c)), however, a voltage drop was observed at the time of the current peak, and the timescale was approximately 60 ns. The reason for this voltage drop was that the current in the argon streamer discharge was likely to have exceeded the limit of the power source. The currents in the argon discharge was ten times larger than that of air cases. Similar voltage drops were observed in all the argon cases. Therefore, it was difficult to discuss discharge currents in argon streamer discharges in this research.

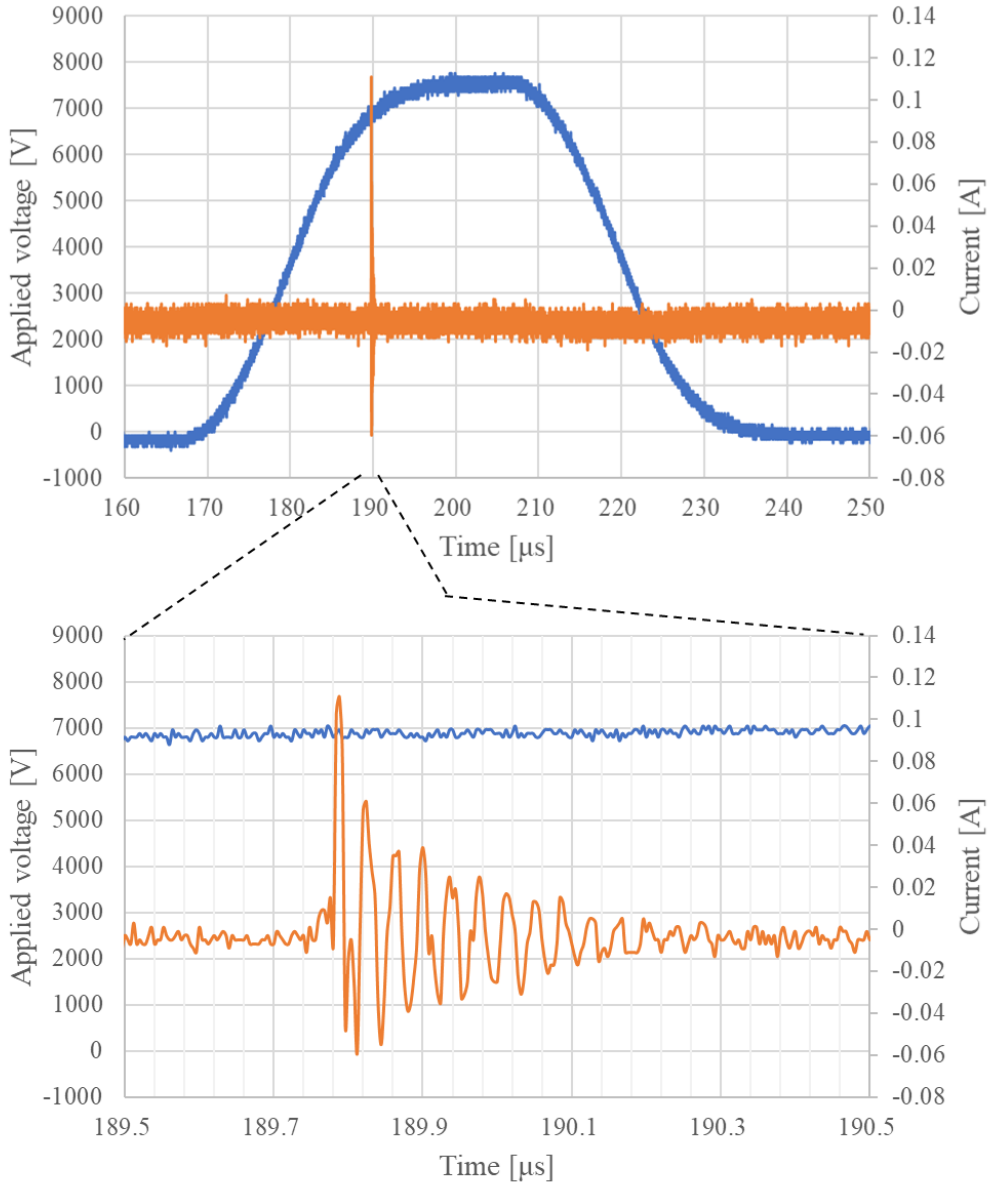

(a) 7 mm, 5 kHz, 8 kV in air.

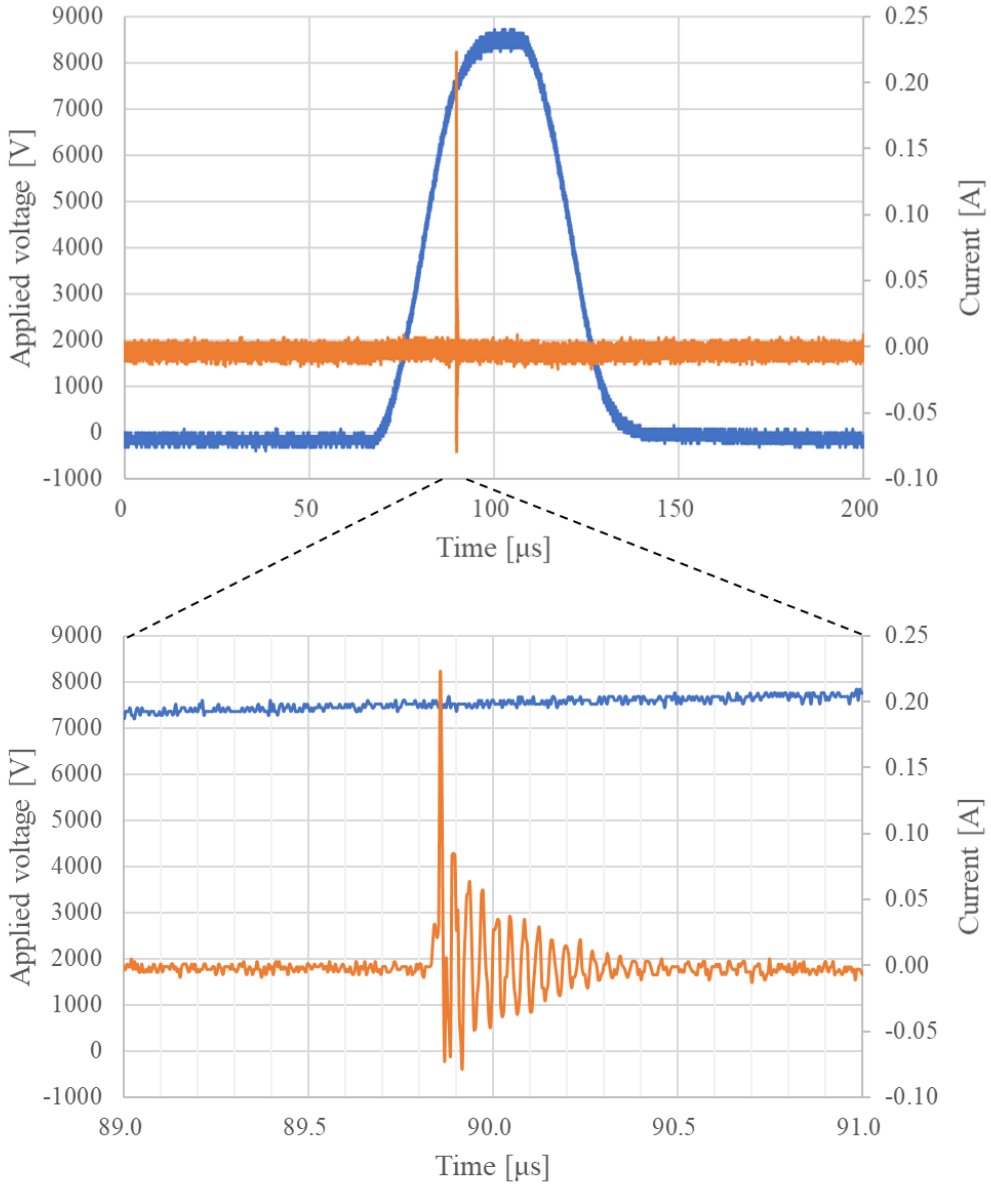

(b) 7 mm, 5 kHz, 9 kV in air.

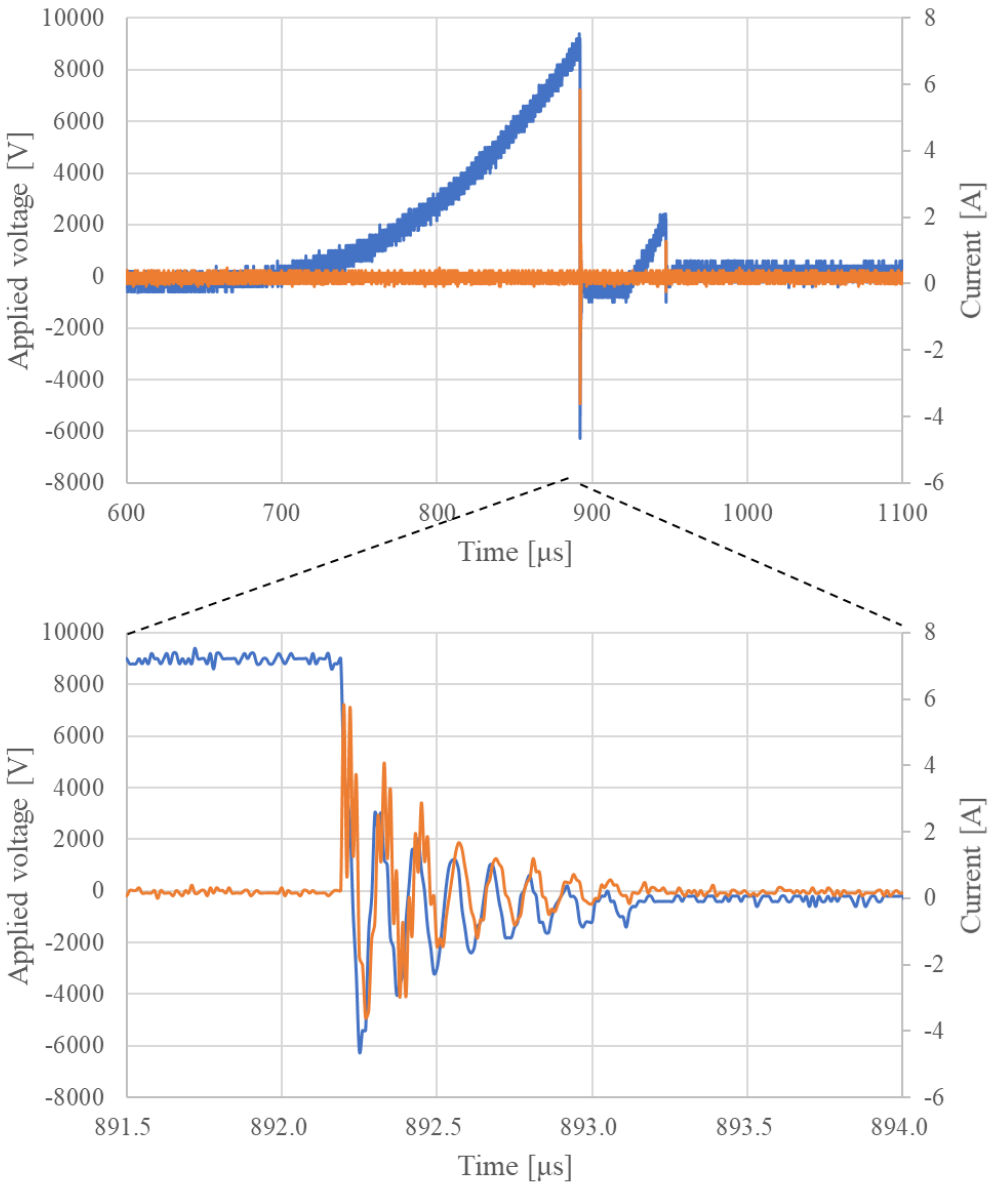

(c) 2mm, 10 Hz, 10 kV in argon.

Figure 4.4: Voltage and current waveforms measured in air and argon streamer discharges.

4.2.2.3. Streak imaging

To observe streamer propagation, visualization was performed by streak imaging. Figure 4.6 shows the streak pictures under 8 kV and 9 kV conditions. The gap between

the electrodes was set to 7 mm. The primary streamer propagates from the pin electrode to the plane electrode at almost constant speed and takes about 20 ns to reach the plane. The propagation speeds were estimated to be about 0.17×10^6 m/s and 0.22×10^6 m/s in the 8 kV and 9 kV cases, respectively, and these were equivalent to or slightly slower than previous studies [2].

After the primary streamer reaches the plane electrode, the high emission region extended from the pin toward the plane again. This is the emission in the secondary streamer. The secondary streamer extended more in higher voltage condition of 9 kV.

It was not possible to perform measurement under a wide range of conditions, owing to problems such as discharge stability, synchronization of shooting timing, and deviation and branching inherent to the streamer discharge itself. For the same reasons, streak pictures under argon gas conditions were not obtained in this study. In order to analyze streamer discharge in more detail, a more advanced measurement system is required. For more detailed analyses, this research utilizes numerical simulations as presented in the next section.

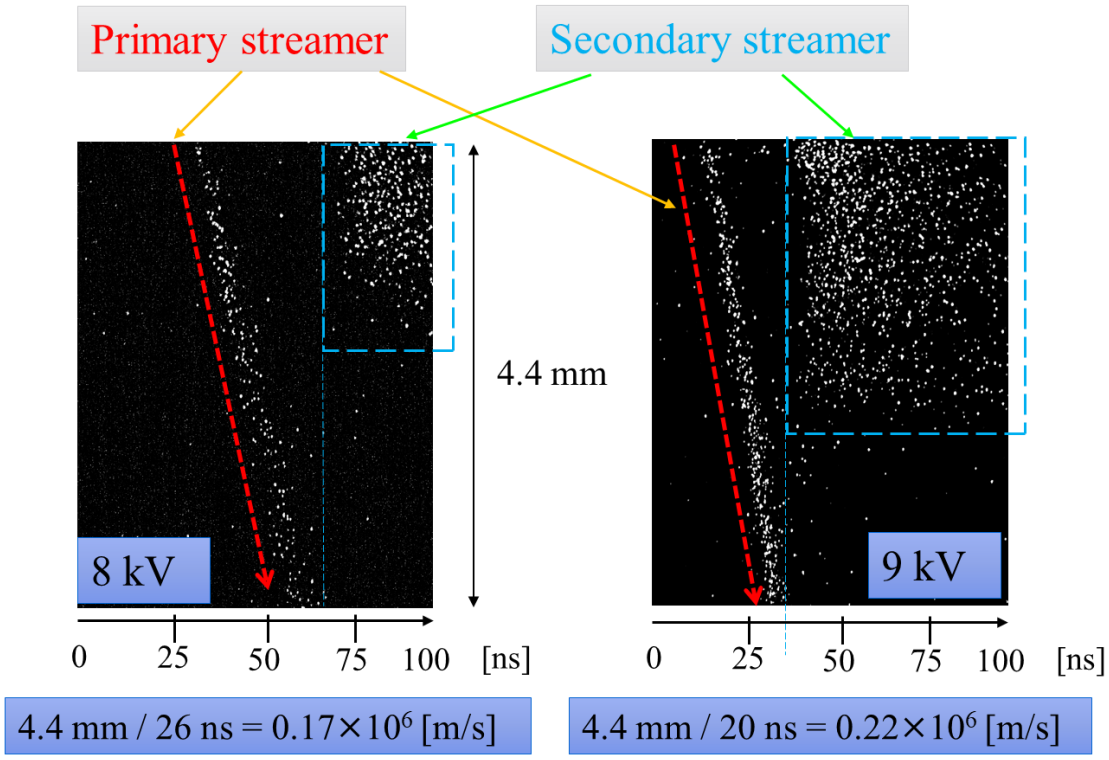

Figure 4.6: Streamer propagation in air observed using streak imaging. Primary and secondary streamers are observed under conditions of 7 mm gap, 5 kHz repetition frequency for 8 kV and 9 kV cases.

4.3 Analysis by numerical simulations

This section provides an analysis of streamer discharge by plasma numerical simulations. As described in the previous section, the data obtained by experimental observation were limited owing to the features of the streamer discharge itself. Therefore, this section focuses on computational approaches for determining the spatiotemporal behaviors of streamer discharges that occur on the order of nanoseconds. This research investigated the fundamentals of atmospheric pressure discharges in noble gases by taking a computational approach to evaluate the key parameters for propagation speeds and streamer head shapes. Plasma generation in atmospheric pressure argon discharges is

compared for cases of applied voltage polarity in a pin-to-plane electrode geometry. This research found that using a negative polarity applied voltage on the pin electrode provided characteristic parameters. This research examined this in computational plasma simulations based on continuum modeling.

4.3.1. Simulation conditi1ons

This research considers the simple pin-to-plane electrode geometry shown in Figure 4.7, corresponding to experimental setup. The inter-electrode distance between the pin and the plane electrode is fixed at 2 mm. The pin electrode form is a hyperboloid of revolution with radius 100 μm, corresponding to that used in previous works [3, 4]. The material for both electrodes is assumed to be copper.

A constant DC voltage is applied to the pin electrode, and the plane electrode is fixed to 0 V. Experimentally observed voltage waveforms in the streamer discharge usually have a rise and fall time [4], but we used a constant voltage in this research because we found no data for argon streamer discharge at atmospheric pressure.

Figure 4.8 shows the computational mesh. The geometry is modeled as axisymmetric, and a hybrid mesh is used. A geometrically flexible unstructured mesh is placed near the tip of the pin electrode, and a structured mesh is placed in the region where the streamer discharge propagates. The minimum mesh size is 1 μm near the pin electrode, and the maximum mesh size is about 10 μm. The computational region in the radial direction is 3 mm. The total number of computational cells is about 440,000.

The boundary conditions are for a flux boundary condition at the pin electrode and a symmetric boundary at the plane electrode and outer boundaries. Previous studies [3, 4,] reported that simulations with flux boundary conditions at the plane electrode tend

to be unstable when secondary electron emission is considered, so we used symmetric boundary conditions at the plane electrode without secondary electron emission.

The background gas pressure is set at 1 atm, temperature is set at 300 K, and density follows the ideal gas law. Initial densities for all other species, including electrons and charged species, are set at 10^9 m^{-3}. Neutral gas flow is assumed to be stagnant, and the initial conditions are set uniformly throughout the computational region. The time step is set at 10^{-12} s.

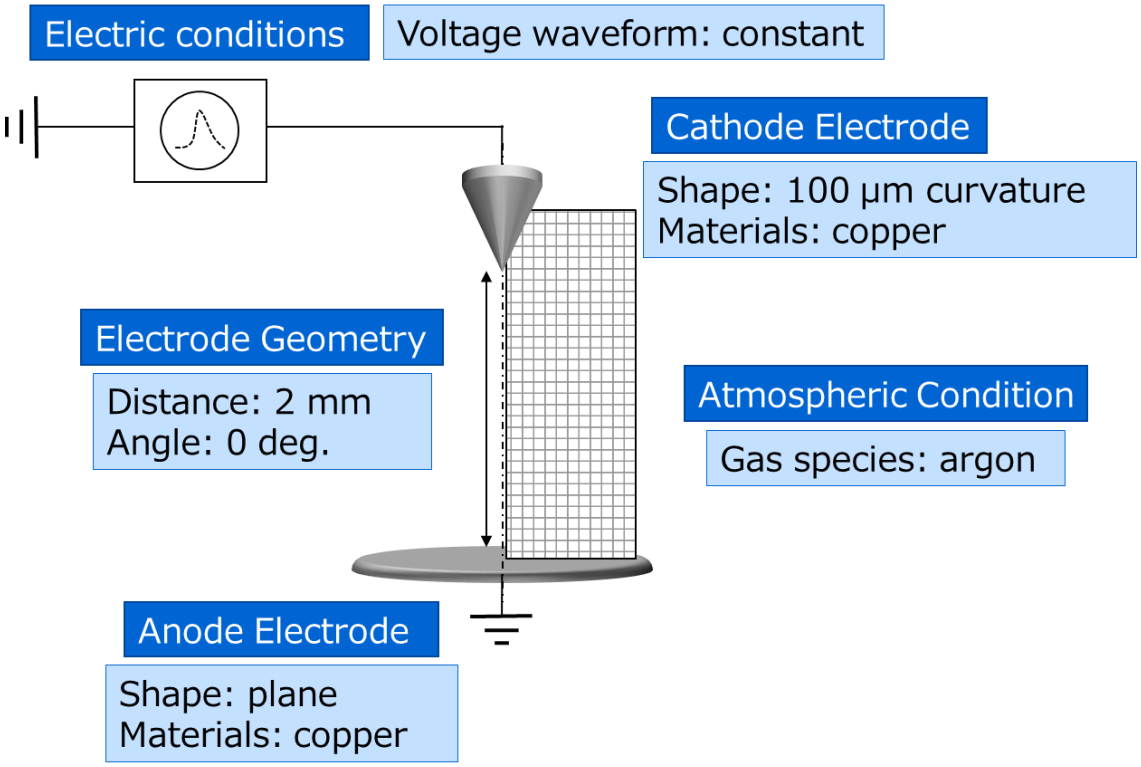

Figure 4.7. Geometry and simulation conditions in this research [5]. Simple pin-to-plane geometry is considered and the voltage is applied to the pin electrode whereas the plane electrode is earthed.

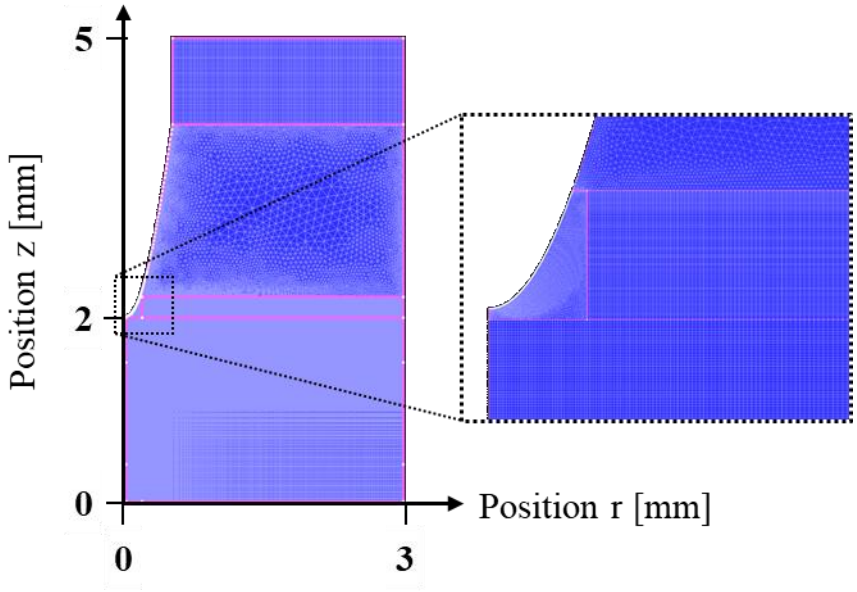

Figure 4.8. Computational mesh used in this research [5]. The computational region is modeled as axisymmetric and a hybrid mesh is used.

4.3.2. Results and discussions

4.3.2.1. Positive polarity for the pin electrode

This section presents simulation results for propagation of primary and secondary streamers and generated plasma properties when a positive polarity voltage is applied to a pin electrode.

Positive primary streamer

When applying a positive high voltage at the pin electrode, the electric potential distribution distorts around the tip of the pin electrode, generating a strong electric field and propagating the streamer discharge along a directed strong field towards the plane electrode. See Refs. [3] and [6] for a detailed description of the mechanisms for the generation and propagation of streamer discharges.

Figure 4.9 shows contour maps for simulated distributions of the reduced electric field and the electron number density. Atmospheric pressure discharge studies generally use the reduced electric field E/N to discuss the electric field. Distributions of other variables, namely, the electric potential and electron temperature, are shown in the appendix. Figures 4.9(a) and (b) show distributions at the start of streamer propagation, before arriving at the plane electrode. A filamentary peak of the reduced electric field can be seen. This peak, called the streamer head or the ionization wave front, increases the electron temperature (mean electron energy). Near the streamer head, highly energetic electron-impact reactions generate electrons, ions, and radicals. The streamer head propagates towards the plane electrode. (See Appendix A1 for the +5 kV condition.) Increased electron number density can be seen behind the streamer-passing region. This region is called the streamer channel and is in a plasma state. At 1.4 ns, the streamer head arrives at the plane electrode. The effective propagation speed between the electrodes is approximately 1.4 mm/ns (1.4×10^6 m/s).

The streamer head expands in size until reaching a position of 1 mm and slightly reduces just when reaching the plane electrode surface. There is insufficient time to propagate at nearly constant size due to the small 2 mm gap, so the streamer head appears expanded and contracted. Note that previous works reported that under longer electrode gap conditions, the streamer head grew in the first propagation stage, became a nearly constant size at the middle of the gap, then reduced in size before arriving at the plane electrode.

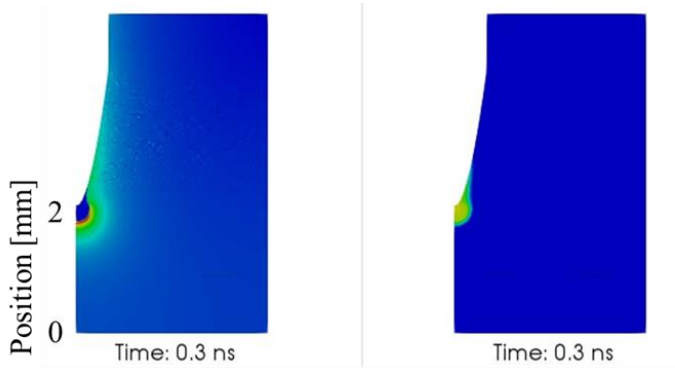

(a) 0.3 ns

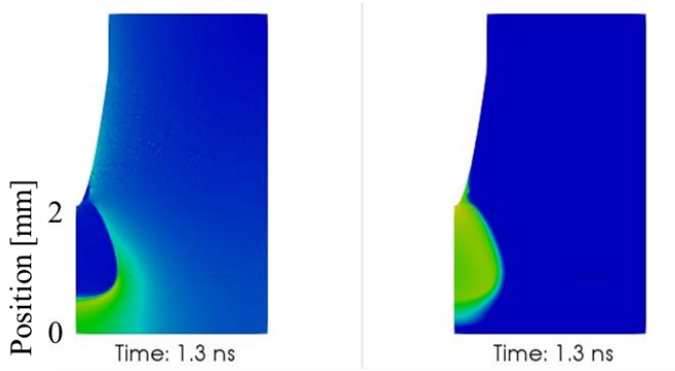

(b) 1.3 ns

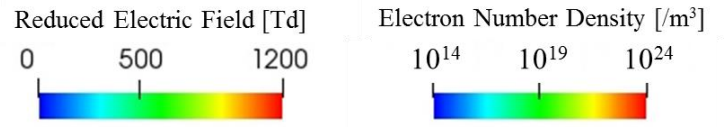

Figure 4.9. Spatiotemporal behavior of a primary streamer in atmospheric pressure argon discharge when positive DC voltage of +10 kV is applied to the pin electrode. Left is the reduced electric field and at right is the electron number density for (a) 0.3 ns and (b) 1.3 ns. A peak in the reduced electric field (streamer head) and a high electron number density region (streamer channel) can be observed.

Figure 4.10 shows temporal distributions of the reduced electric field and the electron number density as functions of position in the interelectrode gap. In Fig. 4.10, interelectrode distances of 2 mm and 0 mm correspond to the pin tip and the plane electrode, respectively, and the primary streamer propagates in a right-to-left direction. The peak of the reduced electric field corresponds to the primary streamer head, reaching a relatively high value of 2000 Td at the initial propagation stage and about 600–800 Td most other times. The relatively high value at the initial stage was induced by the applied constant voltage with no rise time. An increase of the reduced electric field can be observed before arriving at the plane electrode. This tendency agrees with previous works [7, 8], and is induced by approach of the plasma to the plane. The electron number density increases near the peak of the reduced electric field by electron impact reactions caused by high-energy electrons. Under these conditions, electron densities ranging from 10^{20} to 10^{21} m^{-3} are obtained and remain constant along the streamer channel.

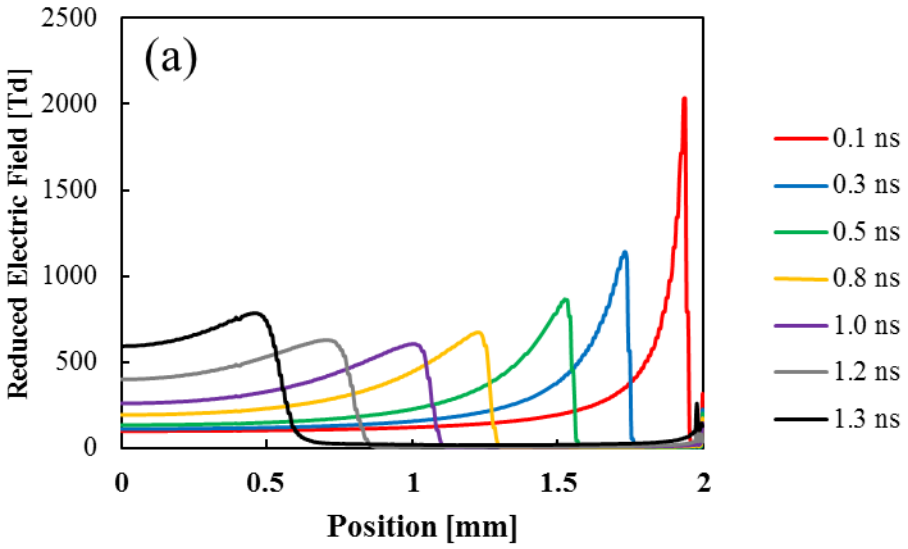

(a) Reduced electric field.

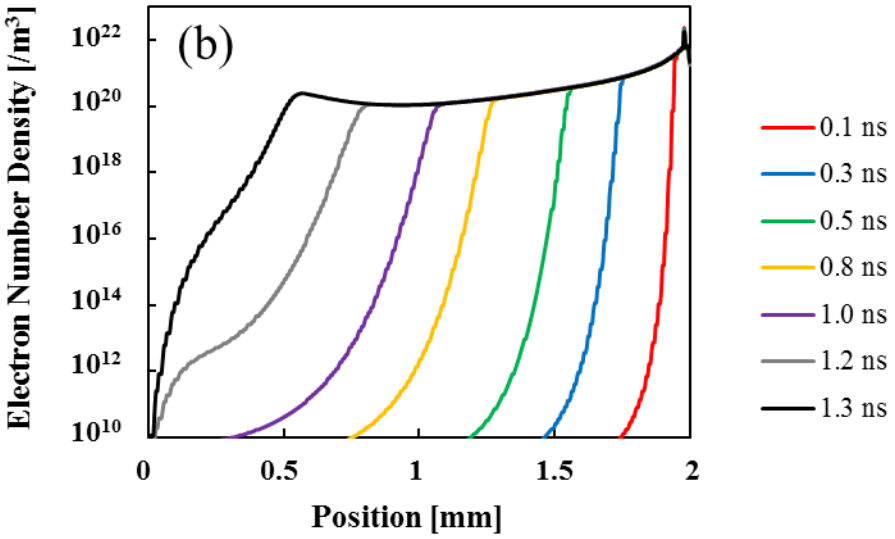

(b) Electron number density.

Figure 4.10. Reduced electric field and electron number density of a primary streamer between electrodes in atmospheric pressure argon discharges when a positive DC voltage of +10 kV is applied. The primary streamer head propagates from right to left.

Positive secondary streamer

In streamer discharge, a high reduced-electric-field region arises from the pin electrode before and after the primary streamer arrives at the plane electrode. This is known as a secondary streamer. As shown in previous studies [3, 4], secondary streamers arise due to redistribution of space charge after a primary streamer arrives at a plane electrode. These studies showed that different species are generated in primary and secondary streamers, so it is equally important to investigate the properties of both. Regarding streamer discharge in air, comparisons between primary and secondary streamers have shown differences in generation efficiency of O, N, and OH radicals, which are thought to be important species for applications [4, 9, 10].

This research focuses on secondary streamers arising at about 1.4 ns, when the primary streamer head arrives at the plane electrode. Figure 4.11 shows spatiotemporal behavior of the electron production rate to discuss the secondary streamer generation. In primary streamer propagation (1.2 ns and 1.3 ns in Fig. 4.11), a filamentary peak of the electron production rate is observed at the streamer head. The primary streamer arrives at the plane electrode at timings ranging from 1.4 ns to 1.5 ns. A region with high electron production rates arises from the pin electrode. This is a secondary streamer, and additional species are produced in this region. A similar high-value region from the plane electrode can also be observed between 1.4 ns and 1.5 ns. This is known as a return stroke, and it disappears relatively quickly.

Note that the numerical simulation diverges after around 0.1 ns when the secondary streamer arises, due to the application of a constant voltage to the pin electrode during the entire simulation period without a rising and falling waveform. Figure 4.11(b) shows the discharge current. The value of approximately 10 A is within double of

experimentally obtained discharge current, although the reliability of the experimental value is not high. The oscillation in the current after 1.5 ns corresponds to the divergence of the simulation. From the perspective of numerical simulation, remarkably strong electric near the plane electrode and high current through the streamer channel made the limitation to the numerical time step small and cause numerical instability for solving the Poisson equation semi-implicitly.

From the perspective of actual situations, the streamer connects a path between the pin and plane electrodes to form a highly conducting channel across the entire gap. This corresponds to observations of arcing (sparking) in previous simulation studies of pin-to-pin geometry [11]. This may represent a complicated mathematical formulation for nonequilibrium plasma phenomena. Such complex transition phenomena, in terms of applied voltage waveforms and heating of neutral gases, are beyond the scope of this research.

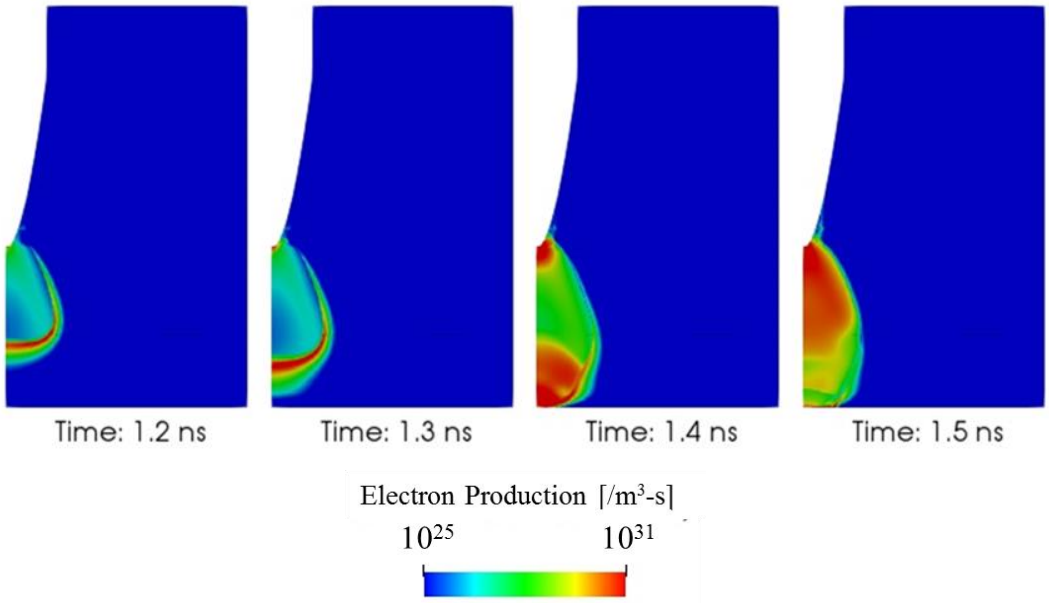

(a) Electron production rate.

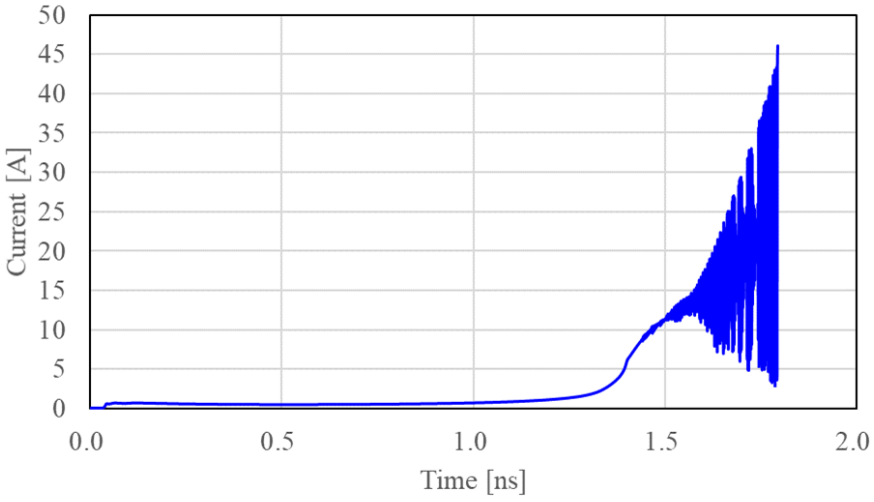

(b) Discharge current.

Figure 4.11. Spatiotemporal behavior of electron production rate and discharge current in atmospheric pressure argon discharge when positive DC voltage of +10 kV is applied to the pin electrode. A region of high electron production arising from the pin electrode shows generation of a secondary streamer. A similar high-value region from the plane

electrode shows a return stroke.

Distribution of species in positive streamers

Figure 4.12 shows obtained plasma properties of species number densities and electron temperatures for primary and secondary streamers in atmospheric pressure argon. The distributions are at about 1 mm (1.0 ns) for primary steamers and after secondary streamer occurrence (1.5 ns) for secondary streamers. In Fig. 4.12(a), increased species number densities in streamer channels and increased electron temperatures at the streamer head are observed in the primary streamer. The increased electron temperature in front of the streamer head is due to a large reduced electric field induced by the small gap. In the primary streamer, dominant species in the streamer channel are Ar^m, E, and Ar^+, followed by Ar_2^+ and Ar_2^m. Note that E and Ar^+ appear to overlap, but Ar_2^+ is less than 1% of Ar^+ and the plasma is electrically neutral. Electron number density in the secondary streamer increases to twice that in the primary streamer (see Fig. 4.12(c)) because the secondary streamer generates additional electrons.

Species composition in the plasma is unchanged between the primary and secondary streamers in atmospheric pressure argon discharge. On the other hand, there is a noticeable difference in electron temperatures between the streamers. In the primary streamer, the electron temperature was about 20,000 K within the streamer channel and about 81,000 K near the primary streamer head. In the secondary streamer, the electron temperature increased to 53,000 K in the streamer channel. This noticeable change suggests that plasma composition in the streamer channel greatly changes between the primary and secondary streamer when molecular or electronegative gases are mixed with argon gas, even if argon is the main component.

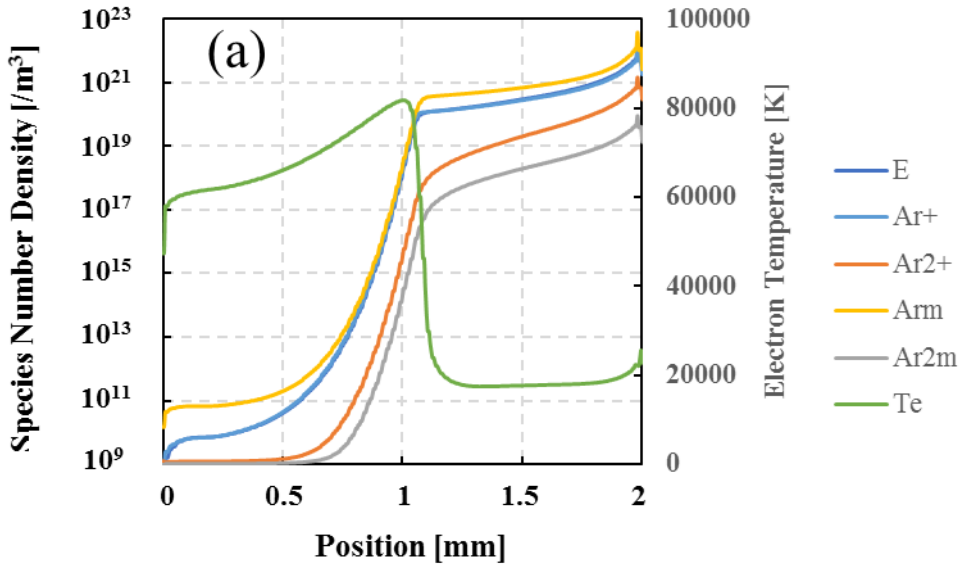

(a) Primary streamer.

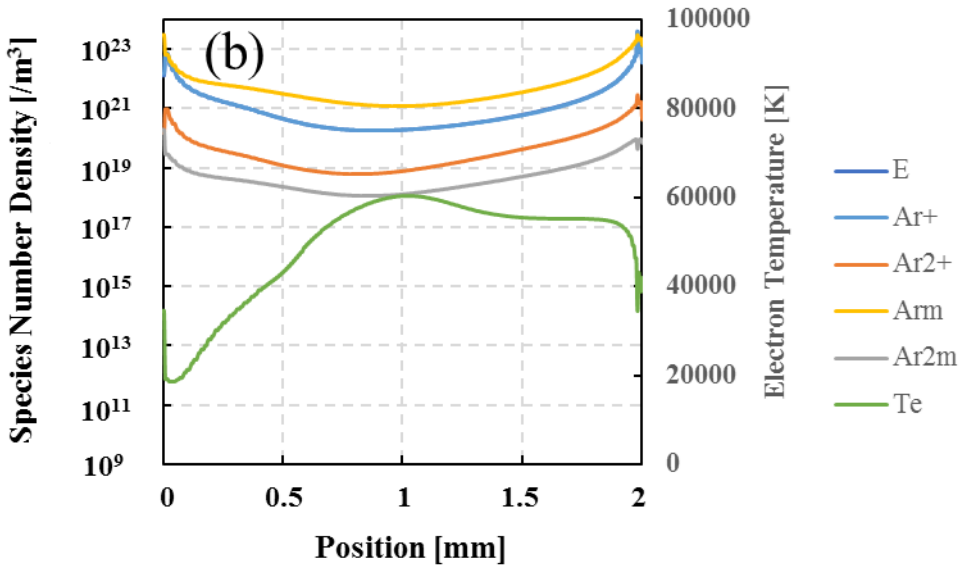

(b) Secondary streamer.

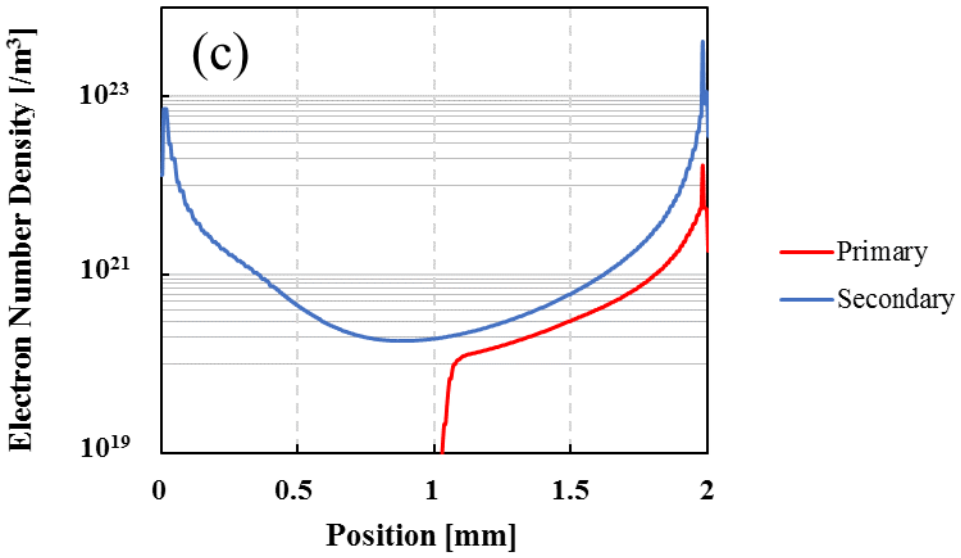

(c) Differences in electron number density between streamers.

Figure 4.12. Simulated species number density and electron temperature as a function of position when a positive DC voltage of +10 kV is applied for (a) primary and (b) secondary streamers, and (c) differences in electron number density between streamers. Plasma species composition is identical between primary and secondary streamers, but electron temperature is noticeably higher in the secondary streamer.

4.3.2.2. Negative polarity for the pin electrode

Polarity of an applied voltage is an important control parameter for realizing required plasma properties. A previous study reported that a streamer head in air at atmospheric pressure diffuses more when applied voltage is negative than when positive. However, there are fewer studies of negative streamers than of positive ones. In particular, regarding streamer discharge in noble gasses like argon at atmospheric pressure, there are few studies of discrepancies in basic discharge types depending on the polarity of applied voltage. Generation efficiency of metastable species leading to a Penning effect may

change. This section presents simulation results for negative voltage applied to the pin electrode. Other settings are identical to the positive voltage case described in the previous section.

Negative primary streamer

Figure 4.13 shows spatiotemporal distributions of the reduced electric field and electron number density when a negative voltage of –10 kV is applied to the pin electrode. (See Appendix A2 for the –5 kV condition.) As in the case where a positive voltage is applied, there is a filamentary peak of the reduced electric field and an increase in electron number density. Unlike the positive streamer, however, in the negative streamer a distorted (sharp) streamer head propagates from the pin to the plane electrode. The negative primary streamer head arrives at the plane electrode at 0.6 ns, and the effective propagation speed between the electrodes is estimated as about 3.3 mm/ns (3.3×10^6 m/s). The distorted shape makes it difficult to evaluate the size of the streamer head, but it appears smaller than that in the positive case.

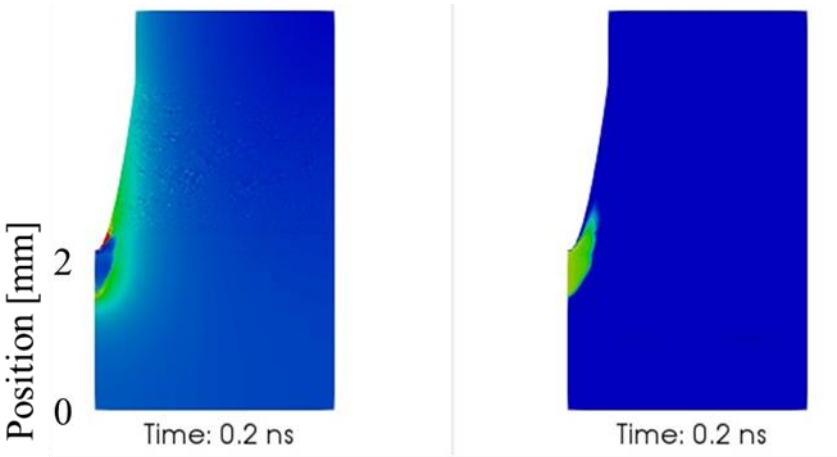

(a) 0.2 ns

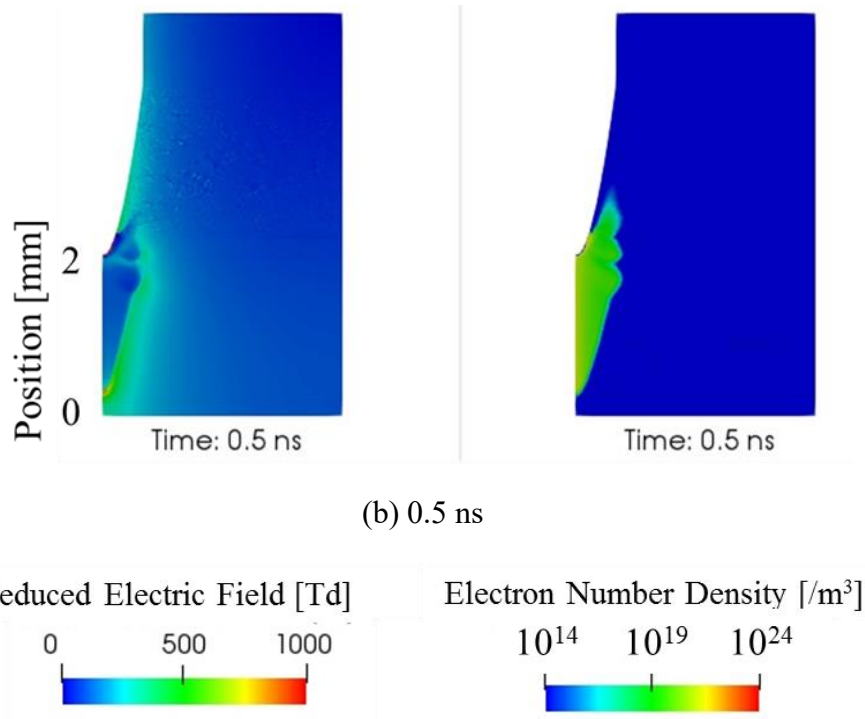

(b) 0.5 ns

Figure 4.13. Spatiotemporal behavior of a primary streamer in the atmospheric pressure argon discharge when a negative DC voltage of –10 kV is applied to the pin electrode. Left is the reduced electric field and at right is the electron number density for (a) 0.2 ns and (b) 0.5 ns. A distorted (sharp) streamer head can be observed unlike the positive streamer.

Figure 4.14 shows several temporal distributions of the reduced electric field and electron number density between the electrodes. The reduced electric field in the negative streamer was a nearly constant value of about 900 Td during propagation. An increase of the reduced electric field is observed before arriving at the plane electrode as for the positive streamer, but this increase is smaller. There is a remarkable peak in the reduced electric field at the streamer head, due to the sharp, small streamer head shape. Electron number density generated by passing of the streamer head is an order of 1.0×10^{21} m^{-3}

and higher than that of the positive streamer (1.0×10^{20} m^{-3}), except near the pin electrode in positive streamer (1.0×10^{21} m^{-3}).

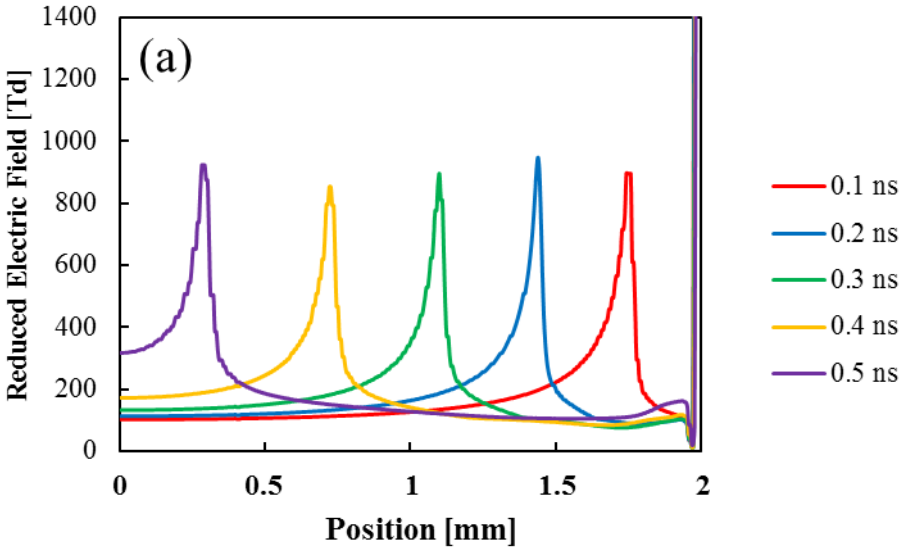

(a) Reduced electric field.

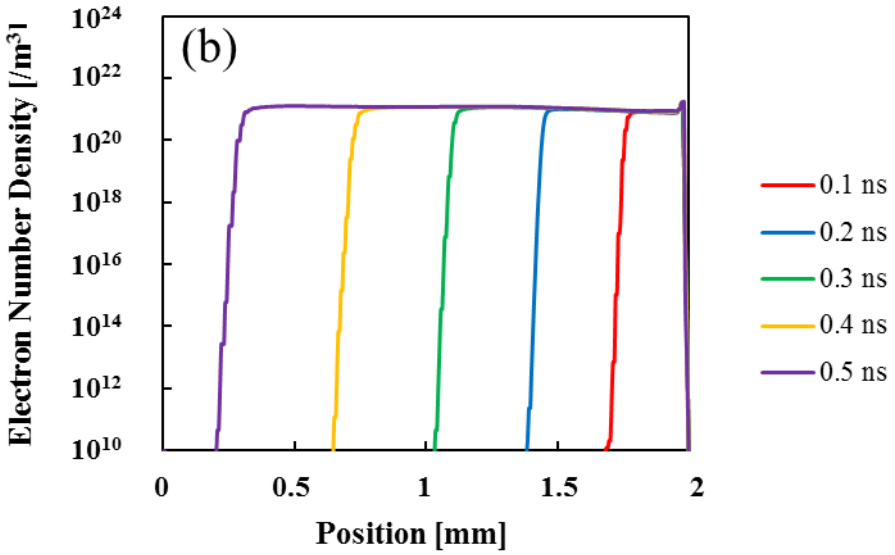

(b) Electron number density.

Figure 4.14. Reduced electric field and electron number density of primary streamers between electrodes in atmospheric pressure argon discharges when negative DC voltage

of −10 kV is applied. The primary streamer head propagates from right to left.

Negative secondary streamer

Figure 4.15 shows spatiotemporal behavior of electron production rates to discuss the generation of secondary streamers when a negative DC voltage of −10 kV is applied. As Fig. 4.15(a) and (b) show, peak electron production rates are observed at the primary streamer head, as in the case of a positive 10 kV streamer, but the shape was different from that shown in Fig. 4.9. At about 0.6 ns (Fig. 4.15(c)), the negative primary streamer arrives at the plane electrode. Unlike the positive streamer, no high-electron-production region from the pin electrode was observed; only a return-stroke-like distribution was observed in negative streamer.

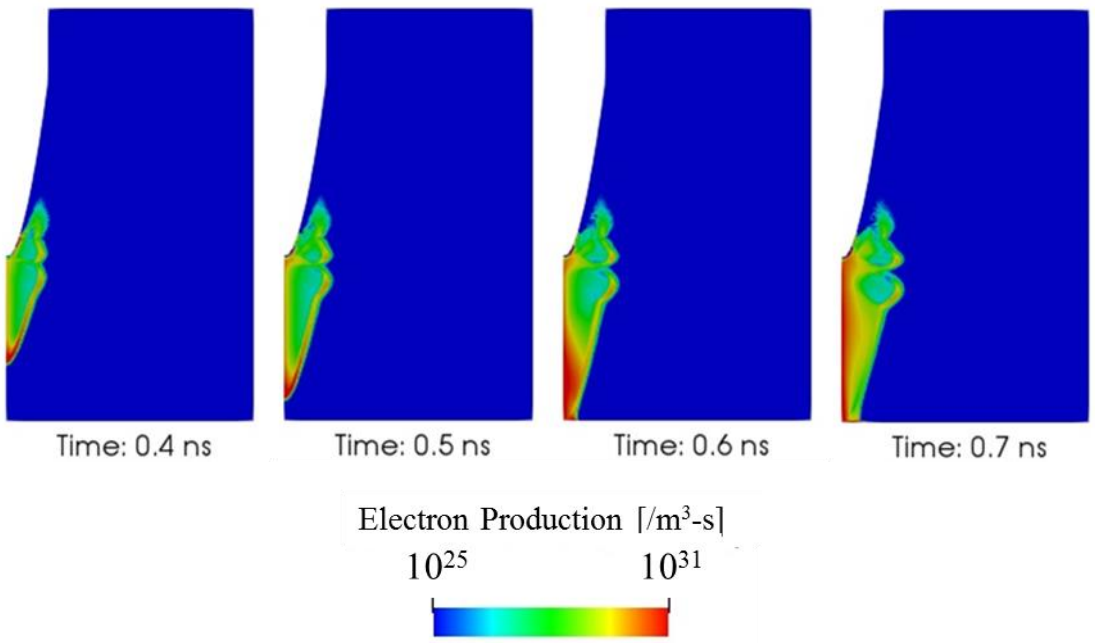

Figure 4.15. Spatiotemporal behavior of electron production rate in atmospheric pressure

argon discharge when a negative DC voltage of –10 kV is applied to the pin electrode. The secondary streamer from the pin electrode is not observed and only return stroke is observed.

Distribution of species in negative streamers

The following describes plasma properties generated by negative streamers. Figure 4.16 shows species number density over time and electron temperatures at a 1 mm position between the electrodes for primary (0.3 ns) and secondary (0.7 ns) streamers when a negative voltage of −10 kV was applied. Dominant species in plasma generated by negative streamers were Ar^m, E, and Ar^+, followed by Ar_2^+ and Ar_2^m. This tendency was identical to the case of positive streamer plasma, but the electron number density increased by ten times. As Fig. 4.16(a) shows, this increase in electron number density corresponds to the increased electron temperature (mean energy) to 200,000 K due to the larger reduced electric field at the negative primary streamer head. Further, the sharper streamer head than that for a positive streamer makes the peak in the reduced electric field remarkable and local. Electron temperatures in the negative streamer channel are about 35,000–50,000 K, compared with about 20,000 K in the positive streamer channel.

In the negative secondary streamer (Fig. 4.16(b)), there is a small difference in species number density as compared to the primary one, but the electron temperature increased to 50,000 K. Figure 4.16(c) shows the discrepancy between the primary and secondary streamer. Near the pin electrode, increase in the electron number density is small due to nonexistence of the secondary streamer, but a larger increase is observed near the plane electrode because of the return stroke, as Fig. 4.15 shows.

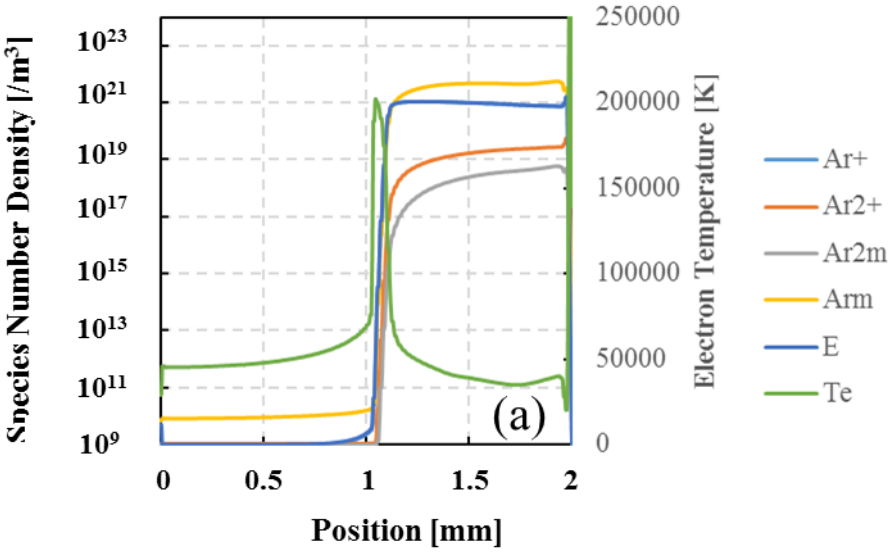

(a) Primary streamer

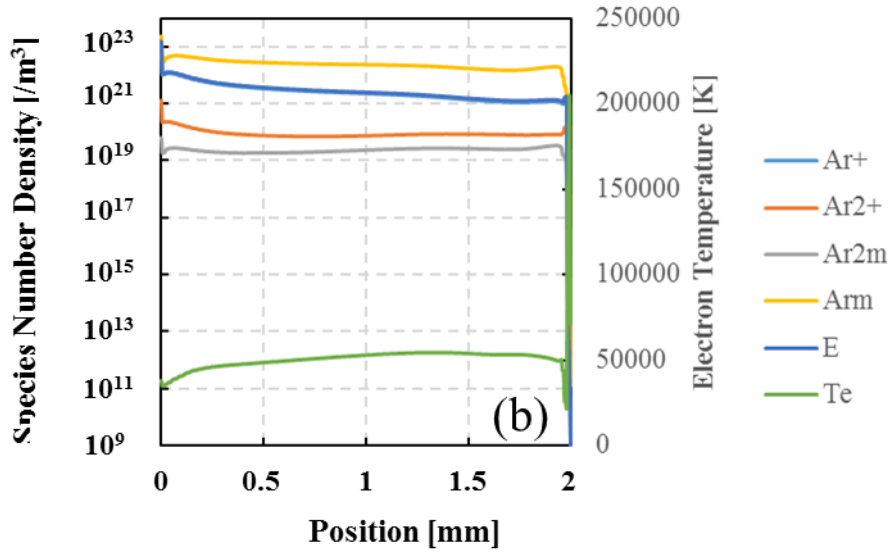

(b) Secondary streamer

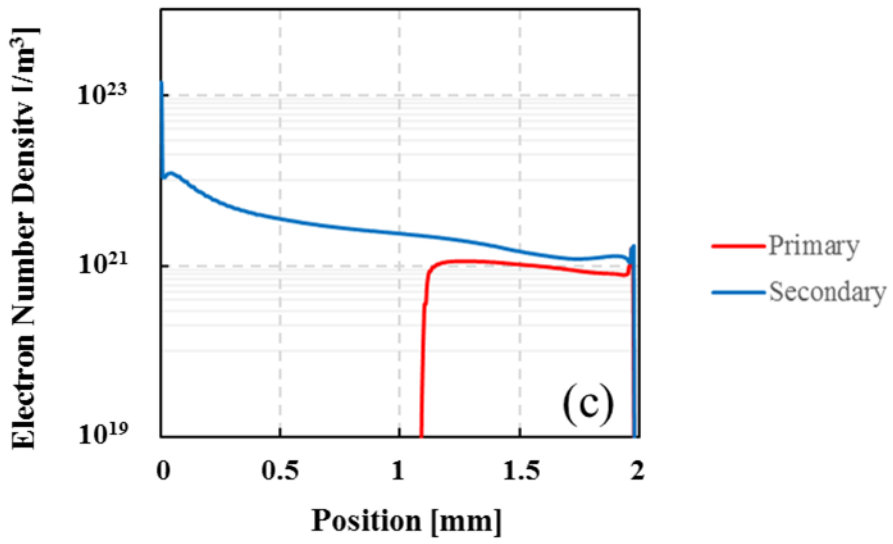

(c) Differences in electron number density between streamers

Figure 4.16. Simulated species number density and electron temperature as a function of position in (a) primary and (b) secondary streamers and (c) difference in electron number density between the streamers when −10 kV is applied.

4.3.2.3. Discussion

Relations among applied voltage, streamer head size, and propagation speed in positive streamers

Figure 4.17 shows simulated properties of the positive streamer head. The size (diameter) of the streamer head was estimated from the radial peak position of the reduced electric field when the primary streamer head passed at a position of about 1 mm. Propagation speed was estimated from the time the streamer head arrived at the plane electrode considering a 2 mm gap. As Fig. 11(a) and (b) show, the diameter and propagation speed of the streamer head increase with applied voltage, while saturation is

observed about the diameter at the high-voltage region. To discuss and demonstrate validity of the obtained results, Fig. 4.17(c) shows the relation between size and propagation speed in the positive primary streamer head. Propagation speed and diameter are nearly proportional when the diameter is relatively small, and propagation speed greatly increases when the diameter becomes relatively large.

Naidis discussed the relation between streamer velocity and diameter, analytically obtaining a relation between the reduced electric field, streamer propagation speed, and streamer head diameter [2]. He showed that propagation speed is basically proportional to diameter and deviates at high-speed regions, and many experimental results support this tendency. Naidis also showed the existence of a minimum sub-millimeter size for positive streamers. As Fig. 4.17(c) shows, our results too suggest a minimum size of about 0.1 mm, corresponding to zero streamer velocity. This qualitatively supports the validity of our model and results.

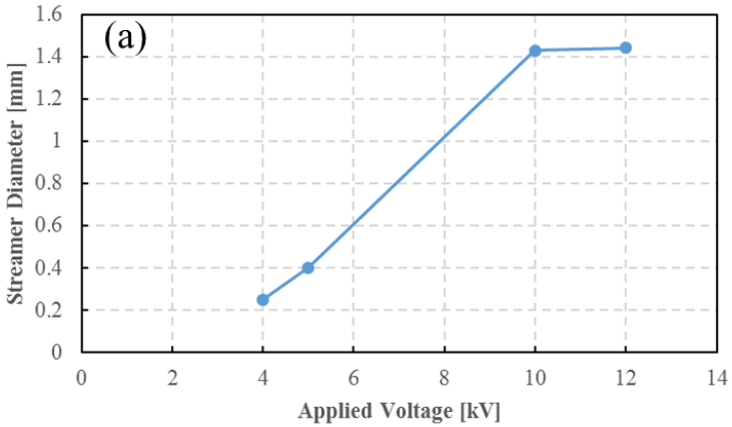

(a) Streamer head diameter.

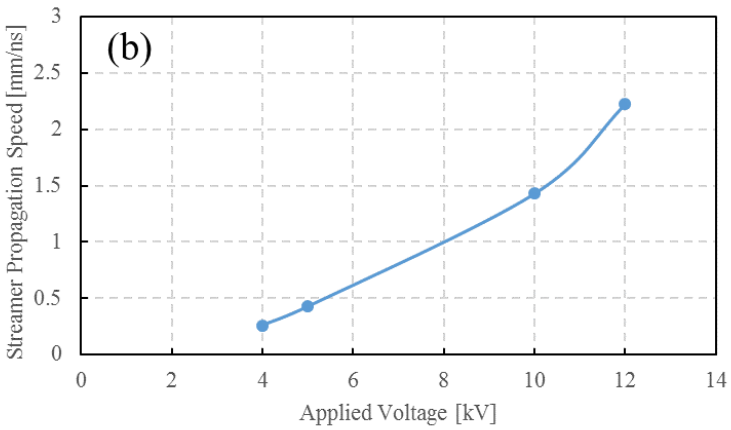

(b) Propagation speed.

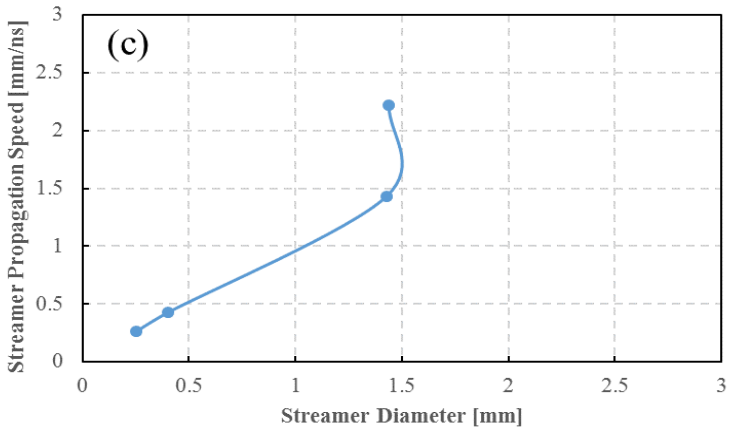

(c) Relation of size and propagation speed.

Figure 4.17. (a) Size and (b) propagation speed of a primary streamer head as functions of positive voltage applied to the pin electrode. (c) Relation of size and propagation speed of a primary streamer head when positive voltage is applied to the pin electrode.

Dependence of electron number density on applied voltage in positive streamers

Figure 4.18 shows electron number density in a streamer channel when passing a position of 1 mm as a function of applied voltage. With increasing applied voltage, a decrease in electron number density was observed to 10 kV, then an increase at 12 kV.

This tendency is somewhat surprising because we expected the increased size and propagation speed of the streamer head to show a stronger discharge. This decrease in electron number density is likely due to insufficient time to induce chemical reactions at the streamer head, due to acceleration of the propagation speed at high voltage. Similarly, a previous work showed that increased time of applied voltage affects the speed of streamer propagation, decreasing electron generation [12]. From the perspective of chemical species delivery to the plane surface, a low-voltage operation of 5 kV can supply Ar^m, E, and Ar^+ of 10^{22} m^{-3} over a 0.4 mm diameter, and of 10^{20} m^{-3} over a 1.4 mm diameter in high-voltage operations of 10 kV.

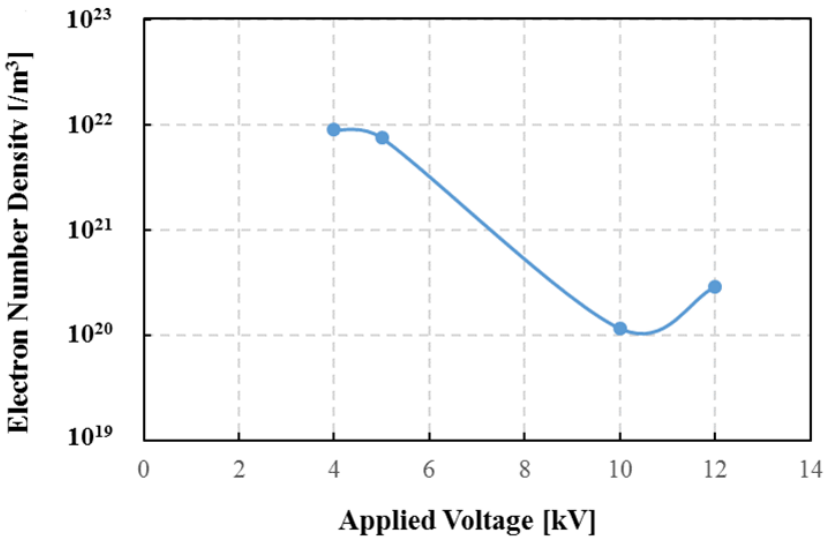

Figure 4.18. Dependency of electron number density generated by streamer discharge on the applied voltage.

Change of discharge mode in negative streamers

As Figs. 4.13 and A2.1 show, we observed a remarkable change in discharge

mode between high and low voltages when the voltage polarity was negative. Under high-voltage conditions, a negative streamer with a diffusive shape propagated among the electrodes. This tendency qualitatively agrees with previous studies in air with negative applied voltage [13, 14]. This diffusiveness is likely induced by differences in the direction of electron movement between positive and negative voltages. In positive streamers, electrons gather toward the pin electrode and central axis. On the other hand, electrons spread away from the pin electrode and central axis in negative streamers. This spread leads to a diffuse shape of the negative streamer and to a corona-like discharge, with lower electron number densities observed under low-voltage conditions.

Comparison with streamers in air plasma

The following compares argon and air streamers when positive voltage is applied. One remarkable difference from air streamers is a lower decrease of electron number density in streamer channels. As Fig. 4.10 shows, electron number density is unchanged between times under propagation. This is due to the low rate of electron loss reactions in argon and noble gas discharges, because electron attachment reactions to form negative ions do not exist. A previous study [15] similarly showed that electron number density does not decrease behind the streamer head in streamer discharge generated within an atmospheric pressure helium plasma jet. Another study of differences between N_2 and O_2 streamer discharge showed that a decreased electron number density is observed in an O_2 streamer channel and that the decrease is negligible for N_2 [16]. Therefore, a small decrease of electron number density in a streamer channel can be considered as a feature of discharges in electropositive gases. The very short propagation time of 1.4 ns may

emphasize this tendency in our conditions.

Regarding the reduced electric field at the streamer head, values are of the same order of magnitude between argon and air streamers. This may be because deviation in space charge is mainly due to fast-moving electrons and mass differences among ions are very small, as compared to mass differences between electrons and ions.

As shown in previous studies [10, 11], dominant species are unchanged between primary and secondary streamers in argon discharge, but differ in air discharges. In atmospheric pressure argon streamers, electron generation is mainly due to electron impact reactions, which increase with increasing electron temperature. Therefore, increased electron temperature in an argon secondary streamer simply increases electron number density in the streamer channel.

Polarity-dependent streamer phenomena

When the positive voltage is applied to the pin electrode, a primary streamer propagates toward the plane electrode, followed by a secondary streamer from the pin electrode when the primary streamer arrives at the plane electrode. The streamer head diameter correlates with propagation speed. Both the streamer head size and the propagation speed increase with voltage applied to the pin electrodes, reaching 1.4 mm and 1.5 mm/ns at 10 kV. On the other hand, the electron number density at the primary streamer head decreases with increased applied voltage, due to acceleration of the propagation speed reducing chemical reactions. Additional electrons are generated by propagation of the secondary streamer. The electron number density is twice that of the primary streamer in the 10-kV case.

When negative voltage is applied to the pin electrode, different discharge types are observed at high and low voltages. With high negative voltage, the primary streamer propagates to the plane electrode, as with positive voltage, but the shape is more diffuse and propagation speed is faster, with no observed secondary streamer. At low negative voltage, the discharge seemed to be a corona type rather than a streamer, and low-density plasma is generated around the pin electrode. Dominant species generated by discharges are Ar^m, E, and Ar^+, followed by Ar_2^+ and Ar_2^m. This tendency was unchanged with polarity of the applied voltage and with differences in the first and secondary streamers.

Candidate choice of voltage polarity for low-voltage operations

Appropriate plasma properties depend on the application and objects to be exposed to the plasma. Generally, safety and electric source costs call for low-voltage operations that maintain a high plasma density. A positive voltage may be appropriate for argon atmospheric pressure discharge, to avoid unintended changes in discharge type observed under negative voltage. Simulations in this research were conducted under ideal, nonperturbed conditions, while actual situations will include uncertain factors such as disturbances in background temperature or flow, mechanical vibrations, and voltage fluctuations of electric sources. Further, generation of a secondary streamer is preferable to increase plasma density.

From the perspective of low-voltage operations, therefore, positive polarity of voltage applied to the pin electrode is appropriate, because it provides relatively high-density plasma, stable streamer propagation, and secondary streamer generation. Simulation-based studies are also useful for developing atmospheric pressure plasma

applications.

4.4 Conclusion

This chapter provided results and discussions about streamer discharge phenomena in air and argon at the atmospheric pressure, utilizing experimental measurements and plasma numerical simulations. The constructed experimental setup produced streamer discharge in air and argon and four distinct regions were observed in air as a previous study.

First, in a streamer discharge, propagations of primary and secondary streamers in air were visualized under a pin-to-plane electrode geometry with the streak imaging. The propagation speed of the primary streamer was estimated as 0.2×10^6 m/s (0.2 mm/ns), this speed is on the same order as or a bit slower than previous experiments. No streak images were obtained about argon streamer discharges due to problems such as a discharge stability and a synchronization of shooting timing, and problems such as deviation and branching that the streamer discharge itself has. In order to analyze streamer discharges in more detail, improvements of the circuit and measurement system are required.

Numerical simulations were conducted to get a more detailed analysis of spatiotemporal behaviors of streamer discharges that occur on the order of nanoseconds. Streamer propagation in atmospheric pressure argon streamer discharges was investigated using a self-consistent, multi-species, multi-temperature plasma fluid model. A parametric study was conducted using positive and negative polarity applied voltage under a pin-to-plane geometry with a gap of 2 mm. The results suggested the following. First, a positive primary streamer propagated in plasma with high electron density, then

the secondary streamer further increased the plasma density, generating an abundance of metastable species. The relation between the streamer head diameter and propagation speed was obtained, for instance, 1.4 mm and 1.5 mm/ns at 10 kV. Second, a negative streamer diffusely propagates in the inter-electrode gap under high-voltage conditions. A corona-type discharge was observed at low negative voltage. Since the generated species maintained both positive and negative polarities, a stable high density of 10^{20} to 10^{22} m^{-3} under a positive low-voltage application has advantages for developing argon-based atmospheric pressure plasma applications.

It was confirmed that experimental and numerical analyses can complement each other and lead to a deeper discussion than either alone, although there is room for improvements in both methods in this study. Moreover, the effectiveness of modeling using a simple chemistry argon model was also confirmed for analysis of streamer discharge phenomena.

References

1. R. Ono, Y. Nakagawa, and T. Oda, J. Phys. D: Appl. Phys. **44** 485201 (2011).
2. G. V. Naidis, Phys. Rev. E. **79** 057401 (2009).
3. O. Eichwald, O. Ducasse, D. Dubois, A. Abahazem, N. Merbahi, M. Benhenni and M. Yousfi, J. Phys. D: Appl. Phys. **41** 234002 (2008).
4. A. Komuro, R. Ono and T. Oda, J. Phys. D: Appl. Phys. **45** 265201 (2012).
5. Y. Sato, K. Ishikawa, T. Tsutsumi, A. Ui, M. Akita, S. Oka, and M. Hori, J. Phys. D: Appl. Phys. **53**, 265204 (2020).
6. L. B. Loeb and J. M. Meek, J. Appl. Phys.**11** 438–47 (1940).
7. N. Y. Babaeva and M. J. Kushner, J. Phys. D: Appl. Phys. **43** 185206 (2010).

8. A. Komuro, Ph.D. thesis (The University of Tokyo) (2013).
9. R. Ono, K. Takezawa and T. Oda, J. Appl. Phys. **106** 043302 (2009).
10. A. Komuro, K. Takahashi and A. Ando, J. Phys. D: Appl. Phys. **48** 215203 (2015).
11. R. Scarcelli, T. Wallner, S. Som, S. Biswas, I. Ekoto, D. Breden, A. Karpatne and L. L. Raja, Plasma Sources Sci. Technol. **27** 12 (2018).
12. A. Komuro, R. Ono and T. Oda, Plasma Sources Sci. Technol. **22** 045002 (2013).
13. D. Saito, W. Hayakawa, A. Komuro, and R. Ono, Jour. Inst. Electrostat. Jpn, **39** 5 204-209 (in Japanese) (2015).
14. Y Xian, X Lu1, J Liu, S Wu, D Liu and Y Pan Plasma Sources Sci. Technol. **21** 3 (2012).
15. G V Naidis, J. Phys. D: Appl. Phys. **43** 402001 (2010).
16. Z. Kanzari, M. Yousfi, and A. Hamani, J. Appl. Phys. **84** 4161 (1998).

Chapter 5 Study on coaxial dielectric barrier discharge

5.1 Introduction

DBD is a typical method for generating LTAPP, and is classified into planar, plasma jet, and reactor types. This chapter describes experimental and numerical analyses of coaxial reactor-type DBD plasma, focusing on discharge properties and the plasma generation process inside the device.

From previous studies, discharges in the reactor-type DBD have reached a consensus of glow-like in pure helium and filament-like in the pure argon [1]. Helium discharge is likely to be suitable for gas decomposition processes in the reactor type DBD because wider plasma region would be realized than that of the argon discharge. Therefore, numerical analyses were conducted under the pure helium condition in this research.

On the other hand, in recent years, it has rapidly become difficult to obtain helium, which makes it difficult to use helium for large-scale experiments. Therefore, experiments were conducted under argon conditions. Although the author also tried additional simulations under argon conditions, the two-dimensional axisymmetric simulations did not stabilize probably due to three-dimensional structures and steep gradients that the argon discharge have in the reactor type DBD. As the result, experiments were conducted with argon whereas the numerical simulations were conducted with helium, though knowledge about argon plasma and about differences between argon and helium discharges are important.

5.2 Analysis by experiments

Figure 5.1 shows the OES setup in this study. Emission spectra are measured using a spectroscope. The 2 mm distance between the spectroscope and plasma (emission

part) was set considering emission intensity. The DBD device comprises a quartz glass tube and two copper cylindrical electrodes. The electrode gap is 30 mm. Voltage of 15 kV and 60 Hz is applied to the upper electrode, and the lower electrode is floating. The flow rate of argon gas through the dielectric tube is 1-3 slm (standard liters per minute). Experiments use argon gas, because helium gas has become difficult to obtain.

Figure 5.2 shows a photograph of argon DBD plasma generated by the coaxial DBD device. The depicted filament-like emissions continually move around in the dielectric tube.

Figure 5.3 shows the OES spectrum for argon DBD plasma. There are more than 10 peaks, almost all of which are assigned as argon-related peaks. For example, the peak at 750.4 nm is due to light emission from transition of Ar $1s_2$-$2p_1$ [1].

Discharge types in coaxial DBD devices have been studied mainly in the context of plasma jet devices [2-5]. The filament-like discharge type in this study agrees with a previous study reporting that argon DBD tends to become filament-like, while helium DBD tends to become the glow type [2, 3]. This study uses numerical simulation to perform more detailed analyses of DBD plasma in the DBD device.

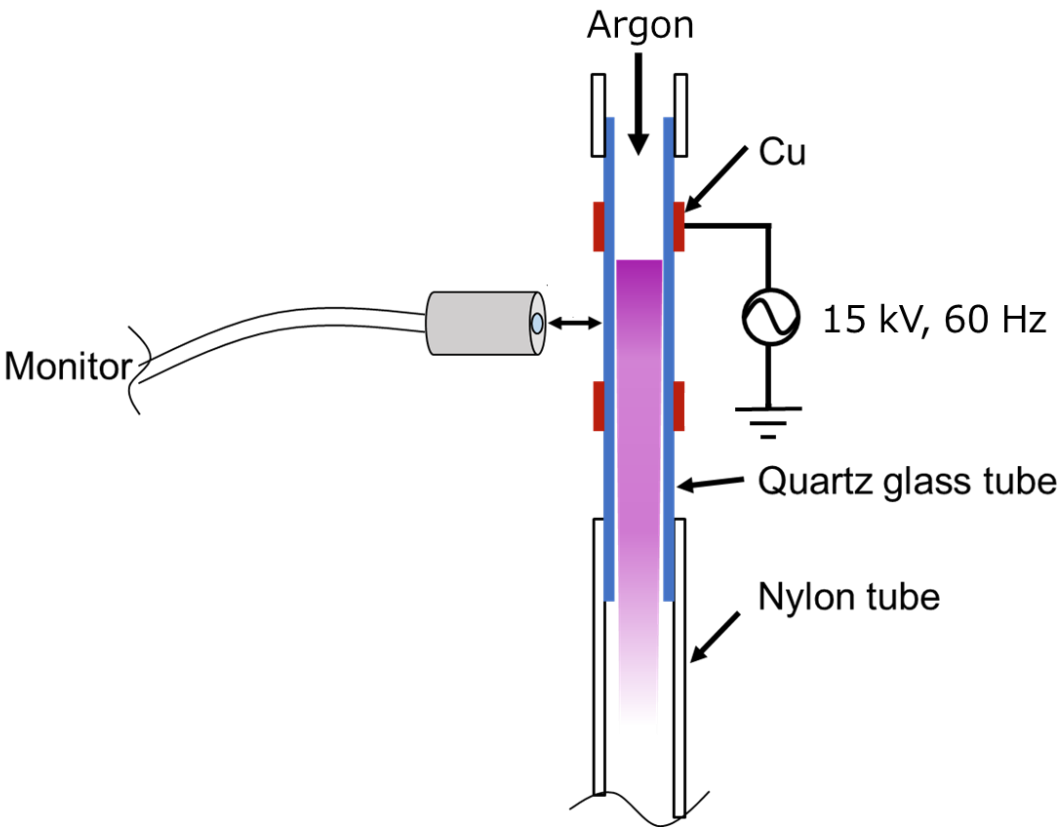

Figure 5.1: Schematic of the OES experimental setup.

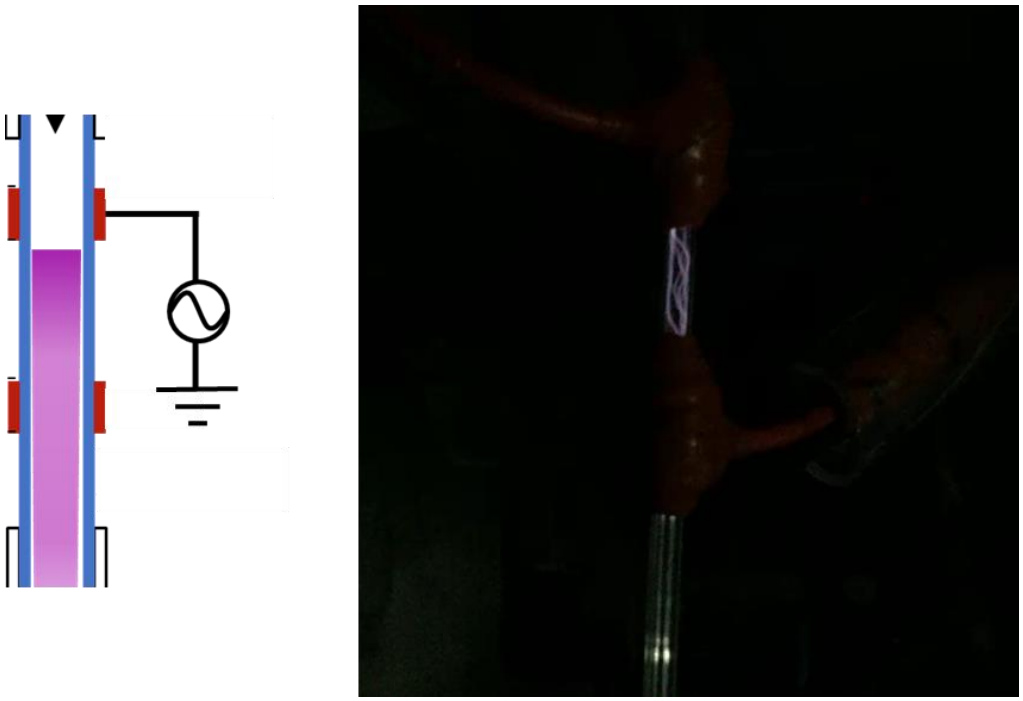

Figure 5.2: Photograph of argon DBD plasma. Filament-like discharge was observed between the electrodes.

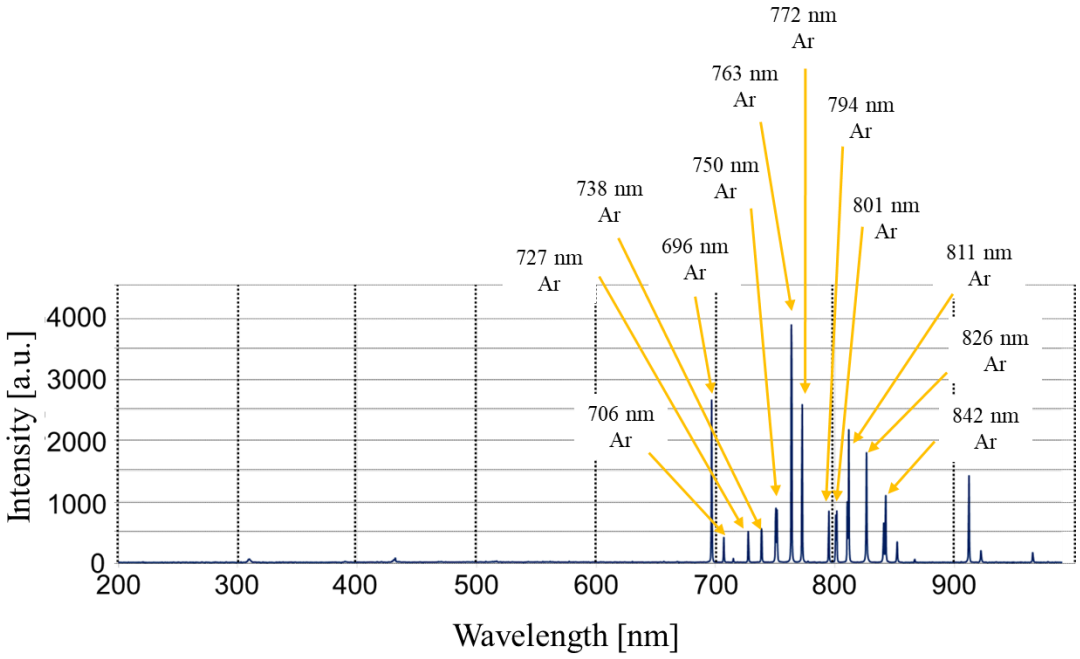

Figure 5.3: OES spectrum and its assignment for the argon DBD plasma. The gas flow rate is 3 slm.

5.3 Analysis by numerical simulations

This section describes attempts to clarify the detailed plasma formation process in a coaxial reactor-type DBD at nanosecond to microsecond timescales, using fluid-based plasma numerical analysis. This section also discusses a parametric study of control parameters for the coaxial DBD and relations between plasma density and distribution.

Analyses described in this section were conducted with helium plasma, whose discharge type in DBD is known to be the gentle glow type. Although knowledge of argon plasma and of differences between argon and helium is important, argon discharge seems to have three-dimensional structures, so modeling it would be quite difficult and computationally expensive. Analysis with helium is also useful, because discharge properties in the DBD device have not yet been elucidated, due to difficulties of

measurement resulting from electrodes and dielectrics preventing observations within the device.

5.3.1. Computational model

5.3.1.1. Plasma fluid model and helium chemistry model

In order to analyze spatiotemporal behavior in the coaxial DBD device, a self-consistent, multi-species, multi-temperature plasma model is used. The model is basically common with Chapter 3 and Chapter 4 (streamer discharge), while the helium chemical reaction model is considered.

Considering pure helium plasma, we modeled six species: electrons (E), helium ions (He^+), helium dimer ions (He_2^+), helium composite metastable species (He^m), helium dimer metastable species (He_2^m), and ground-state helium atoms (He). Table 5.1 shows the plasma chemistry model. Reaction pathways for the pure helium reaction mechanism and reaction rate coefficients for non-electron impact reactions are from a previous work [7]. Rate coefficients for electron impact reactions, denoted as EEDF, are calculated using BOLSIG+, an offline zero-dimensional Boltzmann solver [8] based on cross-sectional data from the literature. For surface reaction mechanisms, all excited and charged species are assumed to be quenched with an attachment coefficient of unity.

As mentioned above, photoionization in discharges accompanied by streamers (bullets) has been noted as determining the streamer propagation speed, but is not essential for propagation itself [8,9]. Moreover, in the analyses of argon streamer discharge with no photoionization model in Section 4 and Ref. [10], the propagation speed of argon streamers agreed with a number of experimental results to within an order of

magnitude (mm/ns). Therefore, this simulation does not assume any photoionization processes. The numerical method is also commonly used for streamer analysis.

Table 5.1. Helium plasma chemistry model

Rxn	Reactions	Reaction rate coefficient [a]	Ref.
G_1	$E + He \rightarrow E + He^m$	$2.308\times10^{-10}\ T_e^{0.31}\ \exp(-2.297\times10^5/T_e)$	[7, 8]
G_2	$E + He \rightarrow 2E + He^+$	$2.584\times10^{-12}\ T_e^{0.68}\ \exp(-2.854\times10^5/T_e)$	[7, 8]
G_3	$E + He^m \rightarrow 2E + He^+$	$4.661\times10^{-10}\ T_e^{0.6}\ \exp(-5.546\times10^4/T_e)$	[7, 8]
G_4	$E + He^m \rightarrow E + He$	$1.099\times10^{-11}Te^{0.31}$	[7, 8]
G_5	$E + He_2^m \rightarrow 2E + He_2^+$	$1.268\times10^{-12}\ T_e^{0.71}\ \exp(-3.945\times10^4/T_e)$	[7, 8]
G_9	$E + He_2^+ \rightarrow He + He^m$	$5.386\times10^{-7}Te^{-0.5}$	[7, 8]
G_{10}	$2He^m \rightarrow E + He + He^+$	2.7×10^{-10}	[7]
G_{13}	$He^m + 2He \rightarrow He_2^m + He$	1.3×10^{-33}	[7]
G_{14}	$He^+ + 2He \rightarrow He_2^+ + He$	1.0×10^{-31}	[7]

[a] Units of cm^3/s for two bodies and cm^6/s for three bodies reactions.

5.3.1.2. Device configuration and parameters

Figure 5.4 shows the reactor-type DBD device used in this study. In the base configuration, pure helium flows through a dielectric tube with 4 mm inner diameter, 0.8 mm thickness, and 100 mm length. For ease of viewing, the *z*-direction is displayed at 1/5 scale. Two copper electrodes are placed around the dielectric tube, with voltage applied to the upper electrode and the lower electrode grounded. Target parameters are applied voltage, electrode gap, inner tube diameter, and thickness and dielectric constant of the dielectric tube. Table 5.2 shows the conditions of all parameters.

Figure 5.4 also shows the computational mesh. The space resolution is uniformly 100 μm in the radial and axial directions, constructed by structured meshes. This mesh

size is larger than in simulations of streamer discharge (where the minimum size is 1 μm). Investigations of effects of mesh resolution on plasma distributions have confirmed that any such effects are small. This resolution has been confirmed as sufficient for qualitatively analyzing the generation process of plasma under our conditions. On the other hand, simulations for argon discharges did not stabilize even with 1 μm resolution mesh under conditions of this section.

Figure 5.5 shows the computational region and the boundary conditions. Simulations are conducted in a two-dimensional axisymmetric geometry. The computational region includes the dielectric tube and the gas inside the tube, modeled as a half region from the center axis. These conditions were set because the experimental results in the previous section and a previous study of a similar coaxial configuration [12] showed that discharge emission between the electrodes is limited.

Note the similarities and differences between our setting and those for a plasma jet. In the plasma-jet case, a plasma bullet or ionization wavefront shoots out from the dielectric tube, inducing electron impact reactions even outside of the tube. The computational region for a plasma jet therefore extends outside of the tube [18, 19]. Generally, the distance between the electrode and nozzle exit in a plasma jet is closer (at most 2 cm) than in our target device. Additionally, some plasma jet devices assume environmental air as a virtual electrode (virtual ground) [9, 13]. Considering these differences, we include no region outside the tube when setting boundary conditions at the nozzle exit. Testing different tube lengths to confirm any effects due to this boundary condition, we found no significant effects on the plasma distribution. As shown below, streamer propagation is driven by the local electric field due to local charge density

induced by the plasma itself. The electric field beyond the electrodes is sufficiently weak that it does not contribute to plasma generation.

5.3.1.3. Operation of applied voltage

Commercial power (frequency 50 or 60 Hz) is assumed for the applied voltage and modeled as constant voltage in the simulations. The following discusses this modeling in more detail. Figure 5.4 shows schematic of the applied voltage and discharge currents in the reactor type DBD. The time period at 50 Hz is 0.02 s (20 ms). However, the numerical time step must be about 1×10^{-12} s (1 ps) to analyze the behavior of electrostatic potential and electrons. This time step requires more than 1×10^{9} iterations per cycle calculation. This is a very high computational cost, so modeling is needed to analyze the discharge.

To overcome this difficulty and acquire insights into the generation process and plasma distribution, we focus on experimental facts. Typical DBD device operation frequencies are in the kHz range [20]. Previous studies have reported discharge current waveforms from 1 kHz to about 100 kHz [16]. In these results, discharge pulses occur at most several times per voltage cycle, with durations of at most several microseconds.

In the 50 Hz sinewave case, for example, 2 μs is 1% of the period. Under this pulse duration, variation of the applied voltage amplitude is less than several tens of volts, which is less than 1% that of the 10 kV (10,000 V) case. Under 50 Hz conditions, therefore, modeling a constant voltage waveform under each discharge pulse is valid, so long as the change in voltage over the duration is sufficiently small with respect to the amplitude.

Based on the above modeling of the applied voltage, this research focuses on the beginning phase of single discharge pulse. This model neglects charge accumulation on

the dielectric surface prior to the discharge pulse which could affect the discharge properties under AC voltage waveform and the electron heating prior to the discharge. However, the simulation of a single discharge pulse provides information on the complicated dynamics of mode transitions during a discharge.

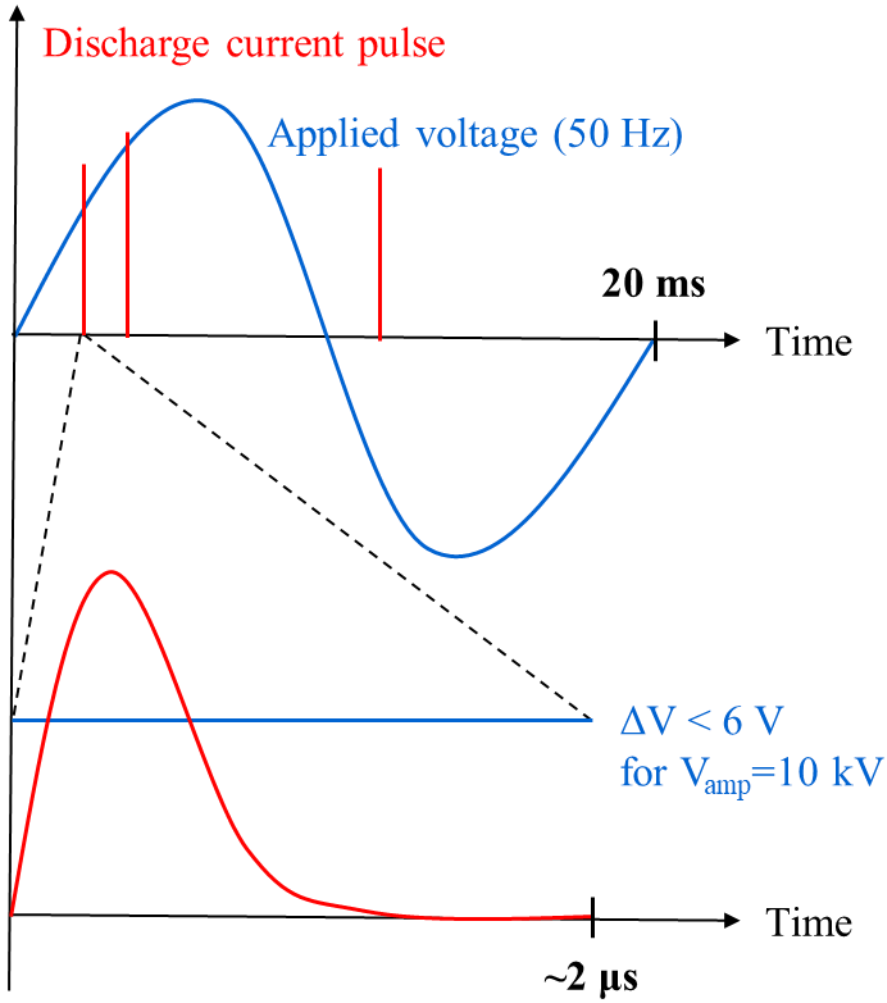

Figure 5.4. Schematic of the applied voltage and discharge currents in the reactor type DBD device.

5.3.1.4. Effects of gas flow

Simulations in this study do not consider gas flow, because of the highly disparate timescales of plasma discharge phenomena and fluid flow under typical conditions of several slm gas-flow rate in a reactor-type DBD. To model propagation of bullets outside the tube, the mole fractions of helium and air outside the tube are estimated as the background concentration [8, 9]. Even in plasma-jet cases, momentum transfer between plasma and background gases is usually not considered. In addition, Li et al. reported that the electron number density in argon plasma does not greatly change in a coaxial DBD device [21].

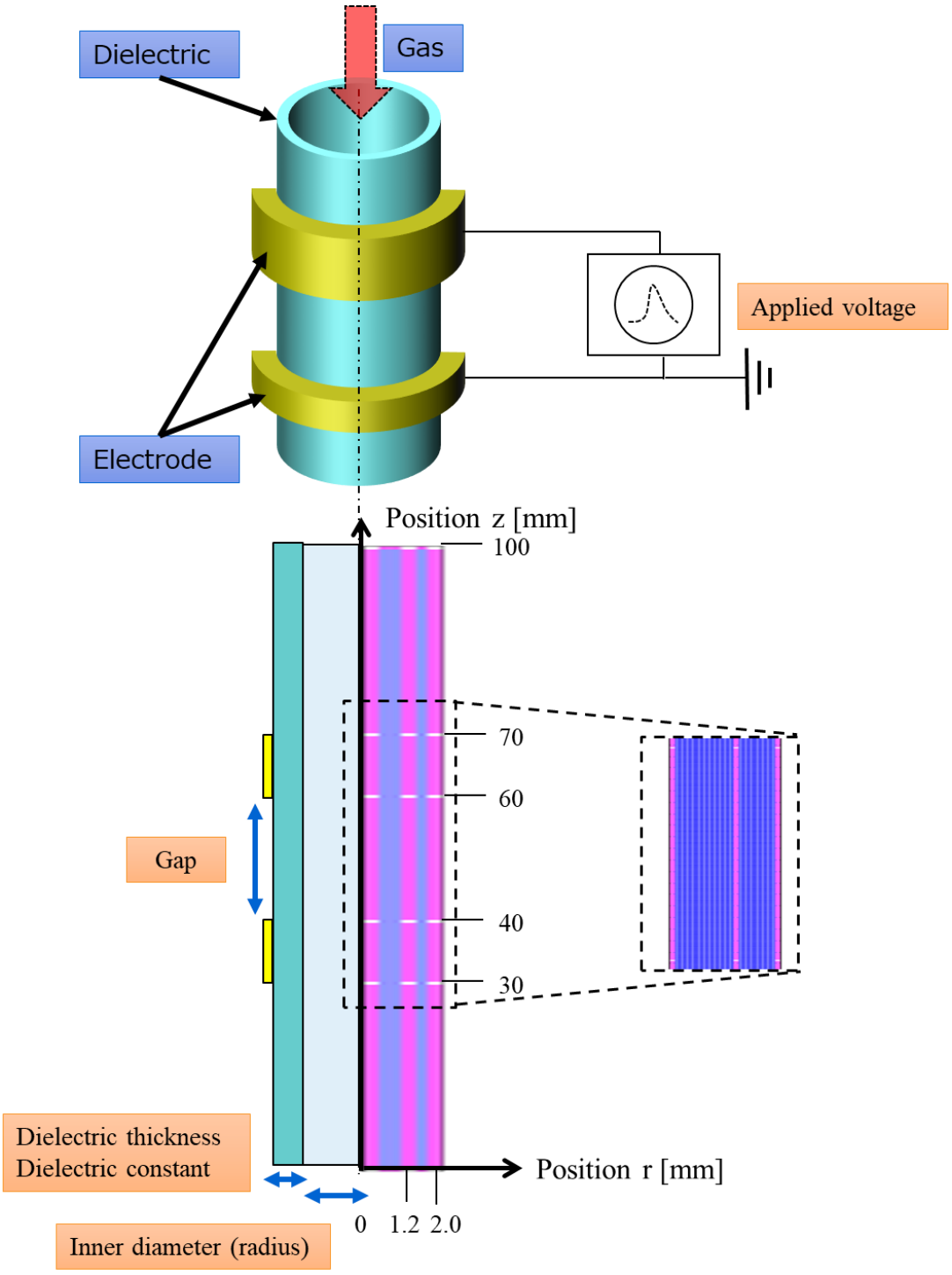

Figure 5.4. Base configuration, computational mesh and parameters.

Table 5.2. Conditions.

Voltage	Gap	Dielectric thickness	Dielectric constant	Inner diameter
10 kV	10 mm	0.5 mm	5	2.4 mm
15 kV	20 mm	0.8 mm	10	4 mm
20 kV	30 mm	2 mm	15	6 mm

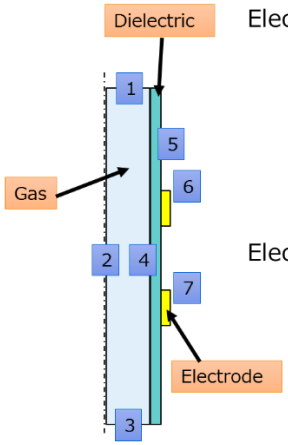

Electric potential
1 symmetry
2 axis
3 symmetry
4 continuous (surface charge)
5 symmetry
6 fixed potential (parameter)
7 fixed potential (0 V)

Species continuity
1 symmetry
2 axis
3 symmetry
4 solid surface flux
5 -
6 -
7 -

Electron temperature
1 symmetry
2 axis
3 symmetry
4 solid surface flux
5 -
6 -
7 -

Heavy species temperate
1 symmetry
2 axis
3 symmetry
4 fixed temperature (300 K)
5 fixed temperature (300 K)
6 fixed temperature (300 K)
7 fixed temperature (300 K)

Figure 5.5. Computational region and boundary conditions.

5.3.2. Spatio-temporal behavior

5.3.2.1. Three stages of plasma development

Figure 5.6 shows a contour map of the reduced electric field and the electron number density in the gas region at characteristic times of 130, 180, and 270 ns after application of high voltage (15 kV) to the electrodes. For ease of viewing, the *z*-direction is displayed at 1/5 scale. Helium plasma clearly develops in three stages in the coaxial DBD device. Detailed descriptions of each stage are presented below.

First, at 130 ns after the high-voltage application, an electric field of approximately 30 Td is induced between the electrodes, and an increase in the electron number density to the order of $10^{17}/m^3$ is observed. This discharge mode is of the Townsend-glow type. The electron density and the electron temperature T_e are nearly uniform between the electrodes. T_e is a nearly constant 40,000 K.

The second stage comes at 180 ns after the high-voltage application, where the electron number density increases to the order of $10^{18}/m^3$. A large electric field appears at an edge of the lower electrode to which the high voltage is applied. This region, called the wavefront, forms at the edge of the plasma region, where the electron number density reaches up to $1\times10^{18}/m^3$ at 150 ns. In this second stage, the electric field wavefront expands to the plasma region. This leads to the streamer discharge or plasma bullet propagating axially, and the electron number density increases to $1\times10^{19}/m^3$ at 180 ns.

In the third stage, the discharge mode transits to a surface discharge that propagates along the dielectric surface. As this surface discharge develops, the electron number density increases to the order of $10^{20}/m^3$ at 270 ns after the high-voltage application. Propagation ceases when the plasma spreads beyond the region of the electrodes. Before transition to surface discharge, charge on the dielectric surface

accumulates with a density of approximately 9×10^{-4} C/m^2. This accumulation develops a reduced electric field of approximately 350 Td, which induces electron heating. The electron number density near the dielectric increases to 1×10^{20}/m^3, while that between the electrodes is lower, on the order of 1×10^{16}/m^3.

At 2000 ns, electron number densities at the center between the electrodes, near the dielectric surface, and at a position slightly away from the electrodes are about 1×10^{19}/m^3, 2×10^{19}/m^3, and 1×10^{14}/m^3, respectively. The plasma density distribution is sustained over a period exceeding 10 μs after 270 ns in the three stages.

Figure 5.7 shows temporal behaviors of electron number densities and electron temperatures at the center between the electrodes and near the dielectric surface above the lower electrode. Temporal behavior of the bulk plasma indicates continuous development of plasma density during the first and second stages. In contrast, temporal behavior of the surface plasma shows a sudden increase in density at the third stage.

Increased electron number density by glow-type (first stage) plasma is observed at the center region between the electrodes. When the electron number density reaches about 1×10^{18}/m^3 (150 ns), the slope of the electron number density becomes relatively gentle. This corresponds to the second stage, where the discharge transitions to the axially propagating streamer (bullet) mode. As the discharge passes, the electron number density further increases to 1×10^{19}/m^3. The electron temperature decreases at the center between the electrodes in the second stage, because this position is behind the streamer head and the electric field decreases. After that, a gradual change is observed between the electrodes.

Figure 5.7 shows no increase in electron density near the dielectric surface between the first and second stages. In the third stage, the discharge mode further changes

to a surface discharge that propagates near the dielectric surface. This surface discharge increases in electron number density near the dielectric surface as it propagates.

Regarding overall distribution in the DBD device, unlike in a plasma jet, no bullets shoot from the tube; rather, bullets form between the glow-like and surface discharges and travel a short distance (less than 6 mm). This agrees with previous studies [12, 13] and our above-described experiments. A combination of the ground electrode and the charge accumulation induces a strong electric field of about 350 Td, the dielectric surface promotes the transition to surface discharge, and the distribution spreads slightly beyond the electrodes. The relatively large distance between the electrodes and the exit is also important.

In the above analysis, the applied voltage was set 15 kV. Although the timing (voltage value) at which the discharge actually occurs under AC in the DBD is unknown, this voltage value may be overvoltage with respect to the voltage at which discharge actually occurs. Regarding this point, as shown in later, even under the conditions of 10 kV and 20 kV, the basic state of time evolution was unchanged. Therefore, except for the effects of residual chemical species and surface charge accumulation on the dielectric surface due to repeated discharge, it is presumed that the qualitative plasma formation process is the same as the above result regardless of the magnitude of the voltage value.

Moreover, it is mentioned that the possibility of different views on the plasma formation process. In the above analysis, the second stage was defined as bullet type discharge since the propagating ionization front is usually called plasma bullet in similar device configuration. On the other hand, the three-stage discharge may be considered to be the formation process of the glow discharge. According to this view point, the first stage is the initial stage of the glow discharge and the plasma sheath has not formed yet.

The electric field wavefront at the second stage is regarded as the plasma sheath. Through the third stage, the formation of the plasma sheath proceeds further, and finally the plasma sheath is formed on the dielectric surface.

The previous studies have measured electron and O-atom densities emitted from DBD devices under similar conditions (60 Hz, atmospheric pressure, and 2-5 slm) in plasma-jet experiments [14], finding that the electron number density is about 1×10^{20}-$1\times10^{21}/m^3$ and O-atom density is 1×10^{19}-$1\times10^{20}/m^3$. These measurements of average electron number density occurred after sufficient discharge by continuously applying alternating voltage. In contrast, the simulation results in this study focus on single discharge pulses and do not consider increases in electron number density by multiple discharges. Therefore, the relatively low electron number densities in our simulations seem to be reasonable.

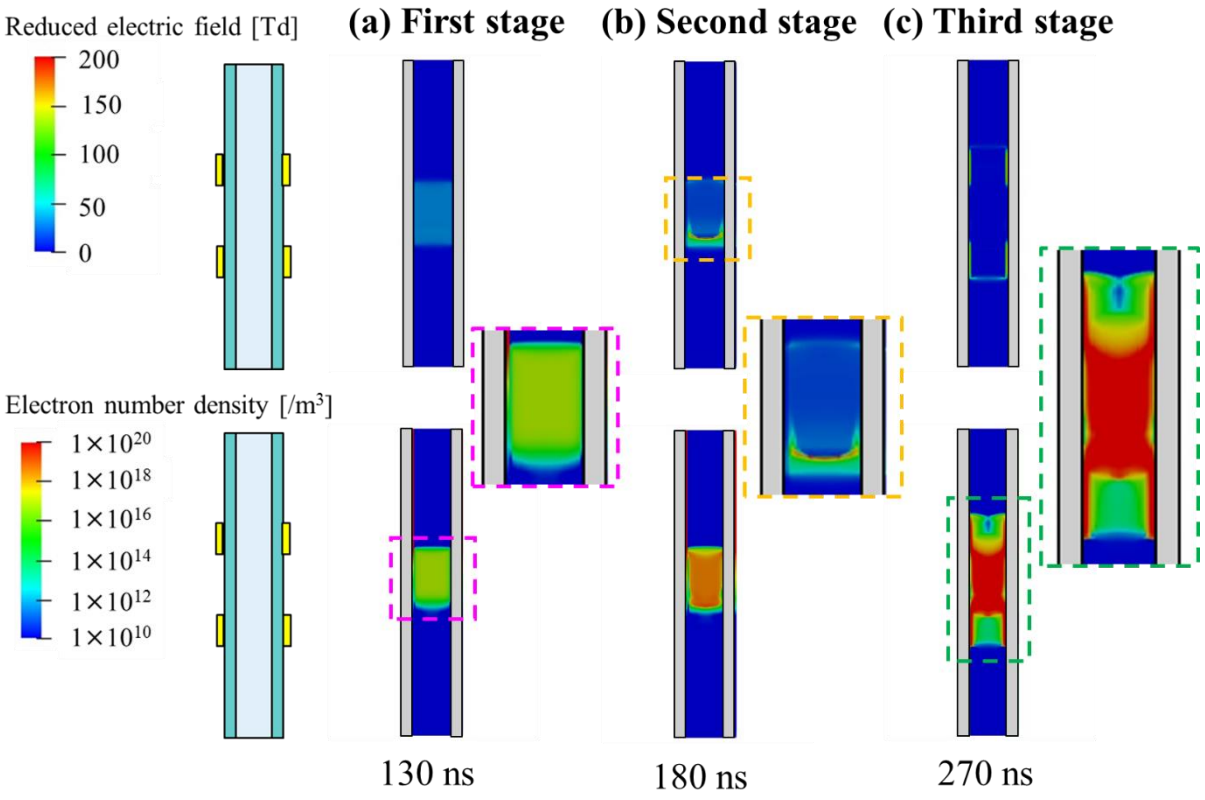

Figure 5.6. Three stages of plasma electron generation [11].

a)

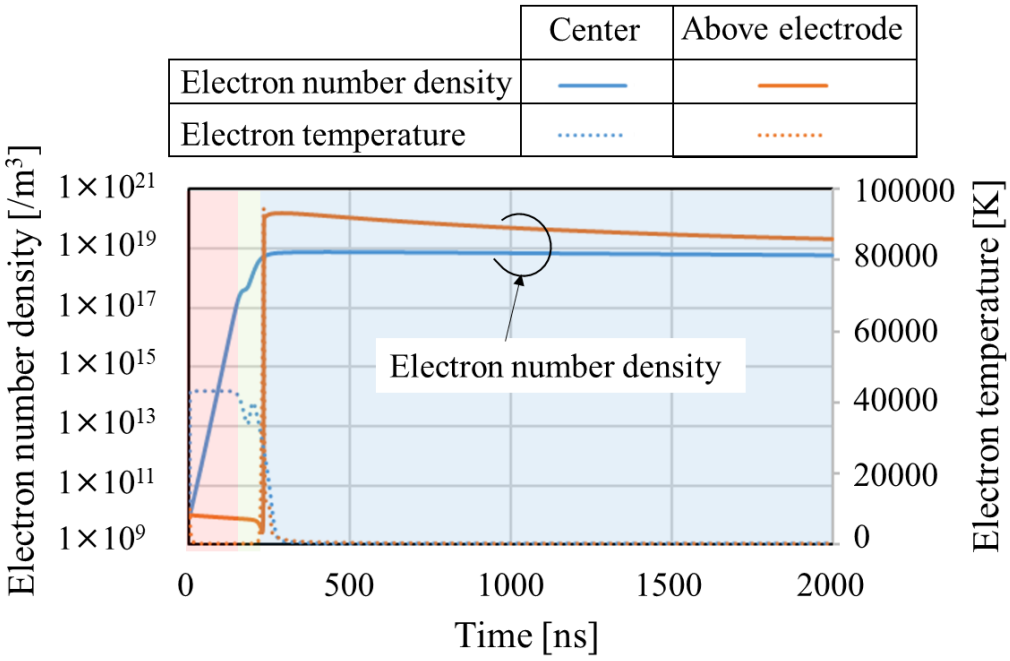
Center
Above electrode
Electron number density
Electron temperature
Electron number density [/m3]
1×10^21
1×10^19
1×10^17
1×10^15
1×10^13
1×10^11
1×10^9
100000
80000
60000
40000
20000
0
Electron temperature [K]
Electron number density
0
500
1000
1500
2000
Time [ns]

b)

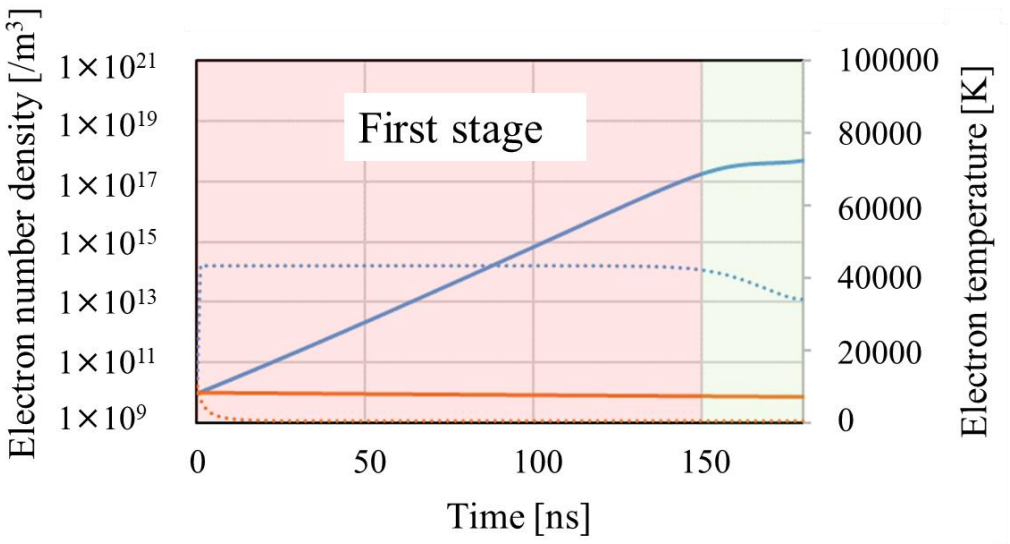
Electron number density [/m3]
1×10^21
1×10^19
1×10^17
1×10^15
1×10^13
1×10^11
1×10^9
First stage
100000
80000
60000
40000
20000
0
Electron temperature [K]
0
50
100
150
Time [ns]

c)

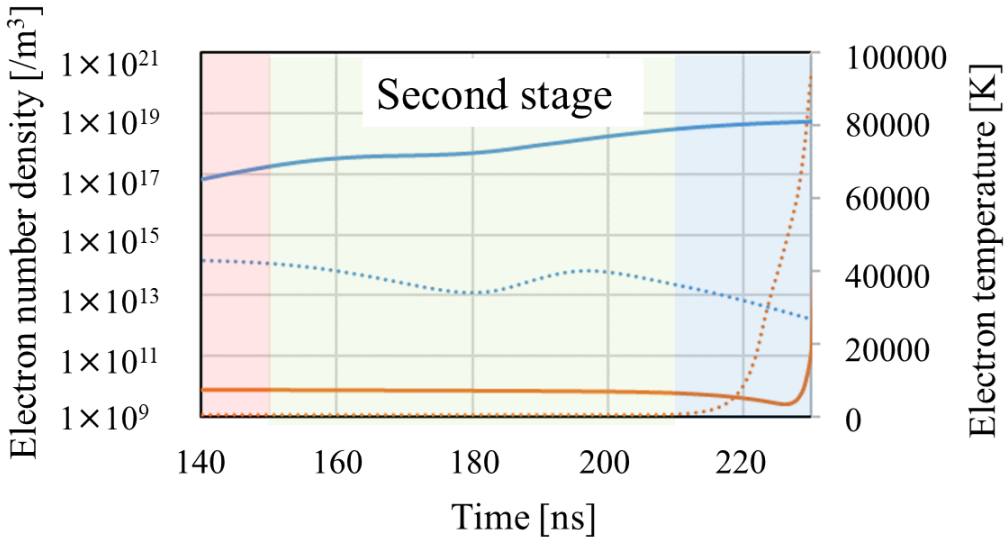

d)

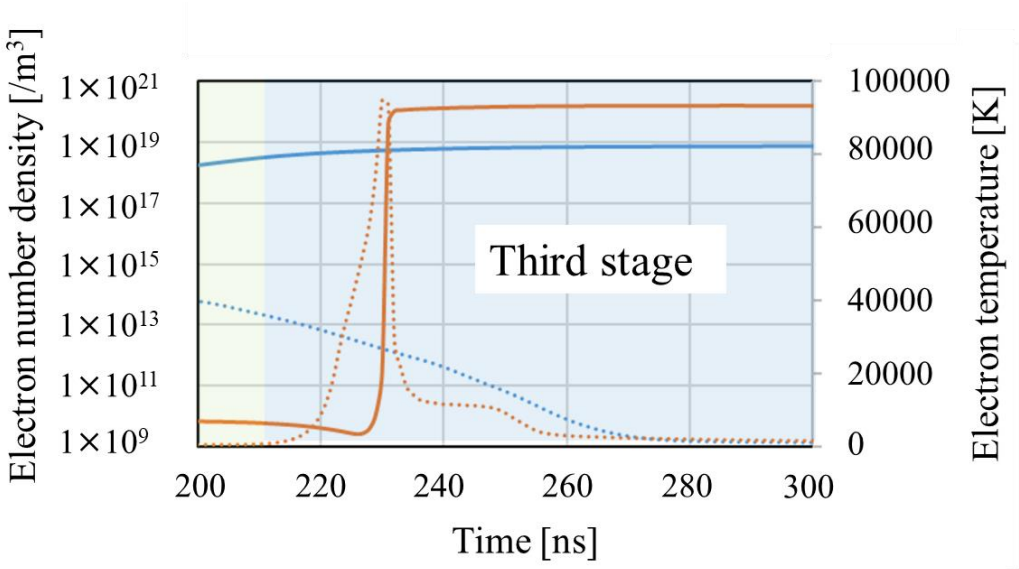

Fig. 5.7. Time history of electron number density (solid lines) and electron temperature (dashed lines) at (a) long time scales (all stages) and in the (b) first, (c) second, and (d) third stages. Blue represents values at the center between the electrodes, and orange represents values near the dielectric surface on the lower (grounded) electrode [11].

5.3.2.2. Details of each stage

5.3.2.2.1 First stage: glow type discharge between electrodes (0 ns – 150 ns)

Applying voltage induces a strong electric field between the electrodes, electron acceleration (heating) increases the electron temperature, and electron impact reactions generate chemically reactive species. Figure 5.8 shows contour maps for simulated distributions of the reduced electric field and the electron number density at 0, 50, 100, 130, and 150 ns in the first stage (0-150 ns). The distribution is nearly uniform and the discharge seems to be of the glow type. The electron number density increases with time. A high-density region begins to form in the plasma from 130 ns. The distribution of plasma density becomes relatively nonuniform. The electron number density reaches about $1\times10^{17}/m^3$ at 150 ns.

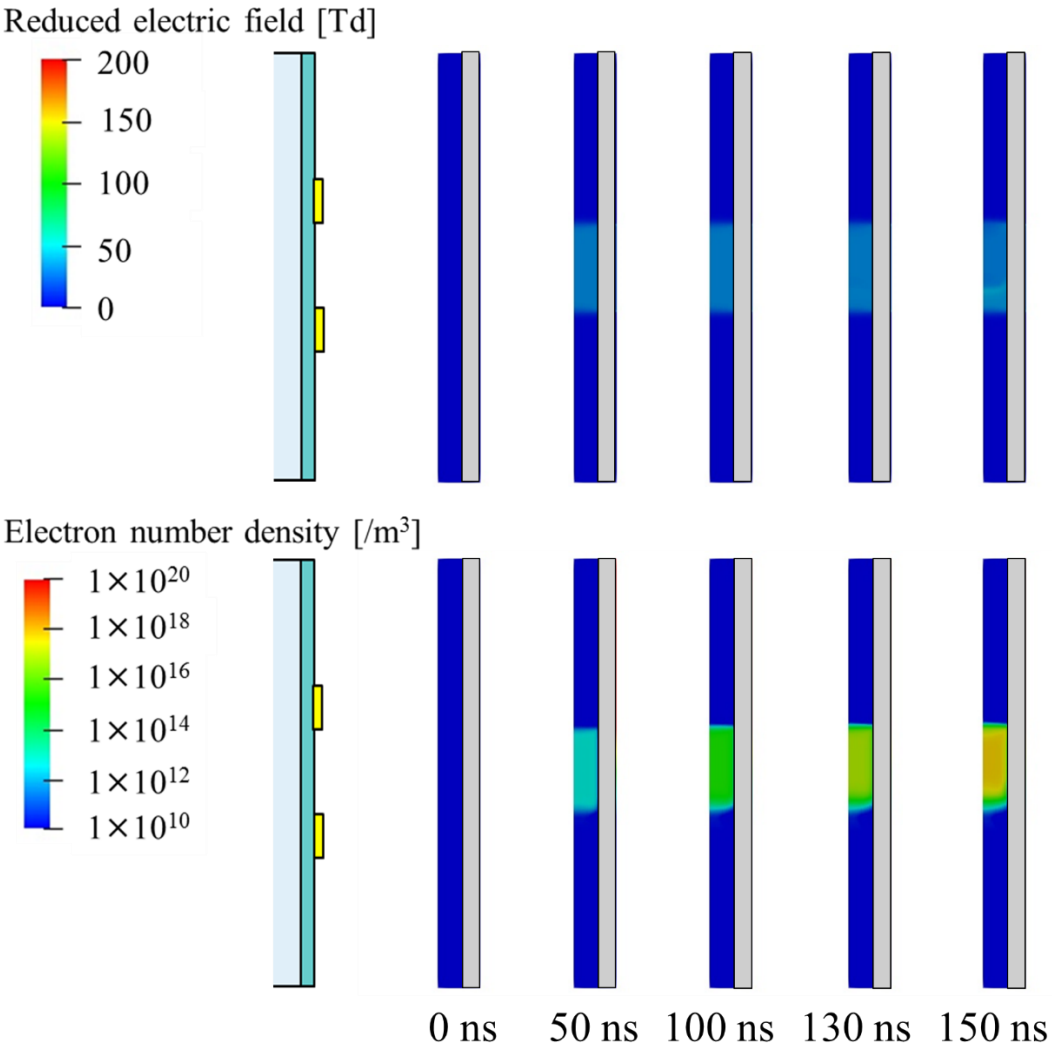

Figure 5.8. Spatiotemporal behaviors at the first stage (Townsend-glow-type discharge). The upper row shows the reduced electric field and the lower row shows electron number density.

5.3.2.2.2 Second stage: development of streamer type discharge (150 ns – 210 ns)

Figure 5.9 shows contour maps for simulated distributions of the reduced electric field and the electron number density. The electron number density in the high-density region reaches near $1\times10^{18}/m^3$ at 160 ns. A high-electric-field region (electric-field wavefront) forms at the lower edge of the high-density region. This high-electric-field region corresponds to the ionization wavefront or streamer head, which is driven by a local electric field induced by a local space charge from the density difference between positive and negative charged particles. This wavefront, also called a plasma bullet in a plasma-jet device, propagates axially along the dielectric surface. As it passes through the dielectric tube, the high-density region enlarges. The electron number density reaches $1\times10^{19}/m^3$, higher than in the first stage. A relatively weaker streamer head with a reduced electric field of approximately 40 Td forms at the upper edge of the plasma region about 30 ns after development of the lower wavefront. The region between the electrodes is located behind the two (upper and lower) streamer heads.

The following describes the trigger that drives the wavefront. As the electron number density increases, a space charge arises at the edge of the high-density region due to the difference between positive and negative species densities. At 160 ns, the space charge reaches an order of magnitude of $1\times10^{18}/m^3$, which is equivalent to the bulk plasma density. At this time, the space charge induces a local electric field of about 100 Td and drives the electric field wave front (streamer head).

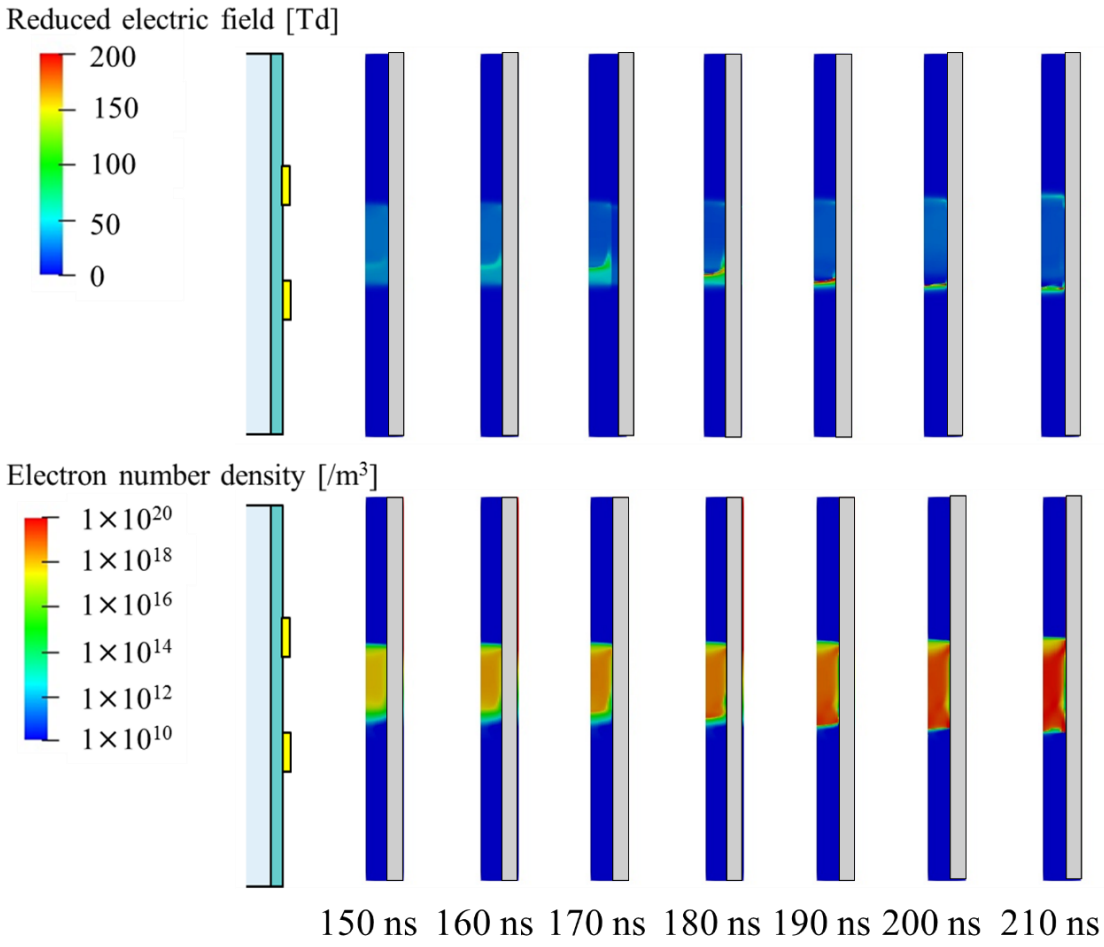

Figure 5.9. Spatiotemporal behaviors at the second stage (streamer-type discharge). The upper and lower rows show the reduced electric field and electron number density, respectively.

5.3.2.2.3 Third stage: transition to surface discharge and its development (after 210 ns)

Figure 5.10 shows contour maps for the simulated distributions of the reduced electric field and the electron number density. The electric field wavefront spreads radially as it propagates axially. When wavefronts reach the inner edge of each electrode, the discharge mode changes to a surface discharge that propagates near the dielectric surface. The surface discharge increases the electron number density near the dielectric surface to $1\times10^{20}/m^3$ as it propagates, and stops when it spreads to a slightly wider range than the electrodes. As a result, the distribution of the electron number density consists of two regions, a relatively uniform region between the electrodes and a high-density region near the dielectric surface above both electrodes. Nearly the same distribution sustains until 2000 ns by secondary discharges due to He_2*, as described below. This feature of the electron number density distribution agrees with previous works reporting that helium coaxial dielectric barrier discharge becomes the glow type [1], whereas a strong emission is observed near the dielectric surface above the electrode [2].

Figure 5.11 shows temporal behavior of distributions of the surface charge density and the reduced electric field 100 μm above the dielectric surface, at the center between the electrodes, and at the lower electrode. Solid lines in this figure show the surface charge density (left axis) and dashed lines show the reduced electric field (right axis). At the center between the electrodes (blue lines), change in the reduced electric field does not correspond to change in the surface charge density, and the surface charge density remains low (1×10^{-7}-1×10^{-6} C/m^2) over the entire time. This is because glow- and streamer-type discharges generate electrons in the gas region between the electrodes. Above the lower electrode (orange lines), on the other hand, rapid increases are observed in the surface charge density and the reduced electric field at about 220 ns. The surface

charge density reaches about 9×10^{-4} C/m^2. In this discharge mode, the electric field wavefront is driven by a local electric field induced by the surface charge, in addition to the local electric field of the wavefront itself. This seems to be a surface discharge. About 350 Td of the reduced electric field is enhanced near the dielectric surface as passing the discharge wavefront,

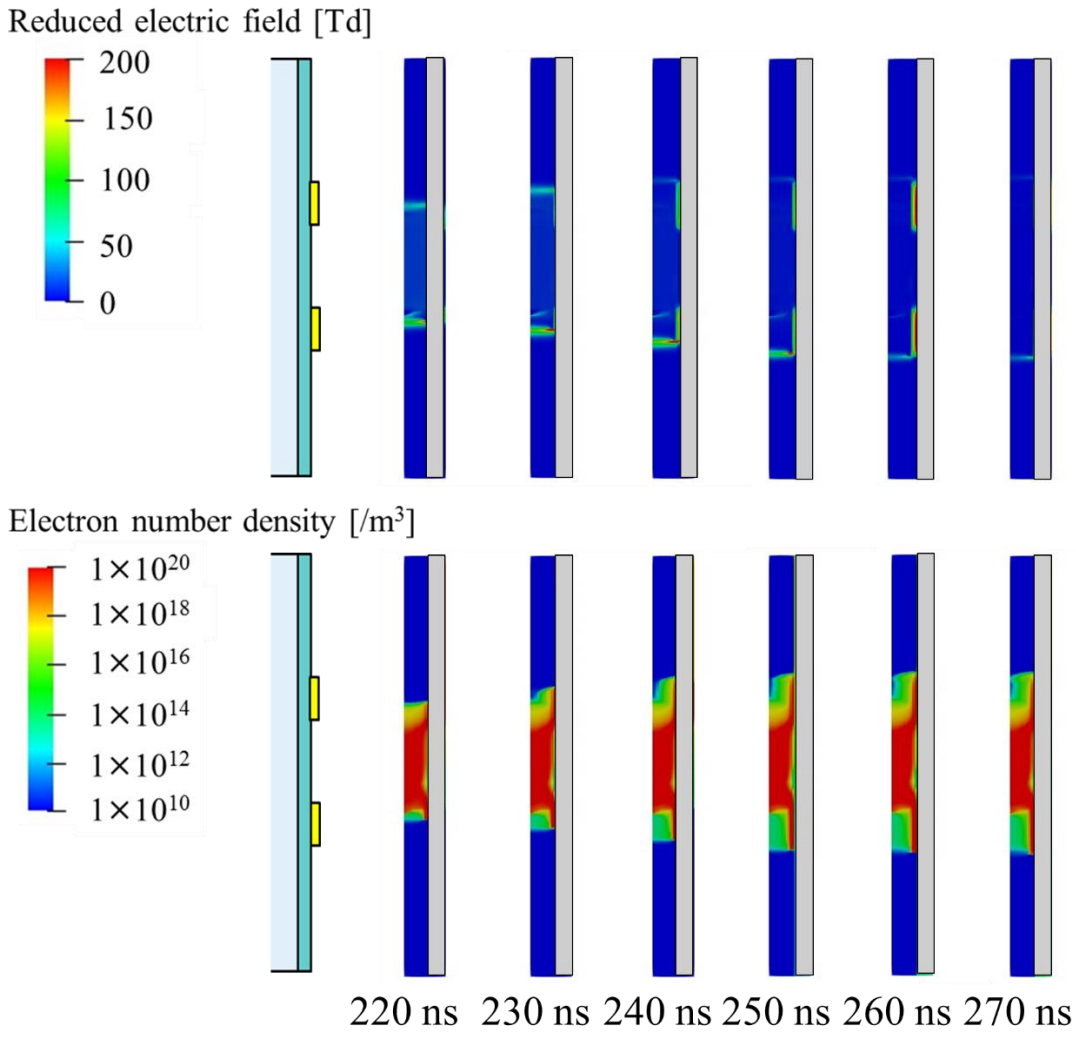

Figure 5.10. Spatiotemporal behavior in the third stage (surface-type discharge).

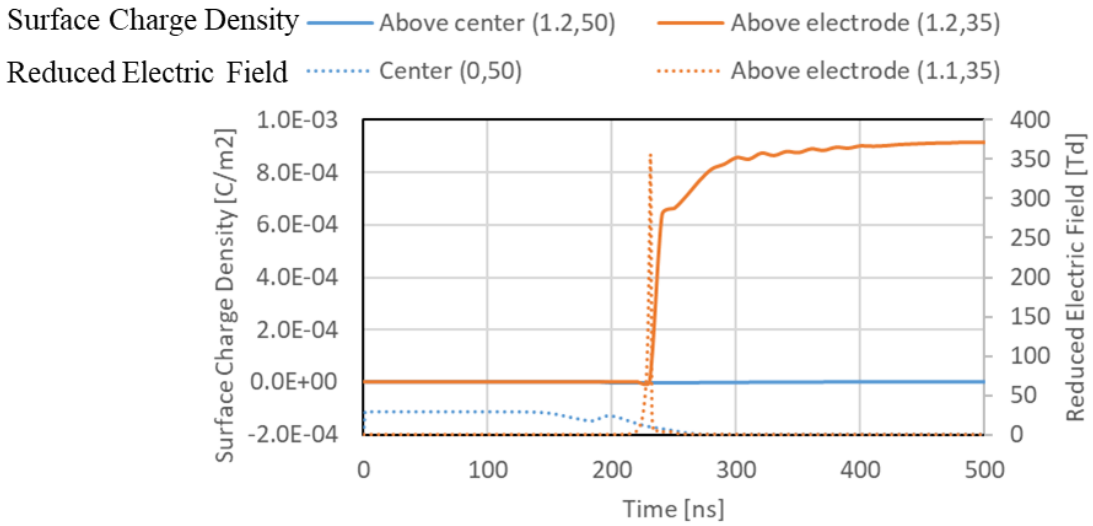

Figure 5.11. Time history of surface charge density at the dielectric surface (solid line) and reduced electric field near the dielectric surface (dashed line), at the center (blue), and at the lower electrode (orange).

5.3.2.2.4 Summary of each stage

The above analysis reveals the generation process of dielectric barrier helium discharge in a coaxial DBD device. In a coaxial DBD device, plasma develops in three stages: relatively uniform glow, axially propagating streamers (bullets), and surface discharge near the dielectric surface.

Previous studies have shown that in plasma actuators (a representative planar DBD), changing polarity of the applied voltage changes the discharge mode [22]. In the plasma actuator, one discharge mode basically corresponds to one discharge pulse. It has also been reported that rise time and slope of the applied voltage also affects the discharge properties in the case of nanosecond or microsecond pulses (much faster than commercial power frequencies) [23]. A previous study of plasma jets reported that helium discharge tends to transition to the surface-discharge mode, and it continues to propagate along the

surface beyond the tube exit when the ambient is pure helium [9]. In addition, three distinct discharge modes are observed in plasma jets [24], as phenomena occurring when bullets shoot out from the tube. To our knowledge, however, there have been no previous reports of transition in discharge mode in a coaxial DBD under one pulse. A unique feature of the coaxial DBD surrounding the dielectric is that it encourages a transition to surface discharge. Moreover, as our results show, the grounded electrode is another important control parameter for discharge propagation, acting like a brake on propagation.

5.3.2.3. Species composition of helium plasma in coaxial DBD device

As the previous section showed, plasma is generated in different discharge modes between the electrodes and near the dielectric surface above the electrodes. The following describes the species composition of helium DBD plasma. In a reactor-type DBD, metastable species are likely to be important for chemical processes through the Penning effect and such, and these behaviors are discussed.

Figure 5.12 shows distributions of each species density at 2000 ns. Similar to the electron number density distribution, the distributions for all species have high-density regions between the electrodes and near the dielectric surface above both electrodes. Streamer discharge in the second stage and surface discharge in the third stage also propagates toward the upper electrode (the voltage-applying electrode). Although the species distributions spread a bit widely at the lower side, differences between the upper and lower sides are small. In actual situations, each species will be delivered by gas flows at much longer timescales (ms). Therefore, for example the density of He_2* is likely to be higher downstream.

Dominant species in coaxial DBD helium plasma are He_2*, He*, E, and He_2^+, followed by He^+, which shows very little presence as compared to the other species. Species composition in the plasma is unchanged between positions (discharge modes). At 2000 ns, the number densities of He_2* and E are about $5\times10^{19}/m^3$ and $1\times10^{19}/m^3$ at the center between the electrodes, and about $1\times10^{21}/m^3$ and $2\times10^{19}/m^3$ near the dielectric surface above the lower electrode. Previous works [6, 15] have reported He_2* as the dominant species in atmospheric pressure helium glow discharge in parallel plates, which agrees with our results.

Figure 5.13 shows time evolutions of species number densities for both positions. The solid lines shows that all species densities increase until 2000 ns simultaneously with applied voltage. This increase is due to the glow-type discharge in the first stage, as shown in the previous subsection. The slope decrease at about 170 ns is due to axial passage of the streamer head. The center between the electrodes is located behind the streamer head, so the electric field decreases there, thereby decreasing the electron temperature. After that, a gradual change is observed between the electrodes. He* and He^+ decreases due to progressing chemical reactions with He (ground-state atom), whereas He_2* and He_2^+ continues to increase as a result of these reactions. The electron number density is temporarily higher than the total of positive ions under streamer propagation, but the plasma subsequently (after about 200 ns) becomes electrically neutral.

Dashed lines in Fig. 5.13 indicate time evolutions of all species densities near the dielectric surface above the lower electrode. No remarkable increase in any species densities is observed until 230 ns (under the first and second stages), unlike at the center between the electrodes. A rapid increase in all densities is observed from about 230 ns, due to the surface discharge in the third stage. After passing of the ionization front of the

surface discharge, the electron temperature (dotted line) exceeds 100,000 K for about 40 ns, increasing the electron production rate (dashed line). All species densities exceed that at the center between the electrodes, due to the strong electric field enhanced by the accumulated charge on the dielectric surface. Changes after this rapid increase are moderate, like at the center between the electrodes.

Changes observed after the rapid increase between the two points also show differences. He_2^+ decreases with time near the dielectric surface (purple dashed line) and increases at the center between the electrodes (purple solid line). This corresponds to a gentler decrease of He^+ near the dielectric surface (green dashed line) than at the center (green solid line). These changes are likely induced by positive charge of the wall. He^+ near the wall receives a repulsive force from a positively charged wall and decreases faster near the dielectric surface, reducing chemical reactions and decreasing He_2^+.

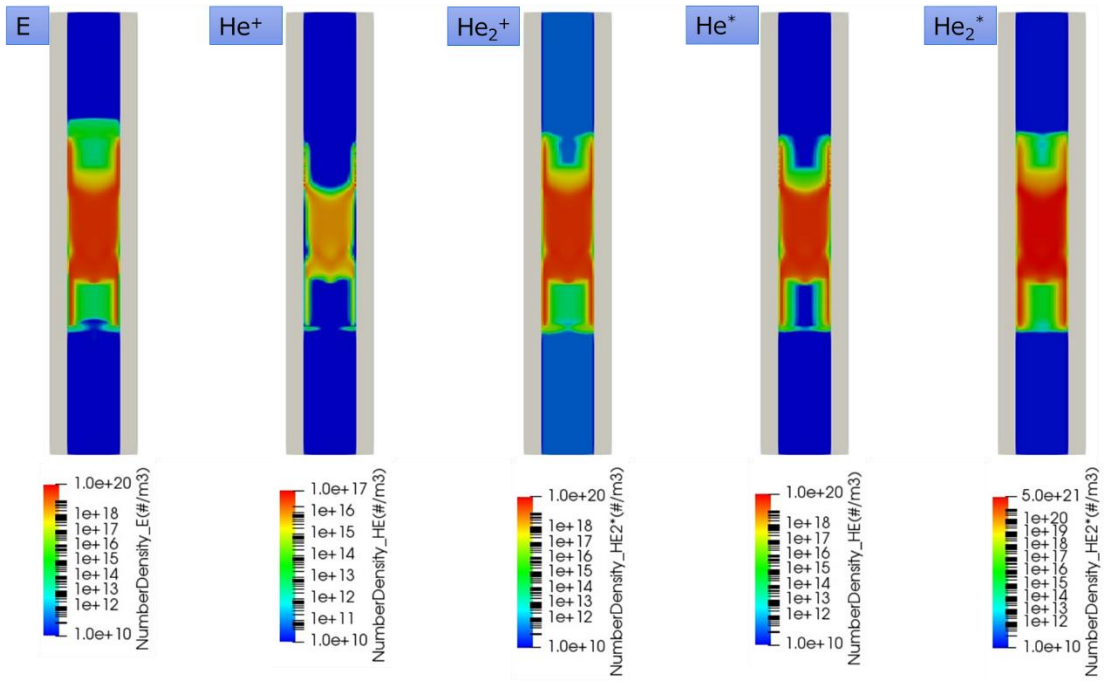

Figure 5.12. Distributions of species number densities at 2000 ns.

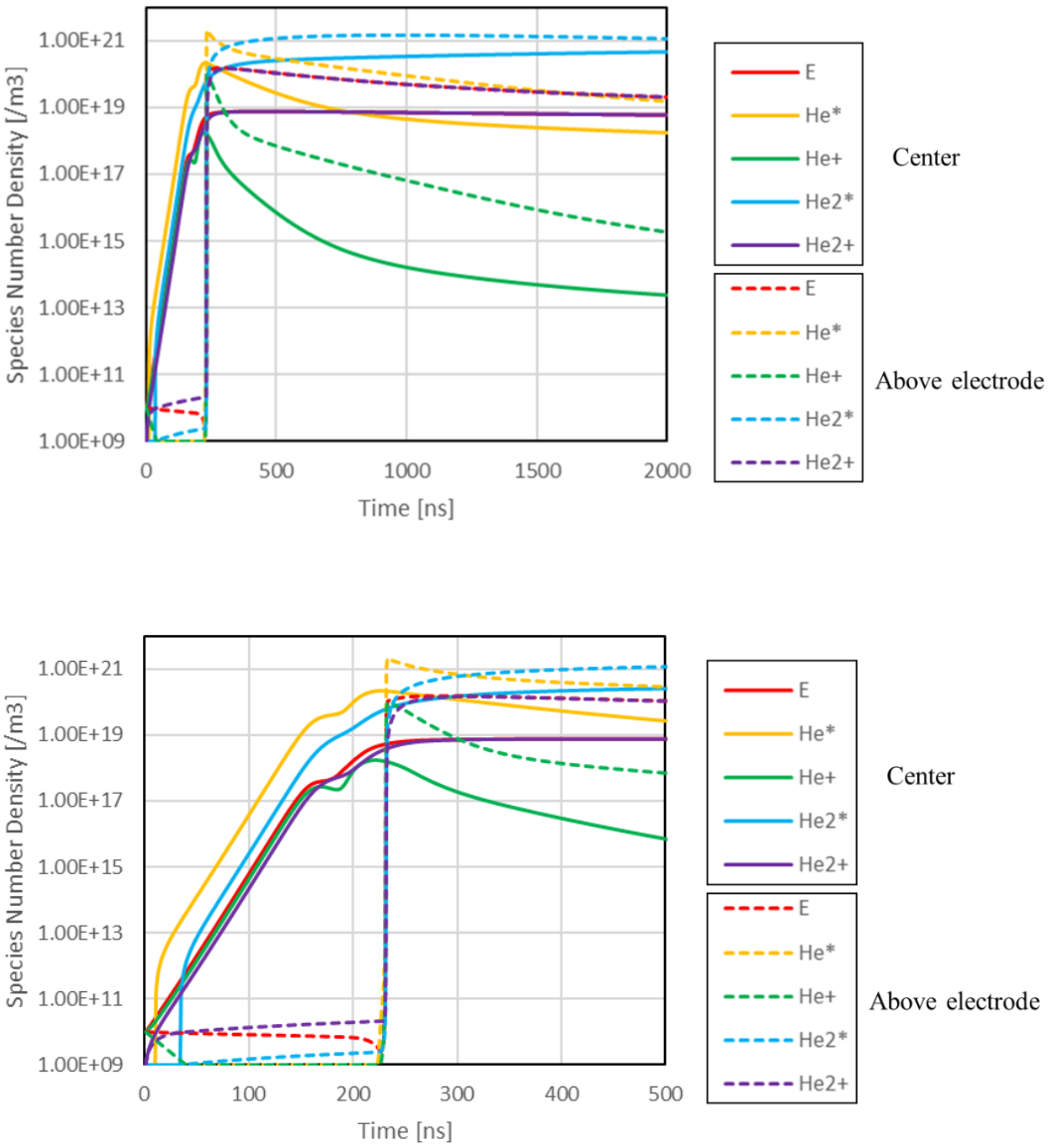

Figure 5.13. Time history of species number densities at the center between electrodes (solid line) and near the dielectric surface above the lower electrode (dashed line). At the center, species number densities rise through the first and second stages. Near dielectric surfaces, species densities rise through the third stage.

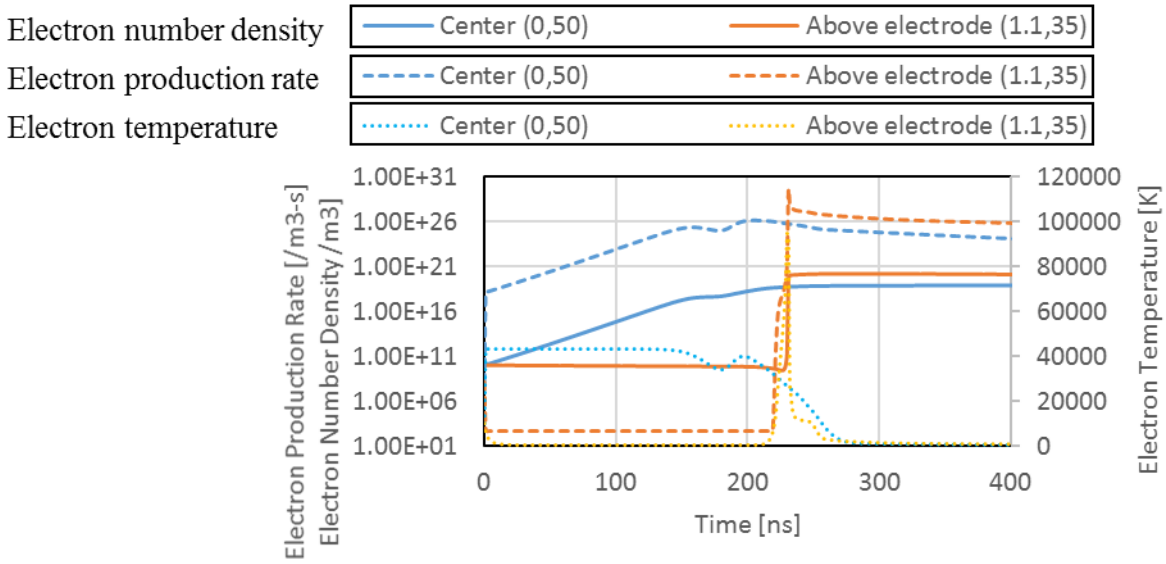

Figure 5.14. Time histories of electron number density (solid line), electron production rate (dashed line) and electron temperature (dotted line).

5.3.3. Parametric study of applied voltage and device configuration

In a reactor-type DBD, chemical species in plasma inside the device are directly used as a reactor for target gases. It is thus important to understand relations between the device parameters and distributions in the device. In experiments, it is not easy to measure detailed distributions inside the device, because the plasma volume is small and emissions from plasma passing through the dielectric are integrated values in the radial and axial directions. However, previous numerical simulations have assumed axial uniformity [16, 17], so relations between the parameters and distributions remain unclear, particularly in the axial direction.

This research thus conducted a parametric study of detailed plasma distributions in a coaxial DBD device, evaluating plasma uniformity and volume as an index. In this study, we investigated applied voltage, electrode gaps, dielectric barrier conditions (thickness and dielectric constant), and inner dielectric diameter.

Applied voltage

Figure 5.15 shows contour maps and radial and axial distributions of the electron number density for the base configuration at 2000 ns under applied voltages of 10, 15, and 20 kV. Similar to the base condition (15 kV), high-density regions form between the electrodes and near the dielectric surface above the electrodes. These distributions indicate that the basic process of plasma generation does not depend on voltage value. Rather, plasma develops through glow-type discharge between the electrodes, axially propagating streamer discharge, and surface discharge. However, a difference occurs in the 10 kV case, where the distribution becomes nonuniform in the region between the electrodes. This is induced by first-stage nonuniformity of the plasma distribution in glow

discharge, as shown in the next section. The radial distribution at the center between the electrodes (z = 50 mm) in the 10 kV case becomes a center peak at which density near the center is higher than at the edge (near the dielectric surface), whereas this distribution is nearly uniform in the 15 and 20 kV cases.

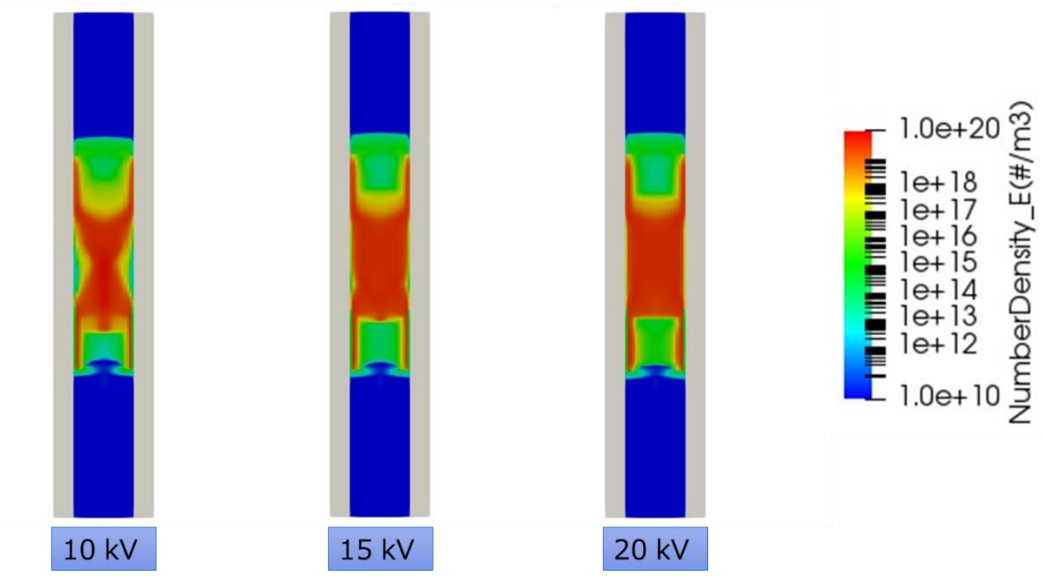

(a) Contour maps of electron number density for different applied voltage.

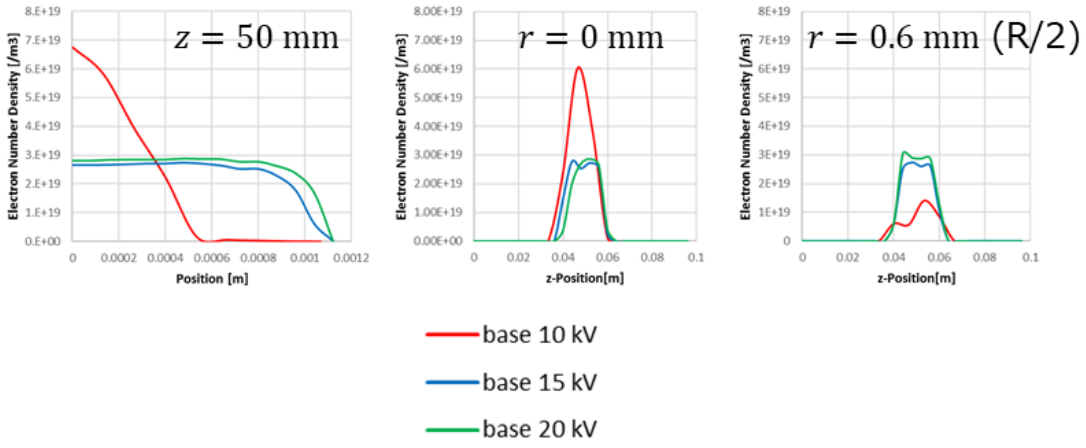

(b) Radial and axial distributions.

Figure 5.15. Distributions of electron number densities at 2000 ns under different applied voltage.

Gap between electrodes

Figure 5.16 shows contour maps and radial and axial distributions of electron number densities at 2000 ns for between-electrode gaps of 10, 20 (base), and 30 mm. Like the results of the applied voltage study, the basic distributions remain under all gap conditions. The author observed high-density regions located between the electrodes and near the dielectric surface above the electrodes. The surface discharge too propagates similarly, though a bit wider than the electrode edges, regardless of the gap, and with the plasma region widening with larger gaps.

Differences are also observed with different gaps. In the 30 mm case, the radial distribution (z = 50 mm) becomes a center peak. This distribution is similar to the 10 kV case. Subsequent analyses showed similar radial nonuniformity in cases of thicker dielectric and lower dielectric constant. The electric field becomes lower under these conditions, and this is an important factor behind the nonuniformity.

In the examined gap ranges, increasing the gap results in a broader plasma region but decreases uniformity. Most previous studies have assumed radial or axial uniformity [16, 17], but the results of this study revealed that distributions become both radially and axially nonuniform, depending on the electrode gap. Analyses of the applied voltage conditions suggest that applying higher voltage would likely increase distribution uniformity. The next section discusses uniformity and plasma volume, which are important from the perspective of application as a reactor.

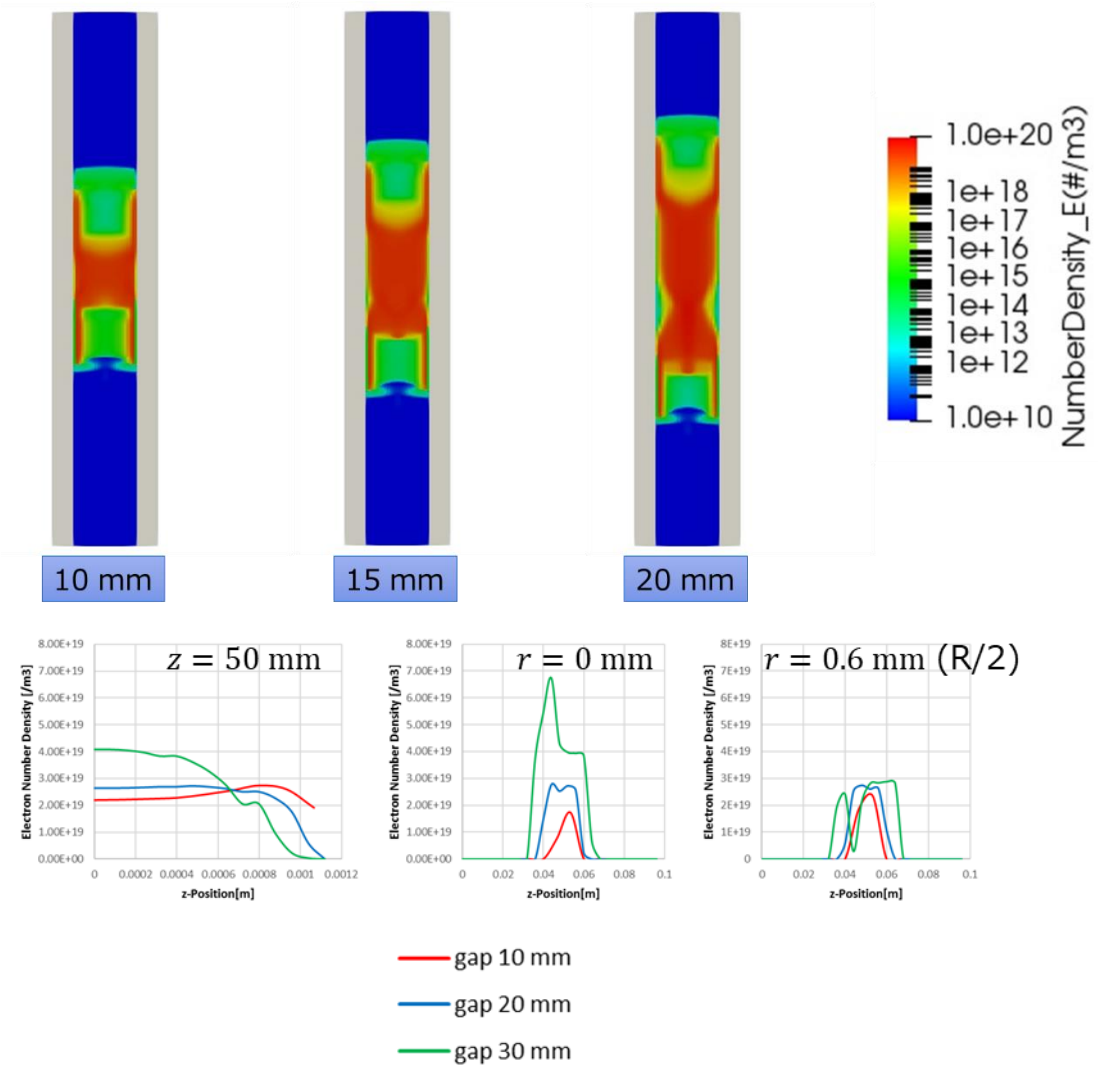

Figure 5.16. Distributions of electron number densities at 2000 ns under different gap voltages.

Dielectric constant and thickness of dielectric barrier

Figure 5.17 shows contour maps and radial and axial distributions of the electron number density at 2000 ns with different dielectric thicknesses and dielectric constants. The dielectric thicknesses are 0.5, 0.8 (base), and 2 mm, and the dielectric constants are 5, 10 (base), and 15.

Neither dielectric thickness nor dielectric constant drastically changes the distributions; as under the other conditions, high-density regions arise in the region between the electrodes and near the dielectric surface above the electrodes. A low-density region arises between the electrodes in cases with thicker dielectric (2 mm) and lower dielectric constant (5). The electric field in the gas region decreases in these cases, as in the low-voltage (10 kV) and larger gap (30 mm) cases.

The following discusses surface charge density accumulating on the dielectric surface. Figure 5.18 shows time evolutions of surface charge density and values at the dielectric surface above the lower electrode at 500 ns. The surface charge density increases as surface discharge wavefronts pass that position, nearly reaching steady states (Figs. 5.18(a) and (b)). The surface charge density increases with decreasing dielectric thickness and with increasing dielectric constant.

The dielectrics act as a capacitor, and these conditions increase their capacitance, increasing the surface charge density. For a constant area, thickness and dielectric constant determine capacitor capacitance. Figure 5.18(c) shows relations between surface charge density and the ratio of dielectric constant to dielectric thickness. As the blue line shows, surface charge density and dielectric constant are proportional. The orange line shows saturation of surface charge density with thinner (larger ratio) dielectrics. These

results indicate that using materials with higher dielectric constant would likely increase the surface charge density and enhance surface discharge.

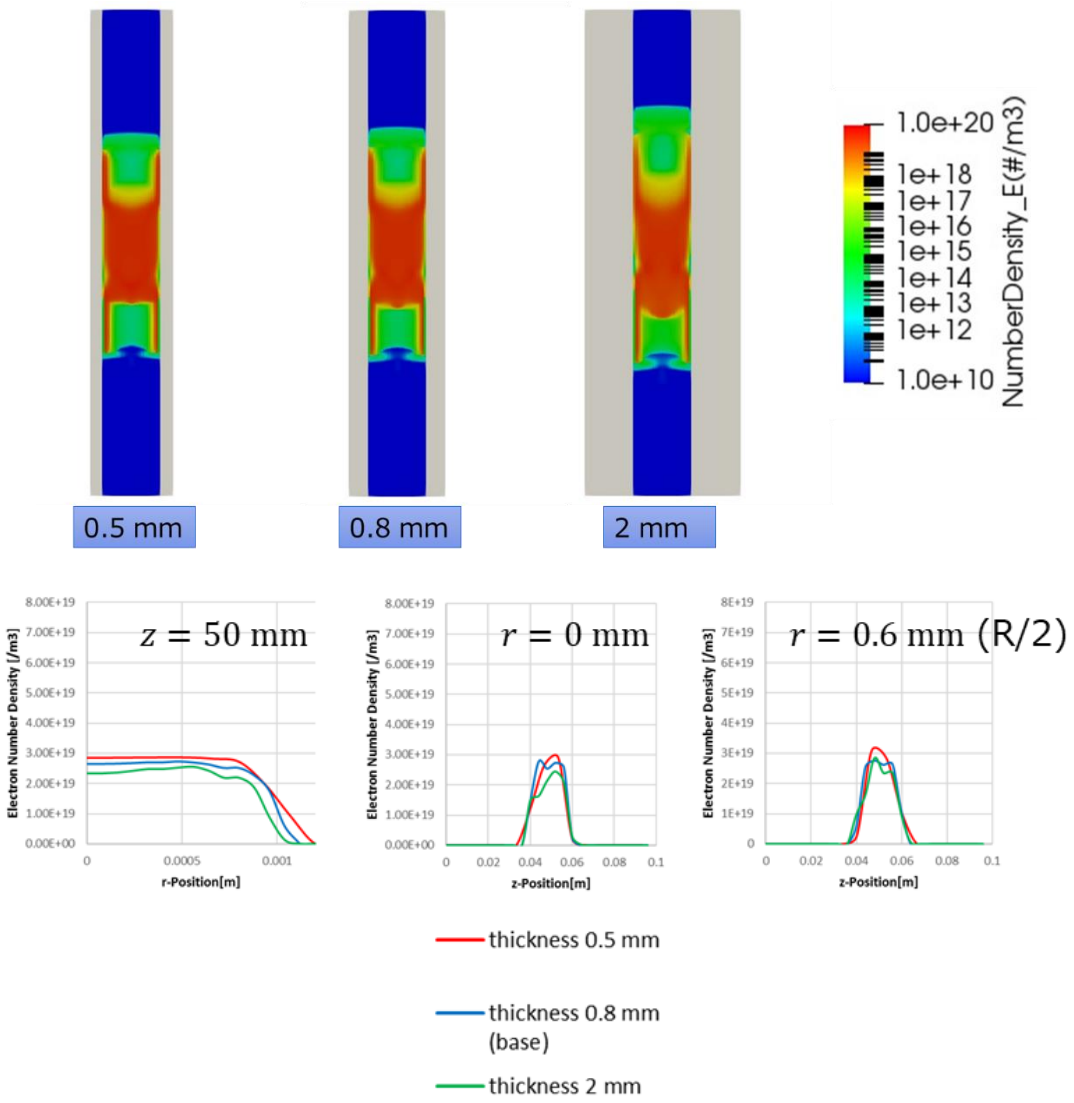

(a) Dielectric barrier thickness.

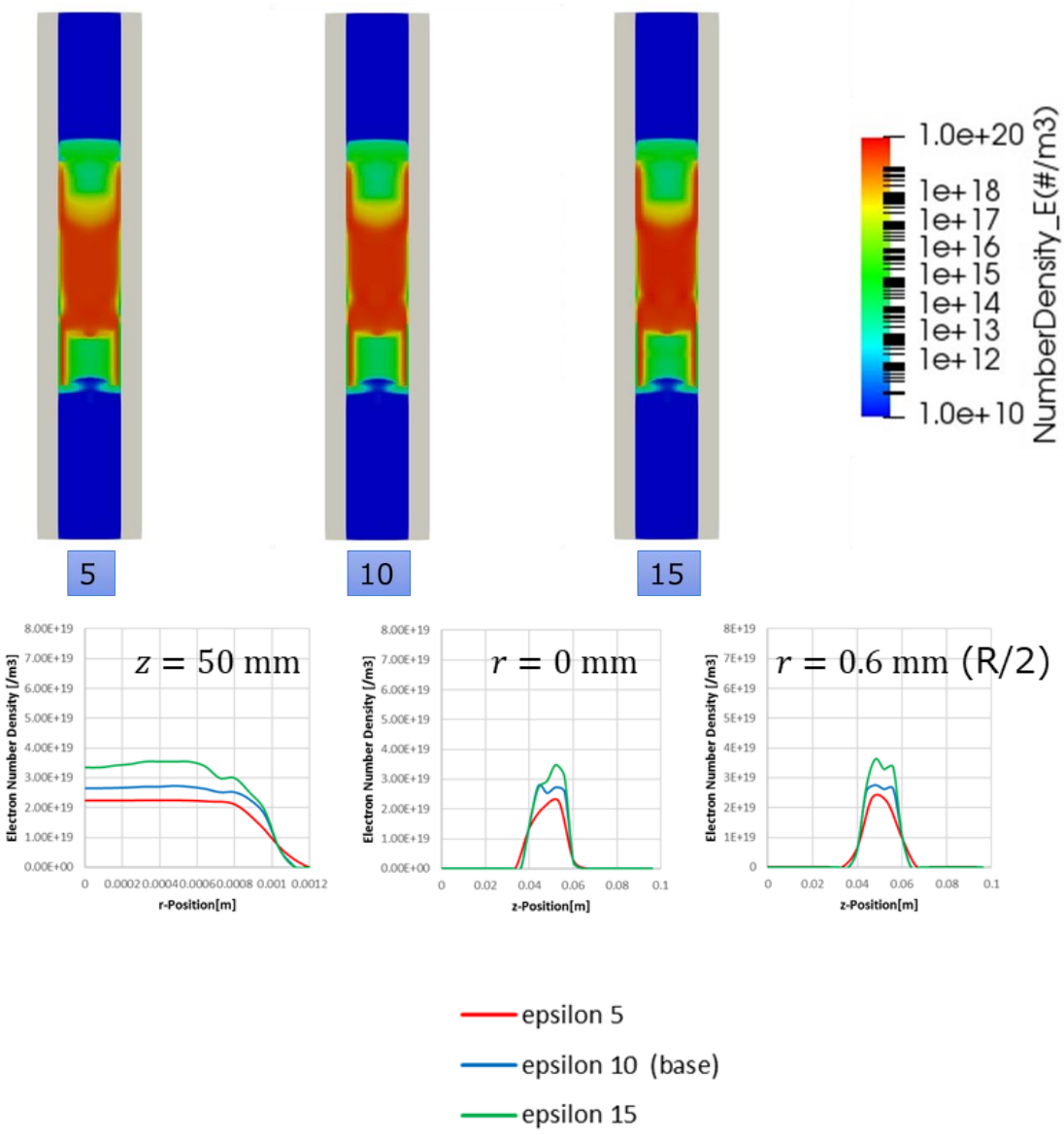

(b) Dielectric constant.

Figure 5.17. Distributions of electron number densities at 2000 ns with (a) different dielectric barrier thicknesses and (b) different dielectric constant.

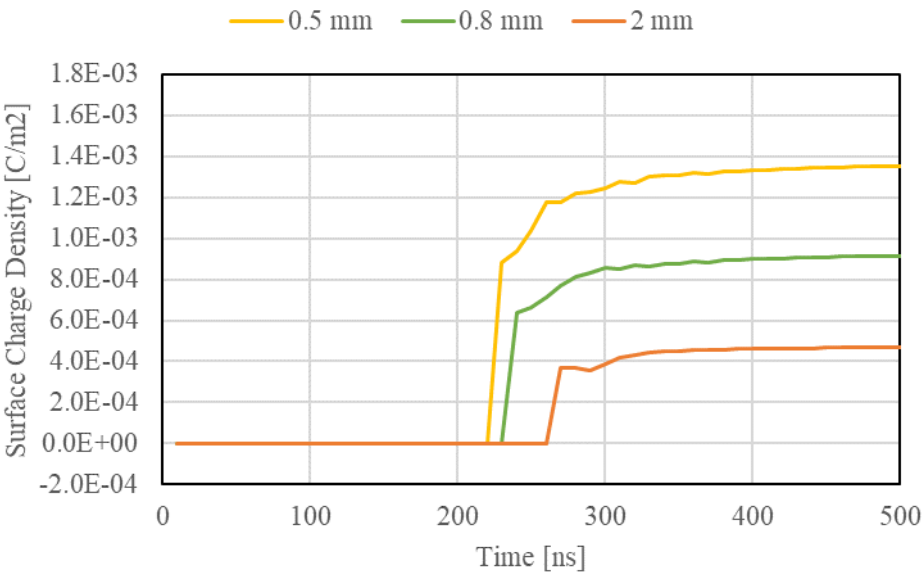

(a) Time history with different thicknesses.

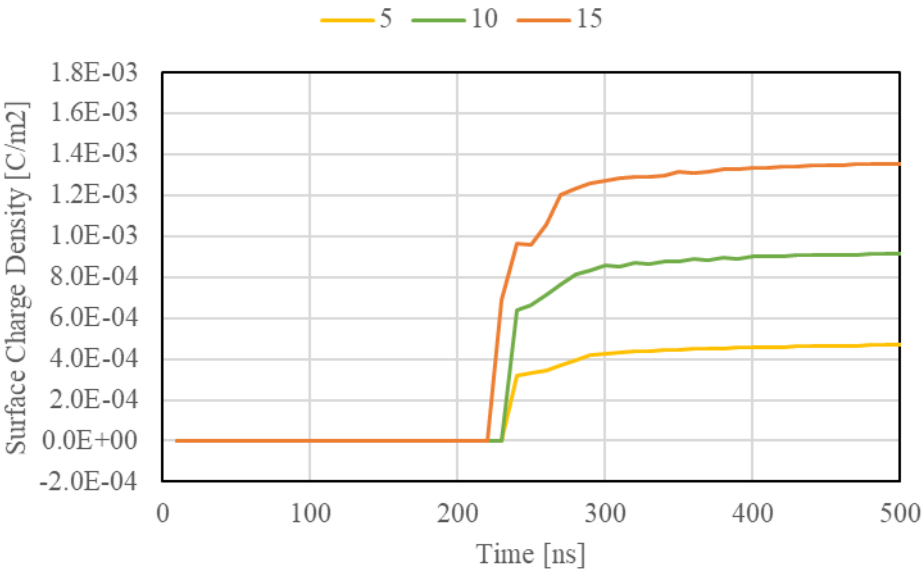

(b) Time history with different dielectric constants.

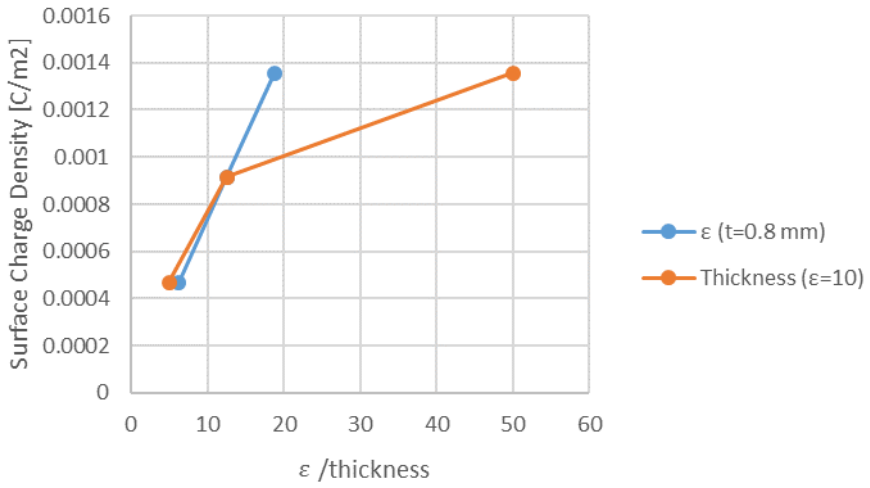

(c) Surface charge density at 500 ns.

Figure 5.18. Surface charge densities with different dielectric barrier thicknesses and dielectric constants.

Inner diameter

Dielectric tubes with larger inner diameter improve processing flow rate and reduce flow-pressure loss. The following describes our investigations of the influence of dielectric tube inner diameter on electron number density distributions.

Figure 5.19 shows contour maps and radial and axial distributions of the electron number density at 2000 ns for inner diameters of 2.4 (base), 4, and 6 mm. The base distributions remain the same for all other conditions. Increasing the inner diameter decreases the electron number density and reduces uniformity of the radial distribution (z = 50 mm). The author also observed that increasing the inner diameter narrows and lowers the high density region in the axial direction.

These results indicate that simply increasing the inner diameter reduces uniformity and electron number density. Further, the analyses so far suggest that applying higher voltage and using a thinner dielectric is likely to enhance the electric field in the gas region and to improve the distributions. Moreover, it is suggested that simultaneously adjusting both the between-electrode gap and the inner diameter effectively controls uniformity and distributions.

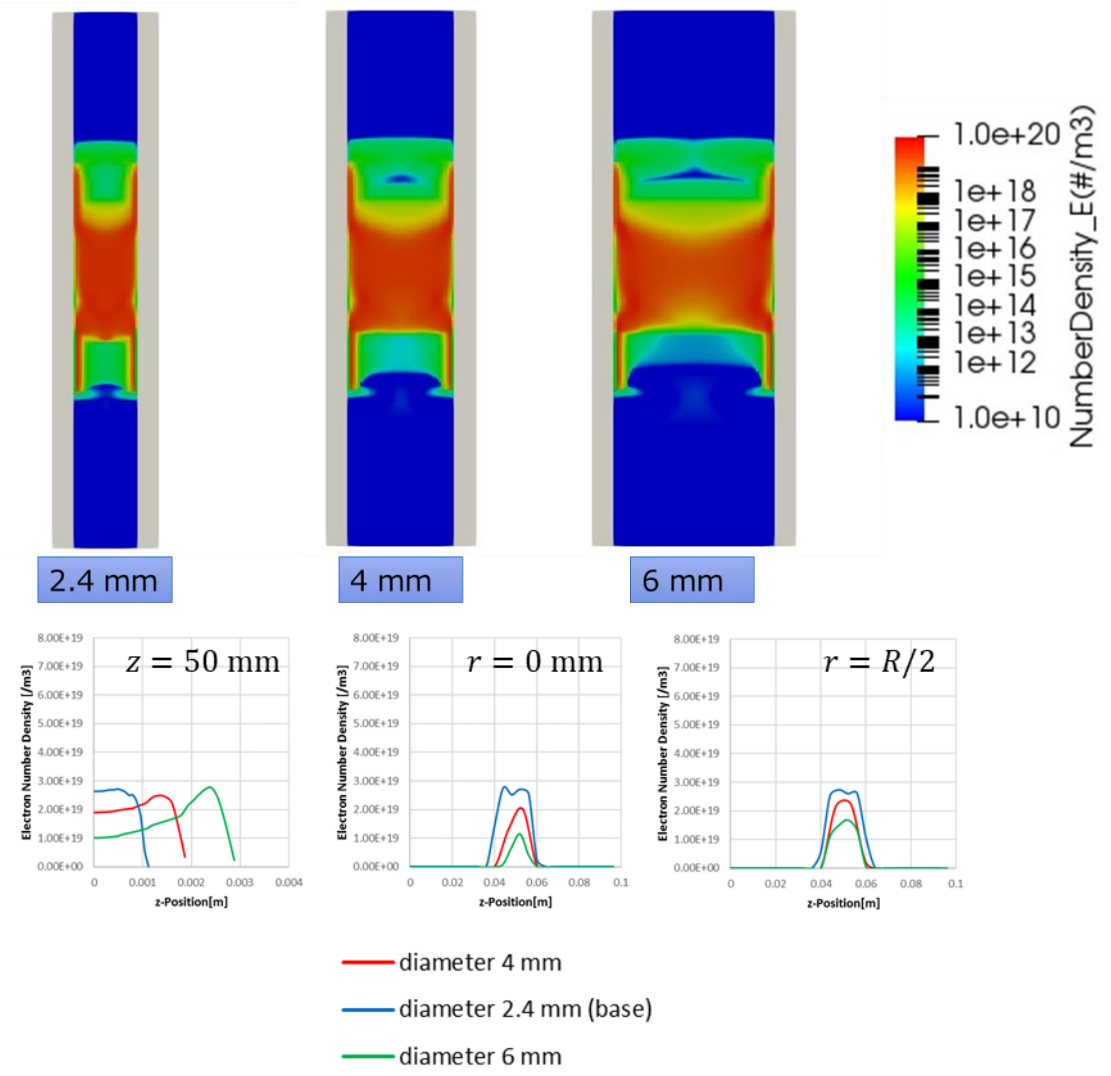

Figure 5.19. Distributions of electron number densities with different inner diameters.

5.3.4. Nonuniformity and volume of plasma electron distribution

Based on the results presented in the previous section, this section discusses the generation process of nonuniformity, uniformity and plasma region volume, and required characteristics for dielectrics.

5.3.4.1 Generation process of the plasma nonuniformity

Plasma distributions in a coaxial DBD device become less uniform with lower voltage, larger electrode gap, lower capacitance, and larger inner diameter. As shown in the previous section, these conditions decrease the electric field in the region between the electrodes, and lower uniformity in radial distributions in all cases. These common features indicate that factors inducing nonuniformity are basically the same.

The author takes the low-voltage (10 kV) condition as an example for discussing the generation process of less-uniform distributions. Figure 18 shows spatiotemporal behaviors of the reduced electric field and the electron number density in the 10 kV case. As in the 15 kV case (Fig. 5.20), a high-density region forms between the electrodes by 440 ns. This is first-stage glow-type discharge. This high-density region spreads over the entire gap between the electrodes in the 15 kV case, but is limited to the upper half between the electrodes in the 10 kV case, due to the narrower high electric field (electron heating) region induced by the lower applied voltage. Similar to the 15 kV case, the second-stage streamer head forms at the edge of the high-density region, but the streamer head shape is sharper. This sharp streamer head generates electrons as an axial propagation, but passes only near the axis region. Electrons are thus generated only near the axis, resulting in a nonuniform radial distribution with a center peak. The streamer

discharge radially spreads with axial propagation, transiting to surface discharge as in all other conditions.

The less uniform distribution of the 10 kV case is thus induced by narrow, nonuniform high-density regions in first-stage glow-type discharge due to the low electric field generated by the low applied voltage. This nonuniform distribution is enhanced by axially propagating streamer discharge in the second stage and by surface discharge in the third stage.

From the analyses above, to understand the distributions in a coaxial DBD, it is important to reproduce all three plasma development steps: generation of a high-density region by glow discharge, axial propagation of streamer discharge, and surface discharge. Moreover, control of plasma distributions will likely require generation of somewhat uniform plasma between the electrodes.

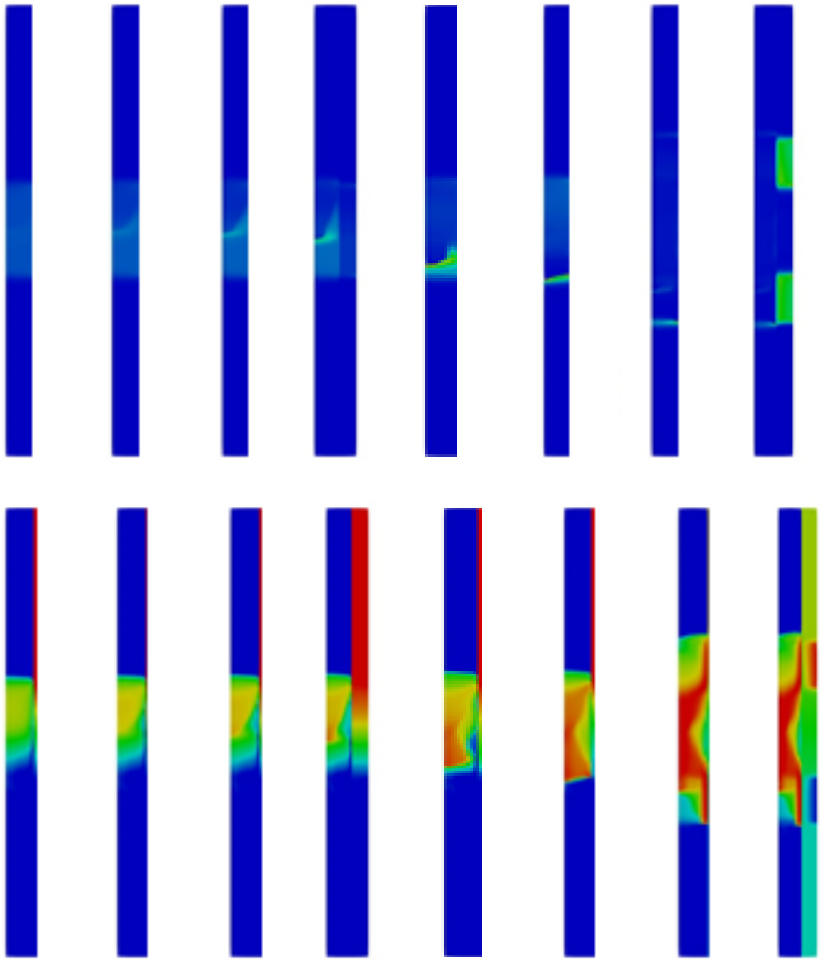

Figure 5.20. Spatiotemporal behavior under 10 kV conditions. The upper image shows reduced electric field, and the lower image shows electron number density.

5.3.4.2 Average electron number density, uniformity and relative plasma region

A reactor-type DBD device generally requires a high-density plasma and a broad plasma region. This section discusses average electron number densities, radial plasma uniformity, and relative plasma regions, summarized in Table 5.3.

The average electron number density is calculated based on the electron number density in the region surrounded by the electrodes. The radial uniformity of the plasma is evaluated as

$$\text{Radial uniformity} = \frac{Ne_{r=0.8R}}{Ne_{r=0}},$$

based on the ratio of electron number densities on the z-axis (r = 0 mm) to $r = 0.8R$ at the center between the electrodes (z = 50 mm). Because the electron number density rapidly decreases at the wall under all conditions, $r = 0.8R$ is used as the indicator. The radial distribution is uniform if the radial uniformity is 1, center-peaked if the radial uniformity is greater than 1, and edge-peaked if the radial uniformity is less than 1.

The relative plasma region considers the region where the electron number density is greater than $1\times10^{14}/m^3$ and uses a value normalized with the results of the base 15 kV case. This indicator shows that the voltage or the configuration grows the plasma region if the relative plasma region is greater than 1, and shrinks it if the value is less than 1.

Results showed that the applied voltage improves all indicators. Therefore, while safety and power costs generally call for low-voltage operations, high voltage is to some extent useful for a coaxial DBD. As the previous subsection showed, radial uniformity reduces in the 10 kV case.

Increasing and decreasing the gap between electrodes has opposite effects on the indicators. A shorter (10 mm) gap improves radial uniformity, but reduces average

electron number density and relative plasma region. In the 10 mm case, there is insufficient time for the streamer discharge to propagate in the second stage. This causes less electron generation and a faster transition to surface discharge. A longer (30 mm) gap reduces radial uniformity, but improves average electron number density and relative plasma region. These results indicate that the second-stage streamer discharge is important for increasing electron number density and controlling distributions, as is the existence of an optimal gap.

Regarding the dielectric conditions, similar changes occur in the same direction of capacitance change. Increasing capacitance (0.5 mm thickness and dielectric constant of 15) increases average electron density, but reduces the relative plasma region. Conversely, decreasing capacitance (2 mm thickness and dielectric constant of 5) decreases average electron density, but increases the relative plasma region. Especially in the case of 2 mm thickness, the relative plasma region shows a high increase (about 20%). As Fig. 15 shows, the electron number density distribution generated by streamer propagation enlarges in this case. Figure 16(a) shows that the surface charge density is lower than in the other thickness cases, and that timing of the rise is delayed in the 2mm case. These results indicate that the delayed transition from streamer to surface discharge improves the relative plasma region.

Finally, we discuss the effects of the inner diameter of the dielectric. The relative plasma region increases with increased inner diameter, but the average electron number density decreases. In the 6 mm case, the average electron number density becomes about half that of the 2.4 mm case, but the relative plasma region doubles. While appropriate plasma properties depend on the application and balance with residence time (flow rate), the inner diameter has the largest effect on plasma region enlargement.

Interactions between parameters should be investigated to understand and acquire design guidelines for coaxial DBD devices. Optimization of device configurations is beyond the scope of this work, but adjusting both the gap between the electrodes and the inner diameter of the dielectric may simultaneously improve both density and distribution.

Table 5.3. Average electron number density, uniformity, and relative plasma region.

	Average electron number density [/m3]	Radial uniformity [-]	Relative plasma area [-]	comments
Voltage				
10 kV	**1.1E+19**	**0.00093**	**0.92**	
15 kV	**1.2E+19**	**0.86**	**1.00**	**base**
20 kV	**1.3E+19**	**0.93**	**1.04**	
Gap				
10 mm	**8.4E+18**	**1.19**	**0.78**	
20 mm	**1.2E+19**	**0.86**	**1.00**	**base**
30 mm	**1.5E+19**	**0.23**	**1.04**	
Dielectric thickness				
0.5 mm	**1.3E+19**	**0.70**	**0.92**	
0.8 mm	**1.2E+19**	**0.86**	**1.00**	**base**
2 mm	**1.0E+19**	**0.79**	**1.18**	
Dielectric constant				
5	**9.8E+18**	**0.64**	**1.03**	
10	**1.2E+19**	**0.86**	**1.00**	**base**
15	**1.4E+19**	**0.75**	**0.98**	
Diameter				
2.4 mm	**1.2E+19**	**0.86**	**1.00**	**base**
4 mm	**8.9E+18**	**1.29**	**1.43**	
6 mm	**6.7E+18**	**2.66**	**1.90**	

5.3.4.3 Effects of dielectric barrier

Dielectric barriers in coaxial DBDs play the important role of preventing transitions to arc and excessive current. To promote discharge and low-voltage operations, thinner dielectrics with higher dielectric constants are preferable, because they prevent voltage drop. However, dielectrics should also have long lifespans and high durability, but thinner dielectrics generally have reduced lifespan, durability, and safety. Moreover, device heating due to discharge may cause problems.

Investigating the effects of dielectric thickness and dielectric constant on plasma density and distributions, we observed conflicting changes between average electron number density and relative plasma region. For example, thinner dielectrics increased average electron number density but decreased relative plasma region. Even so, the effects of dielectric properties on basic plasma distributions were limited; high-density regions still form in the region between the electrodes and near the dielectric surface above the electrodes.

In conclusion, the effects of dielectric properties on plasma distributions are not so large as to drastically change basic plasma distributions. It is therefore possible to prioritize voltage, safety, and durability over plasma distributions, so long as sufficient discharge occurs.

5.4 Conclusion

This chapter applied experimental and numerical analyses to investigate DBD plasma in coaxial DBD devices. Experimental analyses confirmed that argon DBD inside the device formed a filament-like mode with three-dimensional structures.

This research used a self-consistent, multispecies, multitemperature plasma fluid model to analyze the formation process of helium plasma in a coaxial DBD. The results indicated that plasma forms in a reactor-type DBD through three discharge modes. First, a glow-like discharge is generated between the electrodes, and when the space charge due to the difference in positively and negatively charged species densities reaches the same level as that of the bulk plasma ($1\times10^{18}/m^3$), an electric field wavefront is formed and a streamer-like (bullet-like) discharge develops in the axial direction. Finally, when the electric wavefront reaches the dielectric surface, it transitions to a surface discharge strengthened by the accumulated charge, and the discharge fully propagates to the electrodes. At this time, the surface charge density is about 9×10^{-4} C/m^2. Compared with an electron number density of $1\times10^{19}/m^3$ between the electrodes, that near the electrodes is as high as $1\times10^{20}/m^3$, confirming that the strong emission in this region is due to surface discharge. This plasma formation process is quite different from that in a planar DBD, where one discharge mode basically corresponds to one discharge pulse. This research confirmed the development of bullets in a reactor-type DBD, as in the case of a plasma jet, but they are trapped by a strong electric field (momentarily about 350 Td) due to the electric field induced by a combination of the ground electrode and the accumulated charge. Further, the propagation distance is short (6 mm) and it immediately transitions to a surface discharge. This suggests the possibility of controlling plasma bullets not only

by distance between the electrode and the tube outlet, but also by the electrode structure (arrangement).

A parametric study indicated that the inner diameter has the largest effect on plasma region enlargement. Radial uniformity of the electron number density depends on distributions of first-stage glow discharge. In the cases of lower applied voltage, thicker dielectric, lower dielectric constant, larger inner diameter, and larger gap, the resulting lower electric field in the region between the electrodes narrows the glow plasma, and subsequent streamer propagation forms radial nonuniformities. Dielectric properties can be chosen considering safety, durability, and controllability, because basic plasma distributions have relatively small effects.

References

1. N. M. Bourdet, M. Laroussi, A. Begum, and E. Karakas, J. Phys. D: Appl. Phys. **42**, 055297 (2009).
2. X. J. Shao, N. Jiang, G. J. Zhang, and Z. X. Cao, Appl. Phys. Lett. **101**, 253509 (2012).
3. Z. S. Chang, C. W. Yao, S. L. Chen, and G. J. Zhang, Phys. Plasma **23**, 093503 (2016).
4. Q. Li, H. Takana, Y. K. Pu and H. Nishiyama, IEEE Trans. on Plasma Sci. **42**, 10, pp.2360-2361 (2014).
5. H. Y. Lee, J. H. Choi, J. W. Hong, G. C. Kim, and H. J. Lee, J. of Phys. D: Appl. Phys. **51** 21 (2018).
6. J. L. Walsh, F. Iza, N. B. Janson, V. J. Law and M. G. Kong, J. Phys. D: Appl. Phys. **43** 075201 (14pp) (2010).
7. X. Y. and L. L. Raja IEEE trans. Plasma Sci. **31** 495-503 (2003).
8. G. Hagelaar and L. Pitchford, Plasma Sources Sci. Technol. **14** 4 722 (2005).

9. D. Breden, K. Miki and L. L. Raja, Appl. Phys. Lett. **99** 111501 (2011).
10. Y. Sato, K. Ishikawa, T. Tsutsumi, A. Ui, M. Akita, S. Oka, and M. Hori, J. Phys. D: Appl. Phys. **53**, 265204 (2020).
11. Y. Sato, K. Ishikawa, T. Tsutsumi, and M. Hori, Appl. Phys. Express. **13**, 086001 (2020).
12. U. N. Pal, A. K. Sharma, J. S. Soni, S. Kr, H. Khatun, M. Kumar, B. L.Meena, M. S. Tyagi, B. J.. Lee, M. Iberler, J. Jacoby, and K. Frank, J. Phys. D: Appl. Phys. **42** 45213 (2009).
13. P. Bruggeman and R. Brandenburg, J. of Physics D: Applied Physics **46** 46 (2013).
14. K. Takeda, T. Kumakura, K. Ishikawa, H. T., M. S. and M. Hori, Appl. Phys. Express **10** 036201 (2017).
15. F. Tochikubo, T. Chiba and T. Watanabe, Jpn. J. Appl. Phys. **38** 5244–5250 (1999).
16. S. Gadkari and S. Gu, Phys. Plasmas **24** 53517 (2017).
17. D. Petrovic´, T. Martens, J. Van Dijk, W. J. M. Brok, and A. Bogaerts, **42** 205206 (2009).
18. X Lu, M Laroussi and V Puech, Plasma Sources Sci. Technol. **21** 3 (2012).
19. X. P. Lu and K. K. Ostrikov, Appl. Phys. Rev. **5**, 031102 (2018).
20. Ronny Brandenburg, Plasma Sources Sci. Technol. **26** 053001 (2017).
21. X. Li, N. Zhao, T. Fang, Z. Liu, L. Li, and L. Dong, Plasma Sources Sci. Technol. **17**, 015017 (2008).
22. A. R. Hoskinson, L. Oksuz, and N. Hershkowitz, Appl. Phys. Lett. **93**, 221501 (2008).
23. K. Gao, R. Liu, P. Jia, C. Ren, K. Wu, X. He, and X. Li, AIP Adv. **9**, 115210 (2019).
24. J. L. Walsh, F. Iza, N. B. Janson, V. J. Law, and M. G. Kong, J. Phys. D: Appl. Phys. **43**, 075201 (2010).

Chapter 6 Gas decomposition by coaxial dielectric barrier discharge plasma

6.1 Introduction

This section discusses gas decomposition properties in LTAPP as an application utilizing interaction between gas molecules and LTAPP. To understand decomposition mechanisms and ensure safety, it is important to investigate by-products of the decomposition process. Measurements of by-products also facilitate detailed understanding of interactions between gas molecules and plasms. The author uses IAMS in this study because of its low fragmentation, and discusses the decomposition process based on experimental results.

6.2 Experimental setup

Figure 6.1 shows a schematic and photographs of the experimental setup. The experimental system consists of a sampling part, a DBD part and an IAMS part. In the sampling part, argon gas is introduced and bubbled into sample ethanol or butanol. The argon mixture and the sample is then introduced to the DBD part, which is the same as the DBD device described in the previous section. This research applies a 60 Hz, 15 kV voltage between copper electrodes to produce a DBD plasma. The argon-sample mixture is exposed to the discharge plasma when voltage is applied, and part of that may be decomposed by chemical reactions.

After passing through the DBD device, the mixture enters the IAMS apparatus for analysis. There are several IAMS parameters for sample gas molecule detection and spectrum analysis, listed in Table 6.1. “SEM” and “scan speed” are parameters for

adjusting IAMS spectrum intensities. “Filament current” adjusts Li^+ amounts, and “emitter bias” reduces Li^+ energy. We set these values while checking the spectrum, referring to developer (Canon Anelva Technics) recommendations.

This research investigated decomposition properties of the sample butanol molecules by comparing IAMS spectra of cases with and without applied voltage (discharge). Before each measurement, discharge plasma is generated to clean inside the tube for 2 min. Measurements were repeated five times and averaged the results.

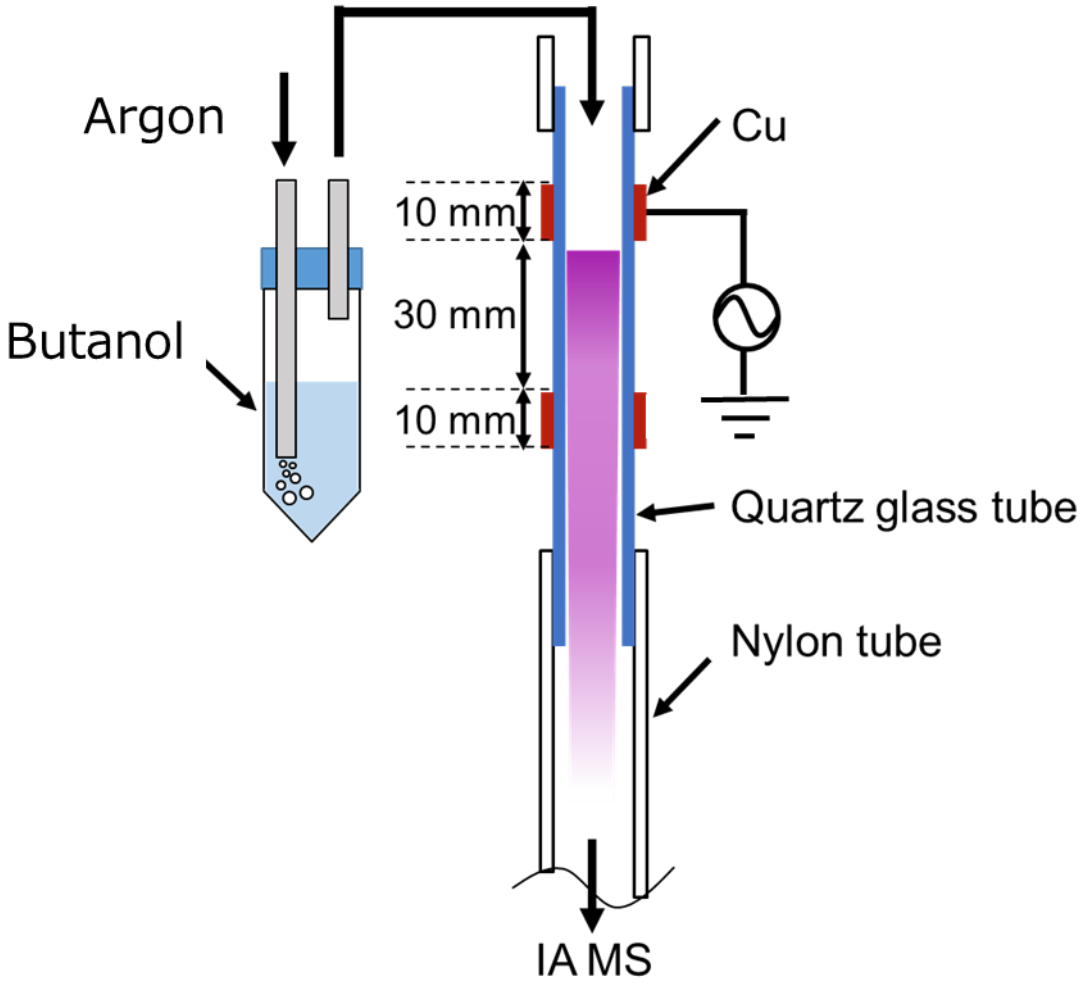

Figure 6.1: Schematic of the experimental setup.

Table 6.1: IAMS settings.

Setting parameters	Values
SEM	1800 V
Filament current	4.099 A
Emitter bias	29.20 V
Scan speed	300 ms/amu

6.3 Experimental results

6.3.1. Effects of sample gas pressure

IAMS spectrum intensity depends on partial pressure of the sample gas molecules, so the author investigated this dependency to establish appropriate parameter settings. The author changed the flow rate of sample butanol gas (mass: 74) under constant flow rates of N_2 and Ar. Flow rates for N_2 and Ar were 7.5 sccm and 1 slm, respectively.

Figure 6.2 shows spectrum intensity of butanol with Li+ (m/z = 81) as a function of total pressure with and without discharge (plasma). In both cases, the intensity increased with total pressure (i.e., butanol partial pressure), becoming saturated in a range above 110 Pa. The obtained relation between partial pressure of the sample gas and spectrum intensity confirmed that the effects of partial pressure were small above 110 Pa. This research therefore conducted experiments at near 115 Pa.

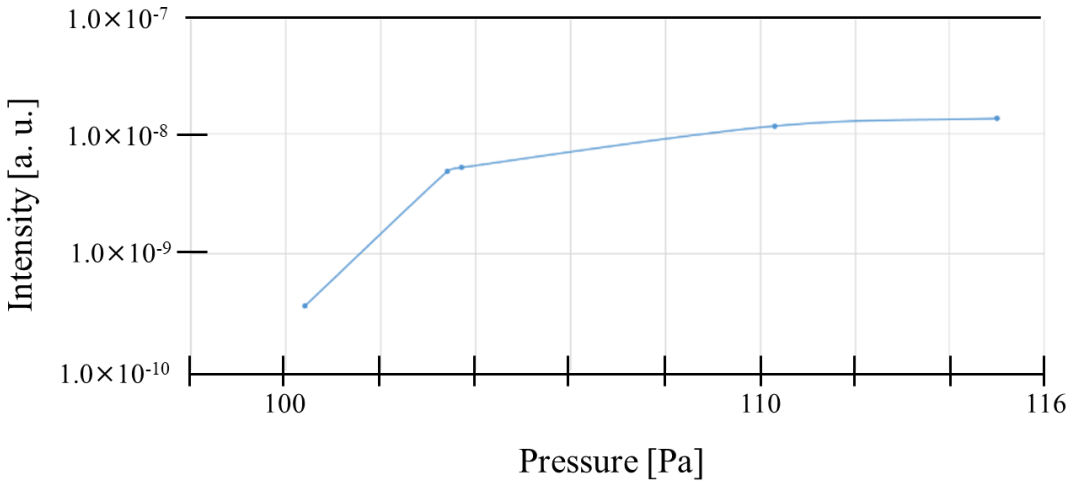

(a) Without discharge (plasma).

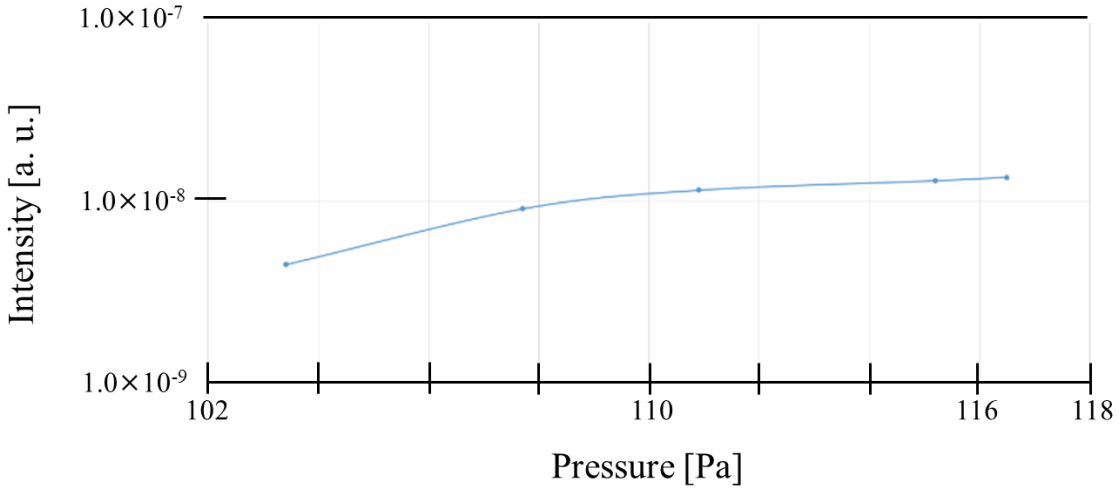

(b) With discharge (plasma).

Figure 6.2: Intensity of butanol spectra with and without discharge at different pressures.

6.3.2. Comparison between cases with and without plasma

The following discusses the properties of butanol decomposition by DBD plasma, comparing cases with and without discharge. There are only limited data regarding probabilities of Li^+ attaching to molecules, and further data were not obtained, so discussions in this section are qualitative. Figure 6.3 shows mass spectra for butanol

measured by IAMS with and without discharge. Blue lines (sample) indicate spectra without discharge (gas flow only), and orange lines (sample + plasma) indicate spectra with discharge. The figure is shown at linear and logarithmic scales for ease of discussion.

The peak at m/z = 81 (mass: 74) corresponds to butanol, and the surrounding peaks in Figure 6.3(b) are considered to be due to mainly attachment and detachment of H atoms because isotope ratio of hydrogen, oxygen and carbon is less than 1%. The peak at m/z = 99 to be a quasi-molecule of butanol with an H_2O molecule and Li^+ as $(C_4H_9OH)(H_2O)Li^+$.

Candidate molecules for the peak observed at m/z = 57 are butadiyne (diacetylene; C_4H_2) and titanium dioxide (TiH_2). It was not possible to identify which, but the peak was not observed under other sample gas conditions (ethanol). The author therefore guesses that the peak at m/z = 57 indicates C_4H_2 from decomposition of butanol, but the existence of titanium as an impurity cannot be ruled out.

Table 6.2 summarizes assignments of peaks and corresponding candidate species in the sample gas. The peak at m/z = 7 is Li+, but other m/z peaks less than 10 were observed in all considered cases. These were likely due to apparatus characteristics.

Spectra show no argon peak, indicating that Li^+ does not attach to nonpolar molecules. IAMS successfully produced signals due to quasi-molecular ions and radicals, whereas decomposition accompanied by ionization is inevitable for unstable radical species when traditional electron ionization techniques (such as EIMS) are used.

Figure 6.4 shows differences in spectra between cases with and without discharge. There were changes in several peaks under discharge (plasma). This research analyzed these changes, assuming that decreases indicate decomposition by plasma and that increases are by-products of decomposition.

The author first describes the decreased peaks, observed at *m*/*z* = 19, 25, 41, 57, 58, 79, 81, 82, 97, 99, and 100. The largest decreases were at *m*/*z* = 81 and 99, with surroundings indicating decomposition of butanol. The author calculated the decomposition rate of butanol as about 4.6% ($\frac{1.357-1.295}{1.357} = 0.04569$) and that at *m*/*z* = 99 (mass: 92) as about 15% ($\frac{5.873-5.006}{5.873} = 0.1476$). The latter may include detachment of H_2O from butanol, which apparently causes a butanol peak.

This section next describes increased peaks, which were observed at *m*/*z* = 35, 63, 65, and 67. The increases seen at 63 and 67 centered around 65. Molecules at *m*/*z* = 63 and 67 are assumed to be molecules where hydrogen differed by two atoms. There are multiple candidate molecules at *m*/*z* = 65 (mass: 58), namely, acetone (CH_3COCH_3) and allyl alcohol (CH_2CHCH_2OH).

The difference between the masses of butanol 74 and 58 is 16. It is possible that one C and four H were removed from the original butanol, or that one O atom was removed. Further discussion is presented in the next section.

Candidate molecules at *m*/*z* = 35 (mass: 28) are CO and N_2. There is a possibility that N_2 in atmospheric air was included as an impurity. Another possibility is that one or two places were cleaved and that one C, one O, and some H detached, thereby forming CO.

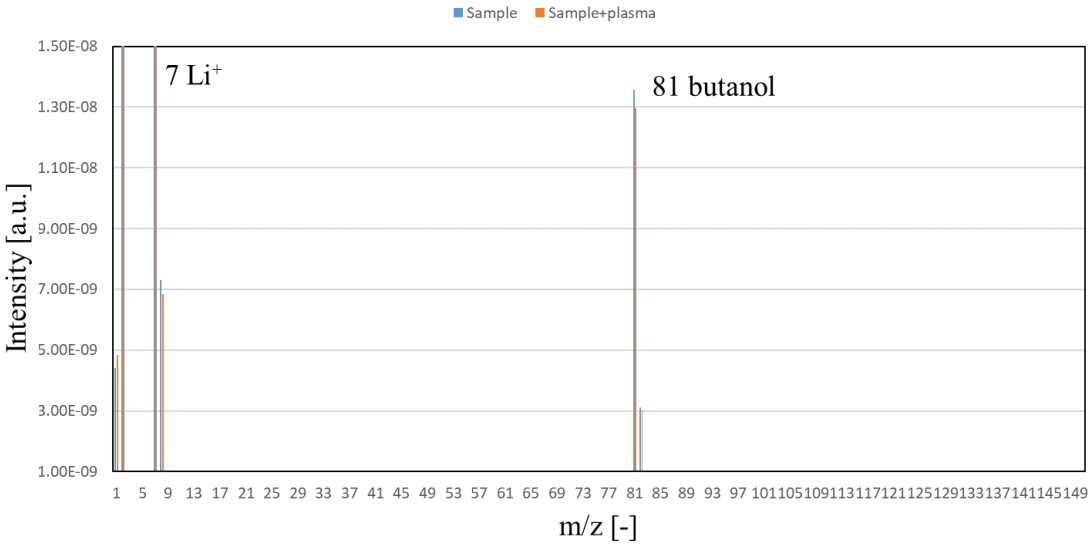

(a) Linear scale.

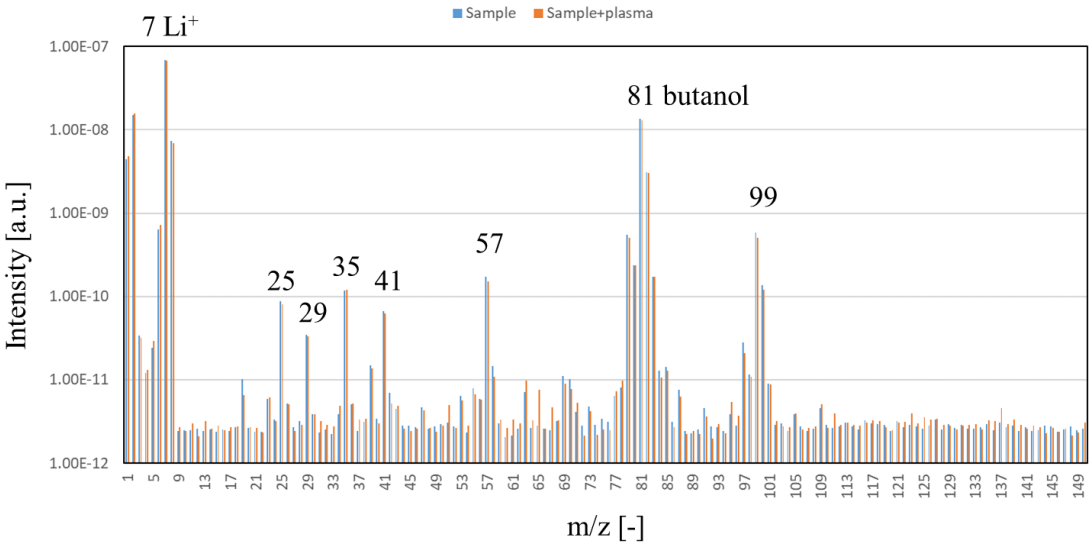

(b) Logarithmic scale.

Figure 6.3: Mass spectra for butanol measured by IAMS with and without discharge.

Table 6.2: Assignment of peaks observed in IAMS spectra.

m/z	mass	assignment	candidate corresponding species
99	92	$(C_4H_9OH)(H_2O)$	
81	74	C_4H_9OH	
57	50	C_4H_2	TiH_2
41	34	H_2O_2	
35	28	CO	N_2
29	22	-	
25	18	H_2O, C_2H_6	
7	7	Li+	

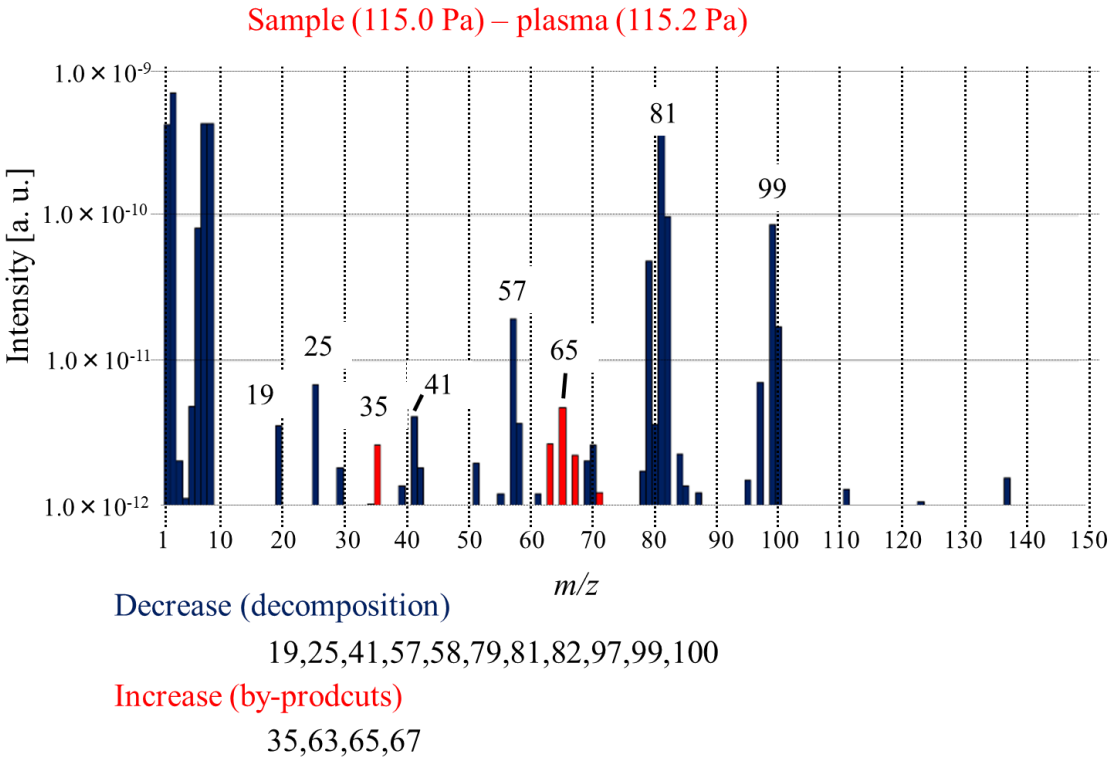

Figure 6.4: Differences in IAMS spectra between discharge and no-discharge cases.

6.4 Discussion

The following discusses the decomposition mechanism of butanol by atmospheric pressure DBD argon plasma. Comparison of spectra in cases with and without discharge indicated that the decomposition rate of butanol was about 4.6%, assuming constant attachment probability of Li^+. Butanol with an H_2O molecule is considered to correspond to the peak at m/z = 99 (mass: 92), and decomposition of this molecule was estimated as about 15%. Regarding these decomposition rates, detachment of H_2O molecule may increase the butanol peaks, making the decomposition rate of butanol likely to be underestimated. The total decomposition amount of butanol would thus be the sum of decomposition, but quantification remains difficult.

Increased peaks at m/z = 35 and 65±2 likely correspond to by-products generated though the decomposition process. Candidate molecules at m/z = 35 (mass: 28) are C_2H_4, CO, and N_2. While the possibility that N_2 was present as an impurity from air cannot be excluded, we assume that these peaks were not due to impurity because the measurements were performed five times and averaged. This research therefore discusses the reaction pathways of C_2H_4 and CO. For m/z = 65 (mass: 58), the difference between the butanol mass (74) and the observed mass (58) is 16. This mass corresponds to CH_4 and O, and the peak at m/z = 65 is thus considered to be either C_3H_7O or C_4H_{10}.

From the above discussion, the following four reactions can be considered for decomposition of butanol by argon plasma, assuming primary reactions (mainly by electron impact). Here, underlines show the assigned molecules corresponding to peaks observed in IAMS spectra.

$$C_4H_9OH \rightarrow \underline{CH_2{=}CH_2} + CH_3CH_2OH \quad (m/z = 35, \text{mass} = 28)$$

$$C_4H_9OH \rightarrow \underline{CO} + CH_3CH_2CH_3 + H_2 \quad (m/z = 35, \text{mass} = 28)$$

$C_4H_9OH \rightarrow \underline{CH_3CH_2CH_2=O} + CH_4$ (m/z = 65, mass = 58)

$C_4H_9OH \rightarrow \underline{CH_3CH_2CH_2CH_3} + O$ (m/z = 65, mass = 58)

Previous studies have investigated butanol decomposition properties through plasma, catalyst, and shock-tube experiments [1-3]. Claudette et al. measured decomposition rates and pathways of *n*-butanol by shock-tube experiments [1], where reaction temperatures and pressures were 1126-1231 K and 1.3-6.5 bar. They reported that ethylene $CH_2=CH_2$ and 1-butene $CH_2CHCH_2CH_3$ were the only products. They also showed that the mechanism of the initial decomposition steps involved direct elimination of water and C-C bond cleavage. The reactions that they reported are as follows:

$C_4H_9OH \rightarrow CH_3 + CH_2CH_2CH_2OH$

$C_4H_9OH \rightarrow CH_3CH_2 + CH_2CH_2OH$

$C_4H_9OH \rightarrow CH_3CH_2CH_2 + CH_2OH$

$C_4H_9OH \rightarrow CH_3CH_2CH=CH_2 + H_2O$

Comparing these reactions with those in this study, the attributions of H atoms are different. Pressure, temperature, and presence of electron impact reactions in plasma may affect this difference. To identify molecular structures and reaction pathways, further measurements under other conditions and with other measurement methods are required.

In this research, the decomposition of butanol is considered to be realized mainly by electron impact reactions between butanol and electrons in DBD plasma. This research also performed numerical analysis to additionally discuss the decomposition process.

Figure 6.5 shows cross-sections of electron impact with methanol, ethanol, and propanol from Ref. [4], which provided no data for butanol. Decomposition of alcohols are discussed based on these cross-sections.

Regarding methanol, CH_nO^+ (n = 0−4) are main products, and H atoms tend to detach from methanol. With increasing numbers of C atoms, C-C bonds tend to break not only at the edge. From these tendencies, the decomposition process of butanol likely has more products.

Figure 6.6 shows rate coefficients of electron impact reactions for mixtures of argon with methanol, ethanol, or propanol. These rate coefficients were calculated using the Boltzmann solver Bolsig+ [5] with the cross sections under conditions of Ar/alcohol=0.99/0.01, 300 K, and 1 atm. The calculation assumes that the electron energy function is determined by argon related reactions because of its dominant ratio in the mixture. From the rate coefficients, direct ionization by electron impact reactions is likely to occur in helium DBD plasma with an electron temperature of approximately 4-10 eV. For all alcohols in this discussion, CH_nO^+ is likely to be generated by their decomposition, but the candidate assignment peak is only m/z = 29 (n = 1). This indicates that CH_nO^+ immediately reacts with other molecules and that secondary reactions are important for understanding the decomposition mechanism in more detail.

For discussion of more complicated molecules like butanol, odor gas, and volatile organic compounds, more detailed measurements and related basic data are needed.

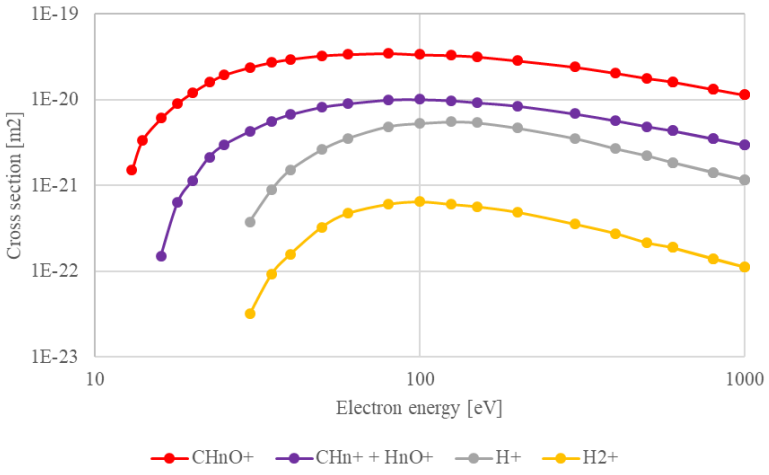

(a) Methanol.

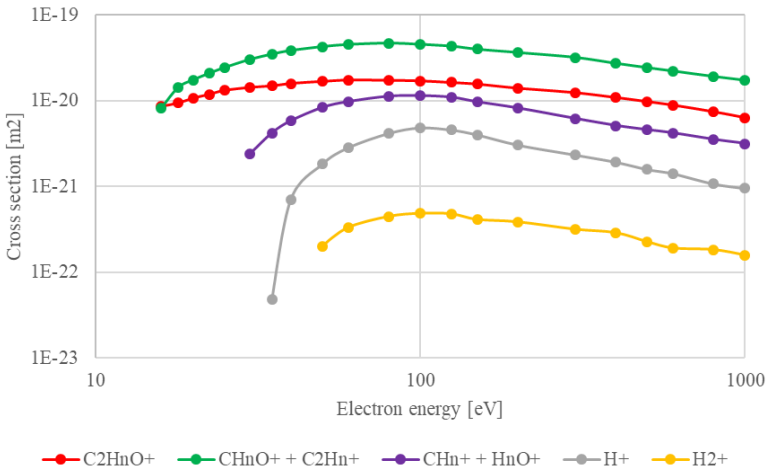

(b) Ethanol.

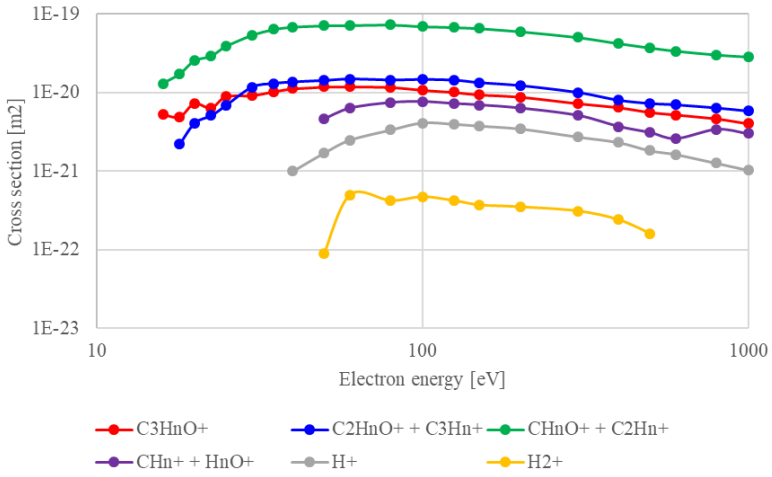

(c) Propanol.

Figure 6.5: Electron impact cross-sections for methanol, ethanol, and propanol.

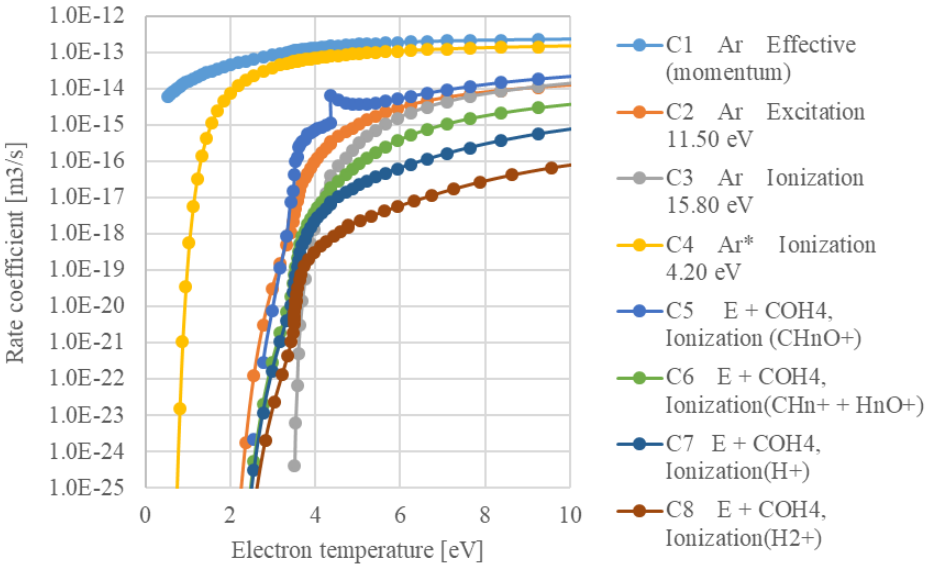

(a) Ar/methanol=0.99/0.01.

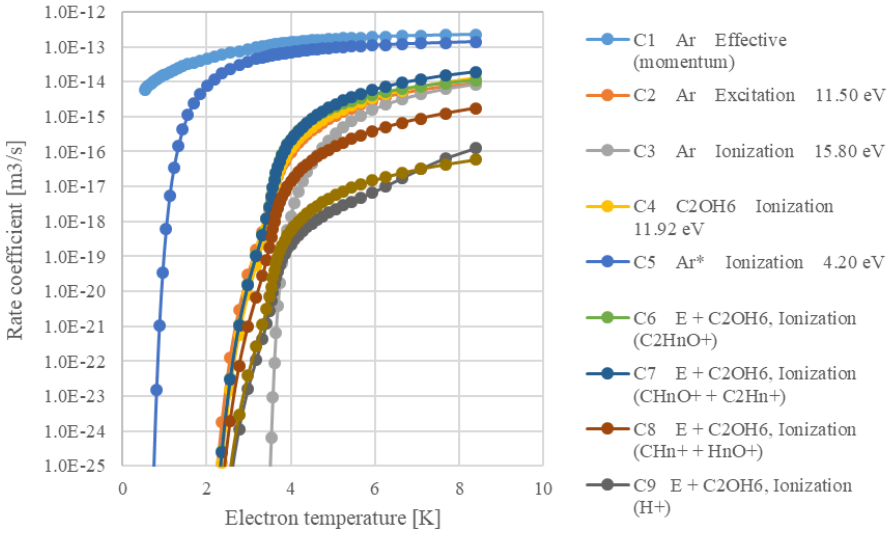

(b) Ar/ethanol=0.99/0.01.

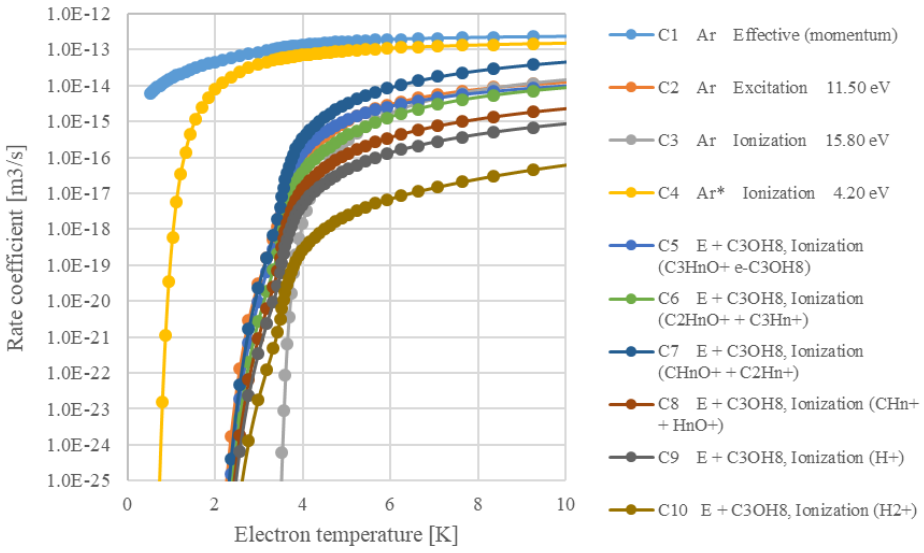

(c) Ar/propanol=0.99/0.01.

Figure 6.6: Rate coefficients calculated with electron impact cross-sections for methanol, ethanol, and propanol.

6.5 Conclusion

This chapter utilized IAMS to analyze decomposition of butanol by atmospheric pressure DBD argon plasma. Comparison of spectra between cases with and without discharge indicated that the decomposition rates of butanol and butanol with a H_2O molecule were about 4.6% and 15%, assuming constant attachment probability of Li^+. The decomposition rate of butanol may be underestimated, because detachment of the H_2O molecule may increase the butanol peak. This research proposed four decomposition processes as the decomposition mechanism of butanol by DBD LTAPP. IAMS can detect by-products and facilitates discussion of relevant mechanisms. Rate coefficients were calculated under Ar/alcohol=0.99/0.01 conditions with the Boltzmann solver. Results indicates that secondary reactions CH_nO^+ (n=0-4) are important for understanding the decomposition mechanism. For more detailed discussions, analyses combined with other measurement methods and related basic data are needed to identify molecular structures.

References

1. C. M. R. Reyes and W. Tsang, J. Phys. Chem. **116** 40 9825–9831 (2012).
2. A. M. El-Nahas, A. H. Mangood, H. Takeuchi, and T. Taketsugu, J. Phys. Chem. A **115** 13 2837–2846 (2011).
3. M. H. Yuan, C. C. Chang, Y. Y. Lin, C. Y. Chang, W. C. Liao, J. L. Shie and Y. H. Chen, J. Advanced Oxidation Technol. **19** 1 (2019).
4. R. Rejoub, C. D. Morton, B. G. Lindsay, and R. F. Stebbings, J. Chem. Phys. **118** 4 (2003).
5. G. Hagelaar and L. Pitchford 2005 Solving the Boltzmann equation to obtain electron transport coefficients and rate coefficients for fluid models Plasma Sources Sci.

Technol. **14** 4 722 (2005).

Chapter 7 Conclusions and future works

7.1 Conclusions

This research provided experimental and numerical analysis results to understand both basic LTAP phenomena such as the streamer discharge and the dielectric barrier discharge, and the gas decomposition process as an application using LTAP.

Firstly, about the streamer discharge, propagations of primary and secondary streamers in air were visualized under a pin-to-plane geometry with streak imaging. The propagation speed of the primary streamer was estimated as 0.2×10^6 m/s (0.2 mm/ns). Besides, a relation between the current peak and, the gap distance between the electrodes and the repetitive frequency was obtained. This result indicates the existence of proper gap for frequency.

For more detailed analysis of spatiotemporal behaviors of streamer discharges that occur on the order of nanoseconds, numerical simulations were conducted. By a self-consistent, multi-species, multi-temperature plasma fluid modeling, streamer propagations in the atmospheric pressure argon streamer discharge were investigated. A parametric study was conducted for positive and negative polarity of the applied voltage under a pin-to-plane geometry with a gap of 2 mm. The obtained knowledge was as follows. First, a positive primary streamer propagates in the plasma with the high electron density, then the secondary streamer further increases the plasma density, generating abundant metastable species. A relation between streamer head diameter and its propagation speed was obtained, for instance, 1.4 mm and 1.5 mm/ns at 10 kV. Second, a negative streamer diffusely propagates in the inter-electrode gap under high-voltage conditions. A corona-type discharge was observed at the low negative voltage. Since the generated species maintained both positive and negative polarities, a stable high density

of 10^{20} to 10^{22} m^{-3} under a positive low-voltage application has advantages for developing argon-based atmospheric pressure plasma applications. It is confirmed that experimental and numerical analysis can complement each other and lead to more deep discussions than either alone, although there is room for improvements in both methods in this research. Moreover, the effectiveness of modeling with simple chemistry argon model was also confirmed for the analysis of streamer discharge phenomena.

Secondary, regarding dielectric barrier discharge, we investigated DBD plasma in a coaxial DBD device through experimental and numerical analyses. Experimental analysis confirmed filament-like argon DBD inside the device. This discharge mode seemed to have three-dimensional structures.

This research analyzed the formation process of helium plasma in the coaxial DBD using a self-consistent, multi-species, multi-temperature plasma fluid model. The results indicate that plasma forms in a reactor-type DBD through three discharge modes. First, a glow-like discharge is generated between the electrodes, and when the space charge due to the difference in positively and negatively charged species densities reaches the same level as that of the bulk plasma ($1\times10^{18}/m^3$), an electric field wavefront is formed and a streamer-like (bullet-like) discharge develops in the axial direction. Finally, when the electric wavefront reaches the dielectric surface, it transitions to a surface discharge strengthened by the accumulated charge, and the discharge propagates to the full electrodes. At this time, the surface charge density is about 9×10^{-4} C/m^2. Compared with $1\times10^{19}/m^3$ between the electrodes, the electron number density near the electrodes is as high as $1\times10^{20}/m^3$, confirming that the strong emission in this region is due to the surface discharge. This plasma formation process is quite different from that in a planar DBD, in which one discharge mode basically corresponds to one discharge pulse. In the reactor-

type DBD, we confirmed the development of bullets, as in the case of the plasma jet, but these are trapped by the strong electric field (momentarily about 350 Td) due to the electric field induced by a combination of the ground electrode and the accumulated charge. The propagation distance is short (6 mm), and it immediately transitions to a surface discharge. This suggests the possibility of controlling plasma bullets not only by the distance between the electrode and the tube outlet, but also by the electrode structure (arrangement). A parametric study indicated that the inner diameter has the largest effects on plasma region enlargement. Radial uniformity of the electron number density depends on distribution of the first-stage glow discharge. In the cases of low applied voltage, thicker dielectric, lower dielectric constant, larger inner diameter, and larger gap, a weaker electric field in the region between the electrodes narrows the glow plasma, and the subsequent streamer propagation forms radial nonuniformities. Because there are fewer effects on basic plasma distributions, dielectric properties can be chosen considering safety, durability, and controllability.

Finally, this research utilized IAMS to analyze decomposition of butanol by atmospheric pressure DBD argon plasma. Comparison of spectra between cases with and without discharge indicated that the decomposition rates of butanol and butanol with a H_2O molecule were about 4.6% and 15%, assuming constant attachment probability of Li^+. The decomposition rate of butanol may be underestimated, because detachment of the H_2O molecule may increase the butanol peak. This research proposed four decomposition processes as the decomposition mechanism of butanol by DBD LTAPP. IAMS can detect by-products and facilitates discussion of relevant mechanisms. For more detailed discussions, analyses combined with other measurement methods and related basic data are needed to identify molecular structures.

7.2 Future works

Streamer discharge

In measurements of streamer discharges, data of argon streamers were not enough to discuss the physics in detail. In order to obtain voltage and current waveforms and streak images for argon streamers, it is necessary to improve the experimental system. Power supply with larger current capacity is needed at least. There are also room for improvement in how to adjust the timing of measurements and to stabilize streamer discharges. Understanding about streamers in other noble gases such as helium and neon is important and measurements should be conducted for these gases. Understanding about effects of negative ions and about air streamers is also important.

About numerical simulations, validation of the results under the same conditions as the experiment is important. Measurements about argon streamer discharge properties are required to conduct validation and identification of problems of the model. Developments of reaction models for other gases should be conducted for noble gases and air.

Dielectric barrier discharge

In order to understand DBD plasma in more detail, measurements should be conducted for voltage and current waveforms and the electron number density. Experiments with helium are demanded to understand helium DBD and compare with numerical simulation results. Differences of discharge properties between argon and helium should also be investigated.

Numerical simulations should be conducted in argon conditions after taking measures against instabilities in the simulations. Numerical analysis should also be

conducted about effects of waveforms of the applied voltage such as the frequency and pulse.

Gas decomposition process

About decomposition of the butanol, more data should be taken to discuss the decomposition mechanism. For example, effects of the input power, the electron number density, and the flow rate should be investigated. It is also important to compare the decomposition of alcohols with different carbon numbers.

In order to understand effects of each chemical species in plasma such as E, O, N and OH radicals, effects of the seed gas should be investigated for Ar(He)/H_2O, Ar(He)/O_2 and Ar(He)/N_2 conditions.

Experiments for odor gases such as indole (C8H7N) and isovaleric acid (C5H10O2) and volatile organic compounds should also be conducted.

Basic data such as electron impact cross sections are not enough to develop reaction models. More data survey and some assumptions such as using data on similar substances are necessary.

Appendix Mobility of electron in argon used in this research

Table A.1. Mobility data of electron in argon.

T_e [eV]	μN [/Vms]
0.02846756	1.29E+26
0.02975487	1.33E+26
0.03173586	1.38E+26
0.03477738	1.45E+26
0.03937968	1.52E+26
0.04614973	1.60E+26
0.05561446	1.68E+26
0.0681674	1.74E+26
0.0835084	1.75E+26
0.1008504	1.72E+26
0.1187927	1.64E+26
0.1363348	1.52E+26
0.1528764	1.39E+26
0.1682841	1.25E+26
0.1826913	1.11E+26
0.1965649	9.81E+25
0.2103718	8.66E+25
0.2244455	7.64E+25
0.2390528	6.74E+25
0.2544605	5.95E+25
0.2710021	5.25E+25
0.2886776	4.64E+25
0.3078205	4.10E+25
0.3286309	3.62E+25
0.3513089	3.21E+25
0.3760546	2.84E+25

0.4032682	2.52E+25
0.4331498	2.23E+25
0.4659662	1.98E+25
0.5021843	1.76E+25
0.5424044	1.57E+25
0.5868266	1.39E+25
0.6359845	1.24E+25
0.690345	1.10E+25
0.749041	9.80E+24
0.813073	8.70E+24
0.882441	7.71E+24
0.957145	6.83E+24
1.037185	6.04E+24
1.123895	5.34E+24
1.217942	4.73E+24
1.319326	4.19E+24
1.430048	3.71E+24
1.550108	3.28E+24
1.681507	2.91E+24
1.823578	2.57E+24
1.977655	2.28E+24
2.143071	2.02E+24
2.319826	1.78E+24
2.508587	1.57E+24
2.709354	1.38E+24
2.916124	1.23E+24
3.112889	1.12E+24
3.272969	1.06E+24
3.383691	1.04E+24
3.456394	1.04E+24
3.505085	1.05E+24
3.544438	1.06E+24
3.579789	1.06E+24
3.616474	1.06E+24
3.656494	1.05E+24

3.701183	1.03E+24
3.751875	1.01E+24
3.807903	9.93E+23
3.871268	9.70E+23
3.941303	9.46E+23
4.018675	9.22E+23
4.102717	8.99E+23
4.193429	8.77E+23
4.290811	8.57E+23
4.39553	8.38E+23
4.507586	8.21E+23
4.627646	8.05E+23
4.757711	7.90E+23
4.899115	7.76E+23
5.054526	7.62E+23
5.227946	7.48E+23
5.423377	7.34E+23
5.646822	7.20E+23
5.905618	7.06E+23
6.20977	6.91E+23
6.571284	6.76E+23
7.01017	6.61E+23
7.54377	6.46E+23
8.19743	6.30E+23
9.01117	6.16E+23
10.02501	6.00E+23
11.30565	5.84E+23
12.89978	5.68E+23
14.91412	5.51E+23
17.41537	5.33E+23
20.57028	5.15E+23
24.51225	4.97E+23
29.45472	4.78E+23
35.6845	4.60E+23
43.58845	4.42E+23

53.86692	4.27E+23
67.367	4.13E+23
85.4427	4.03E+23
100	4.03E+23

Acknowledgements

First of all, I would like to thank Prof. Masaru Hori of the Center for Low-temperature Plasma Sciences, Nagoya University, for giving me the opportunity to undertake this research and to pursue a Ph. D. at the Hori-Ishikawa Laboratory. Without his strong recommendations, I would not have been able to challenge myself. As my supervisor, he gave me a great deal of advice in formulating study policies and technical discussions. I also thank Prof. Masaru Hori for his strong leadership.

I would also like to express my gratitude to co-supervisor Prof. Kenji Ishikawa of the Center for Low-temperature Plasma Sciences, Nagoya University, for giving me great advice in carrying out this research. I wish to thank him for all of our discussions about experimental and simulation results, planning, how to write and organize papers, and how to submit. I am so deeply grateful to Prof. Kenji Ishikawa that I cannot express it.

I would like to show my greatest appreciation to Prof. Hirotaka Toyoda and Prof. Makoto Sekine of the Center for Low-temperature Plasma Sciences, Nagoya University, Prof. Noriyasu Ohno of the Department of Electrical Engineering, Nagoya University, and Prof. Fumiyoshi Tochikubo of the Electrical and Electronic Engineering, Tokyo Metropolitan University, for giving me valuable advices to complete this thesis.

I would like to thank Assistant Prof. Takayoshi Tsutsumi of the Center for Low-temperature Plasma Sciences, Nagoya University, for experimental assist and valuable discussions.

I would like to express my gratitude to Tatsuyuki Moriyama and Kaito Murakami of Hori-Ishikawa Laboratory, for supporting experiments and discussions.

I also would like to thank Hori-Ishikawa Laboratory members and secretary for their many supports.

I would like to thank Dr. Hisataka Hayashi of KIOXIA corporation (Toshiba memory corporation at that time), for giving me a chance to start this research and valuable advice.

I would like to thank Prof. Laxminarayan L. Raja of The University of Texas at Austin, for giving me valuable advice for basic knowledge about plasma numerical simulation.

I am deeply grateful to Kenji Hirohata and Tomonao Takamatsu of Mechanical and Systems Laboratory, Advanced Intelligent Systems, Corporate Research and Development Center, Toshiba Corporation, for advice to start this research.

I would like to thank to Akio Ui, Masato Akita, Shotaro Oka, Okano, Takeshi Morino, Kei Matsuoka, Hideaki Okano of Mechanical and Systems Laboratory, Advanced Intelligent Systems, Corporate Research and Development Center, Toshiba Corporation, for their many supports. I would particularly like to thank Akio Ui and Masato Akita for their valuable advice and discussions.

Finally, I would like to thank to my parents, my brother, and my wife for their always supports.

List of papers

	Title	Journal	Authors
	Original papers		
1	Numerical simulations of stable, high-electron density atmospheric pressure argon plasma under pin-to-plane electrode geometry: Effects of applying voltage polarity	Journal of Physics D: Applied Physics, Vol. 53, No. 26, 265204, 14 pages (2020)	Y. Sato, K. Ishikawa, T. Tsutsumi, A. Ui, M. Akita, S. Oka, and M. Hori
2	Numerical analysis of coaxial dielectric barrier helium discharges: Three-stage mode transitions and internal bullet propagation	Applied Physics Express, Vol. 13, No. 8, 086001, 5 pages (2020)	Y. Sato, K. Ishikawa, T. Tsutsumi, and M. Hori
	International conferences		
1	Numerical analysis on size dependency of particulate matter charging property in plasma electric collector	ISPlasma2018/IC-PLANTS2018, March 4-8, Nagoya (Japan), (2018)	Y. Sato, A. Ui